The Multiscale Microphysics of Galactic Outflows

by

Ryan Jeffrey Farber

A dissertation submitted in partial fulfillment
of the requirements for the degree of
Doctor of Philosophy
(Astronomy and Astrophysics)
in The University of Michigan
2021

Doctoral Committee:

Associate Professor Mateusz Ruszkowski, Chair
Professor Joel Bregman
Professor Gus Evrard
Professor Oleg Gnedin
Professor Ellen Zweibel

Ryan Jeffrey Farber

rjfarber@umich.edu

ORCID iD: 0000-0002-0649-9055

ACKNOWLEDGEMENTS

This thesis would not be possible without the support of many people. Most principally, my development as a scientist these past six years would not have occurred without the steadfast support, enthusiasm, and encouragement of my advisor Mateusz Ruszkowski. I recall many moments in my first two years walking into your office feeling dejected I could not uncover the latest bug in my code by myself. However, you always made yourself available to me, offered invaluable insights, and your quick wit and infectious enthusiasm put a quicker clip to my step upon walking back out. Thank you for pushing me to apply for fellowships year after year. Initially, these ventures seemed of dubious merit, but I always gained some interesting perspective on an existing project, or fun new idea of research to pursue in the future. My appreciation of your strong advocacy for me during conferences, presentations, job applications, and the advancement to candidacy process cannot be understated. You have served as a wonderful role model as a researcher and mentor, which I strive to emulate with (hopefully!) my own students in the future.

Next, I am happy to acknowledge support from Paco Holguin. For one thing, our weekly zooms during lockdown helped tremendously with my social welfare. Shooting hoops with you at the CCRB and playing together as part of the 'Cosmic Rays' in intramural sports provided a nice break from work – especially grading! Moreover, I am profoundly grateful to your support as a collaborator. All the little moments bouncing ideas and debugging each other made the process much less demoralizing to realize I'm not the only one that deals with silly mistakes during code development

– and indeed much more enjoyable overall. I'm grateful we've been able to continue discussing our works and future plans over zoom. Hopefully you can manage a trip to visit MPA but in any case, all the best to your future success!

Although not one of my collaborators, I would be remiss to not include Zhijie Qu. I am profoundly grateful that we were in the same graduate student cohort in Michigan. Your patience despite the many questions I asked you when studying for class exams, and especially the prelim, and the tireless work you put into your own research has been a constant source of inspiration for me. I'm grateful for a number of enlightening discussions on our walks to the CCRB; I would not be aware of half the observational literature of the CGM if it was not for your wisdom.

Fourth, I'd like to acknowledge friends amongst the graduate students in the Astronomy department at Michigan. Adam Smercina: it's been great knowing you since our REU together at Wisconsin. If not for your zealous love of PAHs, I don't know I would have half the interest in dust as I do today. Jesse Golden-Marx: there are really too many great memories to choose, but all of the time together late at the office working, playing in intramural sports together, going to the DC movies and Detroit sports, and especially for discussions about My Hero Academia have left an indelible mark on me. I'm grateful we overlapped at Michigan. Since I'll probably be forced to shorten even this much I'd like to briefly shout-out support, even during stressful times, from Ben Setterholm and Juliette Becker. I'd also like to thank Dan Gifford, Matt Miller and the older graduate students for first welcoming me to Michigan. Last, I'd like to thank the younger graduate students for their efforts in making the department a more welcoming environment for everyone.

Fifth, I acknowledge support from Riley, Enrique, Jesse, and many more members of SWIP. Engaging in outreach was terrific fun and I hope that together we have inspired new generations of scientists and leaders.

Sixth, I am grateful to my collaborators. Ellen Zweibel, your profound under-

standing of cosmic ray physics (and memory of 70s references) has made a significant impact on this budding cosmic-ray researcher. Karen Yang, I am grateful for your support and numerical expertise. Stephanie Tonnesen, most recently, thanks so much for hosting me at the CCA! It was great finally meeting you. I'm grateful for your steadfast support during this ram pressure stripping + cosmic ray project, despite the innumerable computational pitfalls and turns, we've made it! Max Gronke: I am eternally grateful for your taking time in one of your last days in Santa Barbara to discuss my research. Your support and mentorship in the past ∼18 months has made a tremendous effect on my growth as a scientists and the trajectory of my career aspirations. Your support of work-life balance has not fully impacted on me yet, but I'm grateful for the support. I'm fervently looking forward to our work together at MPA!

Seventh, I'm pleased to acknowledge the stimulating transdisciplinary conversations and general fun times spent with multiple generations of roommates at Munger. Eric, BK, Matt, Vikram, David, Xun, Ryan, Joel, Peter, Corey, Nolan, Mahiro, Naoto, Nick, Tawfiq, Ryan, Jack, Trey, and honorary roommates Daniel & last but certainly not least Ke'ale: I have learned much from your various and altogether varying differences in approach and outlook in life. Such diversity of quirks, habits, and mannerisms has certainly enriched my life these past six years.

Eighth, I'd like to acknowledge friends and mentors at Wheaton College, without whom, I would not be where I am today: Jason, jc, Bloch, Dipankar, Tim, Geoff, Tony; Andrew, Kim, Ariel, JT, Brent, Yohannes, and many more.

Ninth, I'm acknowledging forever friends Andrew Torre, Andrew Noerr, Jameson Haller, Jared Ackley, Sean Rohtla, Charlie Yates, Thomas Matthews, and many more friends from high school and previously, I am grateful for your continued friendship and for many wonderful memories together.

Tenth, I would not be who I am today without the support of my wonderful family. I love having so many aunts, uncles, and cousins but unfortunately that also means I will not list everyone here. Instead I will shout-out honorary brother Daniel Steger. I hope you'll visit Germany next year! Last but certainly not least, I am eternally grateful, despite moments of certainly being an ungrateful ingrate, to my loving mother, father, and sisters. You all mean the world to me. Mom, your courage to explore new hobbies and stay active in spite of injury has been truly inspirational. Thank you for all the great memories of birthday parties growing up and caring for me when I was sick. This thesis would not be possible without you. Perhaps most principally, after my first failing grade in high school math, your attention to the development of my study skills made a huge impact on my test-taking for the rest of high school and college. Dad, your dedication to work has probably subconsciously impacted the development of my own work ethic. I appreciate your consistent encouragement for me to do my best, whether in sports growing up or academically. Christina, we may not always get along the best but you've supported me whenever I called and really wanted to talk to you. I appreciate all the great times we had together growing up, watching Digimon, Pokemon, Yugioh, and playing games together. It was really great of you to review my book, and I know I can count on you through thick and thin whatever the future holds for each of us on our journeys. Meaghan, I still believe you have been graced with one of the greatest laughs. I love seeing you whenever I come home and am glad you've been staying safe and healthy.

To all who've been named above, directly or parenthetically, I look forward greatly to seeing you all again soon!

TABLE OF CONTENTS

CHAPTER

LIST OF FIGURES

Figure

LIST OF TABLES

Table

ABSTRACT

Observations indicate spiral galaxies ubiquitously launch multiphase outflows, which help to explain observations of self-regulating star formation in the disk and metallicities of the circumgalactic, intergalactic, and intracluster media much higher than primordial abundances. These outflows are composed of hot $10^{6-7}\,\mathrm{K}$ X-ray emitting gas, cool atomic $\sim 10^4\,\mathrm{K}$ gas, cold molecular gas, and cosmic rays. The observed rapidly outflowing cool and cold gas phases are theoretically puzzling, as such gas should be incorporated into the hot phase before it can be entrained. The presence of cold gas in the ram pressure stripped tails of galaxies in cluster outskirts is similarly surprising, as the intracluster medium is even hotter $\sim 10^8\,\mathrm{K}$. In this dissertation, I study the physics responsible for launching galactic outflows at multiple scales. Performing simulations on the scale of interstellar medium patches, I find that cosmic-ray transport plays a crucial role in their ability to launch outflows. Temperature-dependent transport of cosmic rays helps launch fast outflows and generate large-scale radio halos. Studying the microscopic scale of individual cold clouds in a thermally driven, transonic outflow, I find molecular material can survive the entrainment process for clouds larger than a critical radius. At the macroscopic scale of global spiral disks in cluster environments, I find cosmic rays modify the response of the interstellar medium to the ram pressure of the intracluster medium wind. Specifically, I find that cosmic rays protect cold, tenuous gas that is otherwise stripped in purely thermal models. Moreover, the influence of cosmic rays on the star formation rate and the accretion of material towards the galactic center, powering the activity of galactic nuclei, may provide new constraints on cosmic-ray transport and calorimetry. These results imply that thermal and cosmic-ray feedback play a crucial role in understanding multiphase galactic outflows.

CHAPTER I

Introduction

1.1 A Brief History of Galactic Outflows

In 1610 Galileo revolutionized our understanding of the cosmos. Although his telescope was barely 50% larger than the human eye, such a technological leap enabled the discovery of Jupiter's moons, the phases of Venus, hundreds of previously unseen stars, and the cratered surface of the moon (*Galileo*, 2016), radically restructuring humanity's knowledge of the cosmos. Three hundred years later, Edwin Hubble utilized a telescope ∼66 times larger at Mount Wilson observatory. The 100-inch Hooker telescope not only enabled discovery that space is expanding (*Hubble*, 1929a), it revolutionized our understanding of the universe by unveiling the existence of external galaxies (*Hubble*, 1929b). Thus we see repeatedly the greatest discoveries in astronomy are born from giant technological leaps.

Perhaps unsurprisingly then, shortly after the deployment of the 120-inch telescope at Lick observatory, *Lynds and Sandage* (1963) discovered massive filaments of Hα outflowing several times the escape velocity from the nearby (3.9 Mpc distant; *Sakai and Madore* 1999) dwarf irregular galaxy, M82. See Figure 1.1 for the view from the *Hubble Space Telescope*. Subsequent multiwaveband measurements of M82 have revealed rich multiphase structures roughly coincident with the warm Hα filaments: hot X-ray emitting cavities (*Watson et al.*, 1984), cool 21-cm emitting shells (*Cottrell*,

Figure 1.1: Optical image of M82. The white/blue colors of the edge-on stellar disk can be seen from a small telescope. The red colors indicate the outflowing Hα emitting gas as observed by *Hubble Space Telescope*. Image Credit: NASA, ESA, the Hubble Heritage Team (STScI/AURA). Acknowledgement M. Mountain (STScI), P. Puxley (NSF) and J. Gallagher (U. Wisconsin).

1977), and even cold molecular clouds (*Weiß et al.* 1999; cf. Figure 1.2).

1.2 Observations of Galactic Outflows

In the past sixty years, observations have revealed the ubiquity of galactic outflows at low and high redshift (*Veilleux et al.*, 2005, 2020, and references therein) and generically find the most vigorous outflows are observed in intensely starforming systems. For example, a stream of neutral hydrogen connecting M82 to M81 suggests a recent interaction may have triggered a burst of star formation in the nuclear region of M82 (*Yun et al.*, 1994). The central explosion from subsequent supernovae is energetically consistent with the luminosity of the outflow (*de Grijs et al.*, 2000). Similarly, NGC 253 is one of the brightest and dustiest nearby (∼3.5 Mpc) galaxies,

Figure 1.2: False-color composite of M82. Similar to the optical image in Figure 1.1, orange colors mark Hα emitting gas observed by *Hubble*. Blue colors indicate the hot few million degree X-ray emitting gas observed by *Chandra*. Red colors mark the infrared observations by *Spitzer*, indicating blobs of cold gas and dust are outflowing from the galaxy. Image Credit: X-ray: NASA/CXC/JHU/D.Strickland; Optical: NASA/ESA/STScI/AURA/The Hubble Heritage Team; IR: NASA/JPL-Caltech/Univ. of AZ/C. Engelbracht.

lying at the center of its group (*Rekola et al.*, 2005). A recent merger with a gas-rich dwarf may have triggered the young, massive star clusters observed in its nuclear region (*Anantharamaiah and Goss*, 1996). The massive stellar winds and supernovae from the observed massive star clusters plausibly drive the outflow.

Only more locally can more quiescient galactic outflows be studied in depth. At 50 kpc distant, the Large Magellanic Cloud (LMC) is one of the closest galaxies to the Milky Way (*Pietrzyński et al.*, 2013). Absorption line measurements of an LMC star and a background quasar along nearly the same line of sight above a quiescient region of the LMC suggest a $\sim$100 km s^{-1} outflow driven from the LMC disk (*Barger et al.*, 2016) possibly exceeding the rate of star formation $\sim 0.2\,M_\odot\,\mathrm{yr}^{-1}$ by a factor of two.

Recently, cold outflowing gas has been observed in emission above the Milky Way's galactic center. *McClure-Griffiths et al.* (2013) detected $\sim$10 pc neutral hydrogen clouds outflowing at $\sim$200 km/s. Higher latitude observations detected clouds all the way to the limit of sensitivity, up to 3.5 kpc from the midplane of the Galaxy, with indications of a wind profile accelerating up to $\sim$330 km/s (*Di Teodoro et al.*, 2018; *Lockman et al.*, 2020). A growing sample of neutral clouds are observed to possess a molecular component (*Di Teodoro et al.*, 2020; *Su et al.*, 2021). Molecular outflows are similarly observed in the Small Magellanic Cloud (SMC; *McClure-Griffiths et al.*, 2018; *Di Teodoro et al.*, 2019), locally (e.g., NGC 253; *Bolatto et al.* 2013), and at high redshift (*Spilker et al.*, 2020).

As stars form from molecular gas (*McKee and Ostriker*, 2007), observations of molecular outflows are particularly interesting; for instance, the cycling of star-forming fuel between the disk and halo will regulate the galactic star formation rate, possibly reconciling the observed short depletion times of molecular gas via star formation with nevertheless star formation occurring at the present epoch (*Bigiel et al.*, 2011). Additionally, star formation in the outflows (*Maiolino et al.*, 2017; *Gallagher* *et al.*, 2019) may develop the halo component of galaxies, potentially providing an evolutionary mechanism for completely isolated spiral galaxies to become elliptical. As the neutral and molecular components of galactic outflows are expected to carry a gas mass from the disk similar to the star formation rate (*Li and Bryan*, 2020), galactic outflows may possibly explain longstanding challenges to the modern astrophysical picture of galaxy formation and evolution.

1.3 Implications of Galactic Outflows for Problems in Galaxy Formation & Evolution

As galactic outflows carry the enriched debris of stellar evolution, they may play a key role in enriching the intergalactic and intracluster media (IGM and ICM respectively; *Mac Low and Ferrara*, 1999; *Steidel et al.*, 2010; *Booth et al.*, 2012), explaining the observed stellar-halo mass (*Moster et al.*, 2010) and mass-metallicity (*Larson*, 1974; *Tremonti et al.*, 2004) relations, resolving the missing baryons problem (*Bell et al.*, 2003), and illuminating mysterious ion abundances revealed by quasar absorption line studies (*Werk et al.*, 2013).

The standard cosmological model consists of a cosmological constant term for the dark energy content accelerating the expansion of the universe, cold (i.e., non-interacting) dark matter dominating the gravitating mass, with 'baryonic matter' consisting of only ∼2% the remaining energy density (*Spergel et al.*, 2003). As such, galaxy formation is expected to be dominated by the dynamics of dark matter, with the baryons relatively inertly along for the ride, forming stars in dark matter over-densities. Consequently, a tight stellar-halo mass relation is expected (*Moster et al.*, 2010). However, the Milky Way is observed to possess far fewer and less luminous satellites than expected from cosmological N-body simulations tracking only dark matter (*Klypin et al.*, 1999). This "missing satellites" problem is resolved as a result of supernovae expelling galactic gas, perturbing the gravitational potential and consequently (indirectly) redistributing the dark matter profile in combination with tidal stripping (*Brooks et al.*, 2013).

Yet even after reconciling the missing satellites, observations of luminous galaxies indicate a "missing-metals" problem. A large sample ($\sim$50,000) of star-forming galaxies from the SDSS survey indicate a tight ($\pm$0.1 dex) correlation between stellar mass and the gas-phase metal abundance occurring over three decades in stellar mass (*Tremonti et al.*, 2004; *Peeples et al.*, 2014). Stellar chemical evolution 'closed-box' models suggest that galaxies, particularly at low masses should exhibit drastically higher metal abundances. However, galactic outflows have been shown to eject material more effectively in the weaker gravitational potential wells of dwarf galaxies, in plausible agreement with observations (*Larson*, 1974; *Garrison-Kimmel et al.*, 2019).

Other processes can expel metals from galaxies, which become increasingly relevant in environments of high galactic number density, such as galaxy clusters. Spiral galaxies are observed to be redder, more anemic in neutral hydrogen, louder in radio emission, and more bulge-dominated than spiral galaxies in the field, which may all be explained as a result of the ICM interacting with the interstellar medium (ISM; *Boselli and Gavazzi* 2006). When the ram pressure $P_{\rm ram} = \rho v^2$ (ρ is the density of the ambient medium and v is the differential velocity between the object and its surroundings) exceeds the gravitational restoring force per unit area, P_g, the ICM is able to remove gas from the ISM – a process called 'ram pressure stripping' (RPS, *Roediger*, 2009).

Observations of relatively isolated spirals inhabiting galaxy cluster outskirts detect 'tails' of multiphase gas extending up to 100 kpc from the galaxy, which is indicative of on-going RPS (*Poggianti et al.*, 2017b). The dense, molecular phase is theoretically not expected to be stripped from the gas disk (*Tonnesen and Bryan*, 2012). However, if galactic outflows can loft molecular clouds above the midplane even at velocities small compared to the escape velocity, the reduced gravitational restoring force may enable ram pressure of the ICM to unbind the molecular material from the galaxy. Thus, galactic outflows may act synergistically with ram pressure stripping (*Bustard et al.*, 2020).

While galaxy clusters as a whole nevetheless retain their gas, owing to the immense gravitational potential, in agreement with the cosmological ratio of baryons to dark matter observed by *WMAP* ∼17%, observations of smaller halos detect a paucity of baryons. L_* galaxies such as the Milky Way possess only ∼4% mass in baryons to dark matter while dwarfs are missing a few dex(!) of baryons (*Dai et al.*, 2010). Despite plaguing galaxy formation since its inception, the missing baryons problem may be resolved due to a recently discovered (*Tumlinson et al.*, 2011; *Werk et al.*, 2013; *Bregman et al.*, 2018) preponderance of gas surrounding galaxies in the form of a coronal component – the "circumgalactic" medium (CGM; *Spitzer* 1956).

Yet the CGM possesses its own mysteries. Recent absorption-line measurements indicate a surprisingly ubiquitous $\sim 10^5$ K phase (*Tumlinson et al.*, 2011); the very short cooling time of this gas suggests it is constantly replenished, e.g., via galactic outflows (*Qu and Bregman*, 2018a,b, 2019). However, such a phase may exist in hydrostatic equilibrium if supported by nonthermal pressures (*Faerman et al.*, 2020). Additionally, the existence of warm $\sim 10^4$ K gas with high covering fraction (*Werk et al.*, 2013) and low densities is perplexing from the expectation of thermal pressure equilibrium. Cool gas is expected to concentrate in a small volume of the CGM in pressure balance with the hot X-ray emitting gas. Moreover, observations of intact cold gas at high velocities is theoretically puzzling.

The acceleration of a cold cloud embedded in a hot wind is known as the classical "cloud-crushing" problem (e.g., *McKee and Cowie* 1977). The cold cloud is rapidly 'crushed' by the hot wind as a result of hydrodynamical instabilities (e.g., Kelvin-Helholtz and Richtmyer-Meshkov instabilities) mixing the two phases on a timescale

$t_{\rm cc}$ (*Klein et al.*, 1994):

$$t_{\rm cc} \sim \chi^{1/2} \frac{R_{\rm cl}}{\Delta v} \tag{1.1}$$

where χ is the density contrast between the wind and cloud[1], $R_{\rm cl}$ is the initial cloud radius and Δv is the shear velocity between the cold and hot phases. Since the acceleration timescale due to the ram pressure of the hot wind 'dragging' the cold cloud $t_{\rm drag} = \chi R_{\rm cl}/\Delta v$ is slower than $t_{\rm cc}$ by a factor of $\chi^{1/2}$, the cloud should be disrupted far before it becomes entrained. Hence observations of rapidly outflowing cold gas embedded in X-ray winds is theoretically puzzling. Recent work has shown that efficient radiative cooling allows sufficiently large clouds to survive (*Gronke and Oh*, 2018; *Farber and Gronke*, 2021), yet what launches these hot winds to begin with is a puzzle.

1.4 Mechanisms Powering Galactic Outflows

For galactic masses above L_*, active galactic nuclei (AGN) provide an energetically plausible mechanism for powering galactic outflows, despite the strong gravitational potential of such massive galaxies (*Croton et al.*, 2006). At lower galactic masses, massive stellar winds and supernova explosions, collectively referred to as stellar 'feedback,' can plausibly power the outflows, especially in systems of low-luminosity AGN (*Dekel and Silk*, 1986).

In the standard model of stellar feedback driven outflows, supernova shock-heat the gas in their environs, overpressurizing it compared to gas beyond the shock; the resulting pressure gradient inflates the cavity, launching a hot outflow from the galactic disk into the halo. While this model reproduces well the observed X-ray mass-loading of galactic outflows (*Strickland and Heckman*, 2007), CGM observations of

---

[1] $\chi \sim 10^{2-3}$ for a cloud of neutral hydrogen in a soft X-ray emitting galactic outflow and up to 10^6 for a molecular cloud exposed to the ICM.

thermally underpressured cold gas with a large covering fraction (*Werk et al.*, 2013) suggest nonthermal effects (e.g., turbulence, magnetic fields, or cosmic rays) must be responsible for total pressure equilibrium. Thus, nonthermal effects may play a role in driving galactic outflows and the properties of the CGM.

Starbursts and ultraluminous infrared galaxies possess large quantities of dust and their high star formation rate suggests a strong radiation environment (e.g., Arp 220; *Soifer et al.* 1984; *Scoville et al.* 1991). The large cross-section of dust for interaction with photons may enable efficient coupling between the radiation field and the gas, powering outflows (*Murray et al.*, 2011). However, recent work suggests that when the ultraviolet (UV) flux dominates over the infrared (IR), clouds are rapidly crushed, destroying the dust (*Huang et al.*, 2020). Plausibly the UV radiation does not travel far from the sites of massive stars (where local densities are high), being reprocessed into IR by dust grains; although promising, further work is needed regarding the ability of radiation pressure to drive outflows.

Another nonthermal mechanism that may help to power galactic outflows and explain observational puzzles of the CGM was suggested by the earliest observations of galactic outflows. *Lynds and Sandage* (1963) noted coincidence of their observed outflowing Hα filaments with giant radio lobes (*Lynds*, 1961). Since then, radio halos have been found to be ubiquitous in starforming galaxies, as revealed by the CHANG-ES VLA survey of edge-on spirals (*Irwin et al.*, 2019). Spirals in cluster environments which have enhanced mass loss due to interaction with the ICM also exhibit enhanced radio emission (*Murphy et al.*, 2009; *Vollmer et al.*, 2013). Together these observations suggest high energy, charged particles gyrating along magnetic field lines – cosmic rays – may play a role in driving galactic outflows.

1.5 A Brief Primer on Cosmic Rays

About one hundred years ago, shortly after the discovery of radioactivity, Theodor Wulf measured a higher flux of radiation at the top of the Eiffel tower compared to its base (*Wulf*, 1910). The diminishing flux with depth in a lake suggested the radiation source was not emanating from the Earth (*Pacini*, 1912). After an extensive hydrogen balloon campaign with somewhat more advanced detectors, Victor Hess confirmed the discovery of a cosmic source of the high-energy radiation (*Hess*, 1912). Shortly thereafter, an increase in flux from equatorial latitudes towards the tropics as a result of deflection by the geomagnetic field suggested this cosmic 'radiation' is actually composed of high energy charged particles.

Great strides have been made in the past hundred years in determining the composition of cosmic rays, which is observed to be energy-dependent (*Grenier et al.*, 2015). Protons dominate the low energy ~GeV - TeV component with an increasing fraction of Helium nuclei eventually dominating above roughly 10 TeV and Iron nuclei dominate the highest energies ~EeV (*Thoudam et al.*, 2016)[2]. However, the near-isotropy observed in the arrival direction distribution of cosmic rays[3] (after removing the dipole component resulting from the Earth's motion with respect to the Galaxy, *Nagashima et al.* 1998) has made the determination of the source of cosmic rays more difficult.

If the injection radius (that is, the region within which particles are being accelerated via cyclotron or similar processes) must be less than the particle gyroradius[4] (the classical Hillas criterion; *Hillas* 1984, which however can be circumvented e.g.,

---

[2] Note that leptons contribute roughly 10% at GV rigidities and become a largely negligible contribution at higher energies, as are antimatter at all energies.

[3] I studied the ability of local turbulent magnetic fields to explain the small-scale anisotropies, which I finished at the beginning of my PhD. See *COSMIC-RAY SMALL-SCALE ANISOTROPIES AND LOCAL TURBULENT MAGNETIC FIELDS* by Lopez-Barquero, Farber, Desiati & Lazarian 2016.

[4] The gyroradius (or Larmor radius) is the radius of a charged particle gyrating along a magnetic field due to the Lorentz force.

via wakefield acceleration, *Tajima and Dawson* 1979) then cosmic rays up to ∼PeV energies may be accelerated in the Galaxy while particles of much higher energy must have an extragalactic origin, in putative agreement with the anisotropy of the high-energy cosmic rays correlating with nearby AGN positions (*Collaboration et al.* 2007). Regarding the low energy cosmic rays, which carry the majority of the energy density (∼GeV), *Fermi* γ-ray observations suggest supernova remnants accelerate them. Theoretically, other sources of shocks such as massive stellar winds and the Galactic wind termination shock may also act as sources for cosmic rays (*Blandford and Eichler*, 1987; *Bustard et al.*, 2017).

Since the gyroradius (∼AU) of GeV cosmic rays is much smaller than the coherence length[5] of the magnetic field (∼pc) , cosmic rays gyrate along the interstellar magnetic field. As such, cosmic rays scatter off hydromagnetic waves, efficiently isotropizing the cosmic-ray pitch angle. Cosmic rays with energies $\gtrsim 100\,\mathrm{GeV}$ interact with magnetic waves primarily driven by extrinsic turbulence whereas lower energy cosmic rays self-excite the waves they scatter off of as a result of the streaming instability (*Zweibel*, 2013). The streaming instability occurs as a result of cosmic rays resonantly interacting with magnetic perturbations with similar amplitude to the cosmic rays' gyroradius. Cosmic rays therefore transfer their energy to the waves, although this growth mechanism is balanced by various damping terms to achieve marginal stability of the waves. While individual cosmic ray particles travel at nearly the speed of light, the distribution of cosmic rays is limited to roughly the Alfvén speed via scattering off magnetic perturbations cosmic rays self-excite. Since magnetic perturbations largely travel at the Alfvén speed, the cosmic ray distribution is similarly limited in its transport to the Alfvén speed. Thus cosmic rays can collisionlessly heat the gas as mediated by the excitation and damping of hydromagnetic waves, potentially explaining the observed electron density profile in the Galaxy (*Reynolds et al.*, 1999;

---

[5] That is, the average distance a magnetic wave can travel before the coherent wave packet decays e.g., due to scattering with other wave packets.

Wiener et al., 2013, ; Holguin et al., in prep.).

Despite GeV cosmic-ray transport being dominated by the streaming instability, propagation models frequently resort to simpler diffusive transport models (*Grenier et al.*, 2015). Since cosmic rays have sufficient energy to drive nuclear processes during collision with interstellar gas, the 'grammage' of unstable isotopes (produced by cosmic ray collisions) such as Boron-6 compared to stable isotopes such as Carbon-12, constrain the time cosmic-rays interact with the interstellar medium. That is, observations constrain cosmic-ray diffusive transport models to an energy-dependent diffusion coefficient, D, of

$$D \approx 3 \times 10^{28} R_{GV}^{1/3} \mathrm{cm}^2 \mathrm{s}^{-1} \tag{1.2}$$

where R_{GV} is the magnetic rigidity of particles in GV (*Ptuskin*, 2006). Cosmic rays escape the galactic disk (alternatively, 'reside' in the disk) in ∼10 Myr with such a diffusion coefficient (*Strong et al.*, 2007).

Particle tracking simulations of cosmic-ray propagation (e.g., *López-Barquero et al.* 2016) find that the mean free path of cosmic rays is ∼pc. Since simulations of galaxy formation utilize resolution elements >>pc one can treat the cosmic rays as a fluid similarly to how the thermal plasma is treated as a fluid (*Batchelor and Batchelor*, 2000).

How do cosmic rays drive galactic outflows? Cosmic rays could provide an extra source of heating via the streaming instability; however, this appears to play a minor role in cold gas acceleration (*Huang et al.*, 2020). Instead, cosmic rays provide a direct source of momentum through their pressure gradient, allowing them to accelerate an arbitrarily cold wind (*Ipavich*, 1975), in contrast with thermal models that accelerate gas via heating. More recent work suggests cosmic rays act synergistically with thermal wind driving (as in *Chevalier and Clegg* 1985) to explain observed outflow properties (*Everett and Zweibel*, 2011). Indeed, the anisotropic transport of cosmic rays *along* magnetic field lines requires either thermal winds or Parker instability to initially open up magnetic field lines so that cosmic rays can interact with the more tenuous halo gas and drive a wind (*Breitschwerdt et al.*, 1991, 1993; *Heintz and Zweibel*, 2018). That is, cosmic rays escaping the disk due to diffusive transport set up a pressure gradient between the disk and the halo. The pressure gradient then acts on tenuous halo gas driving that material which subsequently modifies the upstream flow in the disk together with the thermal feedback operating more principally at small scale heights in the interstellar medium. The most advanced recent galaxy formation models suggest cosmic rays dominate the pressure in galactic halos and can help explain observations of the cold CGM (*Ji et al.*, 2020), yet agreement with X-ray observations remains to be determined.

1.6 Thesis Outline

In Chapter 2, we investigate the impact of cosmic ray transport on their ability to drive galactic winds. *Farber et al.* (2018) included the first 3D magnetohydrodynamic galaxy evolution simulations to consider a diffusion coefficient that depended on local properties of the interstellar medium and halo. Wind properties depend sensitively on cosmic ray transport.

In Chapter 3, we 'zoom-in' to determine the survival of individual clouds of cold gas in a hot wind (*Farber and Gronke*, 2021). In contrast to previous work considering $\sim 10^4$ K clouds of neutral gas, we explore the temperature-dependence of the cold phase on cloud survival and include dust modeled as tracer particles.

In Chapter 4, we 'zoom-out' to full galactic scales and consider the impact of cosmic rays on ram pressure stripping, acting synergistically with galactic outflows. We include face-on and edge-on orientations of the galactic velocity vector relative to the ICM with respect to the disk spin axis, including an isolated galaxy case for comparison. These simulations include an improved stellar feedback implementation, compared to *Farber et al.* (2018), injecting the proper amount of momentum despite not resolving the Sedov-Taylor phase of supernovae. Our results suggest that recent observations of the high AGN fraction and moderately enhanced star formation rate in cluster spirals may place novel constraints on cosmic ray transport and calorimetry.

In Chapter 5, we summarize and conclude with interesting avenues for future progress on the multiscale nature of multiphase outflows: (1) highly idealized single-cloud acceleration studies with more rigorous comparison to observed systems, (2) constraining cosmic-ray transport using the observed anticorrelation between radio halo scale height and gas surface density (*Schmidt et al.*, 2019), and (3) a detailed cross-examination of resolved radio maps of cluster spirals compared to that expected from high-resolution simulations. While truth rings clearly from the eminent Lord Rutherford's quip "All science is either physics or stamp collecting" we would add that *theorizing is either concerned with observable phenomena, else philosophizing.*

CHAPTER II

The Impact of Cosmic-Ray Transport on Galactic Winds

2.1 Preface

This chapter is adapted from work of the same title appearing in the Astrophysical Journal, Volume 856, 112 (*Farber et al.*, 2018). I am the lead author, and it is coauthored by M. Ruszkowski, H.-Y. K. Yang, and E. G. Zweibel. My contributions include performing the simulations and analysis, while M. Ruszkowski, H.-Y. K. Yang, and E. G. Zweibel contributed invaluably to modelling ion-neutral damping from the perspective of diffusive cosmic-ray transport, as well as ideas for analysis. Note that I contributed code for the Townsend exact integration radiative cooling scheme to "Role of cosmic-ray streaming and turbulent damping in driving galactic winds" by F. Holguin, M. Ruszkowski, A. Lazarian, R. Farber, and H.-Y. K. Yang, published in Monthly Notices of the Royal Astronomical Society 2019, Volume 490, 1271.

2.2 Abstract

The role of cosmic rays generated by supernovae and young stars has very recently begun to receive significant attention in studies of galaxy formation and evolution due to the realization that cosmic rays can efficiently accelerate galactic winds. Microscopic cosmic ray transport processes are fundamental for determining the efficiency of cosmic ray wind driving. Previous studies focused on modeling of cosmic ray transport either via constant diffusion coefficient or via streaming proportional to the Alfvén speed. However, in predominantly cold, neutral gas, cosmic rays can propagate faster than in the ionized medium and the effective transport can be substantially larger; i.e., cosmic rays can decouple from the gas. We perform three-dimensional magnetohydrodynamical simulations of patches of galactic disks including the effects of cosmic rays. Our simulations include the decoupling of cosmic rays in the cold, neutral interstellar medium. We find that, compared to the ordinary diffusive cosmic ray transport case, accounting for the decoupling leads to significantly different wind properties such as the gas density and temperature, significantly broader spatial distribution of cosmic rays, and larger wind speed. These results have implications for X-ray, γ-ray and radio emission, and for the magnetization and pollution of the circumgalactic medium by cosmic rays.

2.3 Introduction

Galactic winds are observed ubiquitously in star-forming galaxies and significantly affect their chemical and dynamical evolution (*Veilleux et al.*, 2005). Galactic winds redistribute angular momentum, aiding in the formation of extended disks (*Brook et al.*, 2011; *Übler et al.*, 2014), help to produce large-scale magnetic fields in dwarf galaxies (*Moss and Sokoloff*, 2017), and pollute the intergalactic medium with metals (*Steidel et al.*, 2010; *Booth et al.*, 2012).

Additionally, most galaxies are missing a large fraction of baryons compared to the cosmological average (*Bell et al.*, 2003). Models matching observed luminosity functions to simulated halo mass functions find that 20% of the baryons are accounted for in L_* galaxies, and that this fraction decreases rapidly for both more and less massive galaxies (*Guo et al.*, 2010). This suggests that the efficiency of converting baryons into stars is a strong function of halo mass.

The discrepancies between halo and stellar properties, "the missing baryons problem," constitutes an outstanding challenge in galaxy formation. Galactic winds can possibly solve the missing baryons problem by ejecting baryons out of galaxies. For galaxies more massive than L_*, active galactic nuclei likely dominate the energetics of the outflows (e.g., *Croton et al.*, 2006), while in less massive galaxies galactic winds are likely driven by stellar feedback (*Larson* 1974, *Chevalier and Clegg* 1985, *Dekel and Silk* 1986).

In the standard model of supernovae driven galactic winds (*Chevalier and Clegg*, 1985), thermal energy is injected into the gas, launching it ballistically and entraining denser gas as it is flung out of the galaxy. Thermally driven winds may explain the superwinds observed in starburst galaxies such as M82 (*Bustard et al.* 2016). However, results from high-resolution simulations demonstrated that such models may inject significant amounts of energy and launch metals out of galaxies but fail to expel a significant amount of mass into the intergalactic medium (*Mac Low et al.* 1994; *Melioli et al.* 2013). Additionally, *Steidel et al.* (2010) found the kinematic features of Lyman-break galaxies best match models in which the gas velocity increases with distance to at least 100 kpc. This result is also difficult to reconcile with the thermal feedback model. The insufficiencies of purely thermally driven winds hint at the importance of additional stellar feedback processes, such as cosmic rays (*Boulares and Cox* 1990; *Breitschwerdt et al.* 1993; *Uhlig et al.* 2012).

Cosmic rays can be accelerated by means of the diffusive acceleration mechanism operating in the shocks of supernova remnants (*Blandford and Eichler* 1987; *Caprioli* 2015) and in the winds from massive stars (*Bykov* 2014). Cosmic rays exert pressure that is in rough equipartition with magnetic and dynamical pressures in the interstellar medium (*Zweibel and Heiles* 1997; *Beck* 2001; *Cox* 2005), suggesting their dynamical importance. In particular, cosmic rays can provide pressure support against self-gravitating clouds, suppressing star formation (*Jubelgas et al.* 2008; *Pfrommer et al.* 2017a). Additionally, *Fermi* γ-ray observations of starburst galaxies M82 and NGC 253 imply cosmic ray energy densities roughly two magnitudes higher than in the Milky Way (*Paglione and Abrahams* 2012; *Yoast-Hull et al.* 2013; *Yoast-Hull et al.* 2014).

Cosmic rays escape the Galactic disk in $\sim$10 Myr (*Strong et al.*, 2007). Compared to the thermal gas, cosmic rays can be relatively free of energy losses, which together with their fast escape from the disk, suggests that cosmic rays may efficiently transport supernova energy to regions occupied by tenuous gas above the disk, which they can accelerate into a wind (*Hanasz et al.* 2013).

Early work by *Ipavich* (1975) considered the emission of magnetohydrodynamic (MHD) waves by super-Alfvénic cosmic rays. These waves enable cosmic rays to be coupled to the thermal gas. A steady-state, spherically symmetric, hydrodynamic treatment by *Ipavich* (1975) suggested that cosmic rays could drive outflows at rates $\gtrsim 1\ \mathrm{M}_{\odot}/\mathrm{yr}$ from a typical galaxy. *Breitschwerdt et al.* (1991) extended the work by *Ipavich* (1975) by including the streaming of cosmic rays along large scale magnetic fields and found that mass outflow rates of $\sim 1\ \mathrm{M}_{\odot}/\mathrm{yr}$ are possible in Milky Way-like galaxies. *Everett et al.* (2008) further extended this work by combining cosmic ray and thermal pressure under Milky Way conditions and found that both thermal and cosmic ray pressures were essential for wind driving in the Milky Way.

Recently, 3D numerical studies of cosmic ray winds have found that wind properties depended sensitively on the details of cosmic ray transport. This was demonstrated in both Eulerian grid hydrodynamic (*Uhlig et al.* 2012; *Booth et al.* 2013; *Salem and Bryan* 2014) and MHD simulations (*Hanasz et al.* 2013; *Ruszkowski et al.* 2017) as well as unstructured moving mesh simulations (*Pakmor et al.* 2016a; *Simpson et al.* 2016; *Pakmor et al.* 2016b; *Pfrommer et al.* 2017a; *Jacob et al.* 2018).

In predominantly cold, neutral gas, cosmic rays can propagate faster than in the ionized medium and the effective transport can be substantially larger; i.e., cosmic rays can decouple from the gas. In this work, we study the consequences of this decoupling and show that it has a significant impact on the properties of cosmic ray driven galactic winds. In Section 2, we delineate the numerical methods and treatment of physics in our simulations. In Section 3, we present our results, and in Section 4 we conclude.

2.4 Methods

We model cosmic rays with a two-fluid model (e.g., *Salem and Bryan* 2014; *Ruszkowski et al.* 2017), in which cosmic rays take the form of an ultra-relativistic ideal fluid with an adiabatic index $\gamma_{\rm cr} = 4/3$ and the thermal gas is characterized by an adiabatic index $\gamma = 5/3$. We include advection of cosmic rays, dynamical coupling between cosmic rays and the gas, and model the transport of cosmic rays relative to the gas via anisotropic diffusion of cosmic rays along magnetic field lines rather than via the streaming instability (see Section 2.4.3). We model the effect of cosmic rays decoupling from the cold, neutral interstellar medium (ISM) via a temperature-dependent diffusion coefficient (see Section 2.4.3). Additionally, we include star formation and feedback, self-gravity of the gas, and radiative cooling. We solve the following equations:

$$\frac{\partial \rho}{\partial t} + \boldsymbol{\nabla} \cdot (\rho \mathbf{u}) = -\dot{m}_{\rm form} + f_* \dot{m}_{\rm feed}, \tag{2.1}$$

$$\frac{\partial \rho \mathbf{u}}{\partial t} + \boldsymbol{\nabla} \cdot \left(\rho \mathbf{u}\mathbf{u} - \frac{\mathbf{B}\mathbf{B}}{4\pi} \right) + \boldsymbol{\nabla} p_{\rm tot} = \rho \mathbf{g} + \dot{p}_{\rm SN}, \tag{2.2}$$

$$\begin{aligned} \frac{\partial e}{\partial t} + \boldsymbol{\nabla} \cdot \left[(e + p_{\rm tot})\mathbf{u} - \frac{\mathbf{B}(\mathbf{B} \cdot \mathbf{u})}{4\pi} \right] = \\ \rho \mathbf{u} \cdot \mathbf{g} + \boldsymbol{\nabla} \cdot (\boldsymbol{\kappa}(T) \cdot \boldsymbol{\nabla} e_{\rm cr}) - C + H_{\rm SN}, \end{aligned} \tag{2.3}$$

$$\frac{\partial \mathbf{B}}{\partial t} - \boldsymbol{\nabla} \times (\mathbf{u} \times \mathbf{B}) = 0, \tag{2.4}$$

$$\begin{aligned} \frac{\partial e_{\rm cr}}{\partial t} + \boldsymbol{\nabla} \cdot (e_{\rm cr}\mathbf{u}) = & - p_{\rm cr}\boldsymbol{\nabla} \cdot \mathbf{u} + H_{\rm SN} \\ & + \boldsymbol{\nabla} \cdot (\boldsymbol{\kappa}(T) \cdot \boldsymbol{\nabla} e_{\rm cr}), \end{aligned} \tag{2.5}$$

$$\Delta\phi = 4\pi G \rho_b \tag{2.6}$$

where ρ is the gas density, $\mathbf{u}$ is the gas velocity, $\dot{m}_{\rm form}$ is a density sink term representing star formation, $f_*\dot{m}_{\rm feed}$ is a density source term representing stellar winds and supernovae (see Section 2.4.4), $\mathbf{B}$ is the magnetic field, $p_{\rm tot}$ is the sum of the gas ($p_{\rm th}$), magnetic, and cosmic ray ($p_{\rm cr}$) pressures, $\mathbf{g} = -\boldsymbol{\nabla}\phi + \mathbf{g}_{\rm NFW}$ is the gravitational acceleration (including contributions from self-gravity of gas and stars: $-\boldsymbol{\nabla}\phi$ and dark matter: $g_{\rm NFW}$; see Section 2.4.1), $\dot{p}_{\rm SN}$ is the momentum injection from stellar winds and supernovae, $e = 0.5\rho\mathbf{u}^2 + e_g + e_{\rm cr} + B^2/8\pi$ is the total energy density (where e_g is the thermal energy density), $\boldsymbol{\kappa}(T)$ is the temperature-dependent diffusion coefficient (see Section 2.4.3), $e_{\rm cr}$ is the cosmic ray energy density, C is the radiative cooling term (see Section 2.4.2), $H_{\rm SN}$ is the supernova heating term (see Section 2.4.4), and ρ_b is the total (gas and stars) baryon density.

We use the adaptive-mesh refinement MHD code FLASH4.2 (*Fryxell et al.*, 2000; *Dubey et al.*, 2008) as extended to include cosmic rays (*Yang et al.* 2012; *Yang et al.* 2013; *Yang and Ruszkowski* 2017; *Ruszkowski et al.* 2017) to solve the above equations. We utilize the directionally unsplit staggered mesh (USM) solver (*Lee and Deane*, 2009; *Lee*, 2013). The USM solver is a finite-volume, high order Godunov scheme that utilizes constrained transport to ensure divergence-free magnetic fields.

Due to computational constraints, we employ sound speed limiting. That is, we set a ceiling to the thermal and cosmic ray energy so that the timestep does not become unfeasibly small. Specifically, we impose an upper limit on the generalized sound speed

$$c_s = \left(\frac{\gamma p_{\rm th} + \gamma_{\rm cr} p_{\rm cr}}{\rho}\right)^{1/2}. \tag{2.7}$$

In our fiducial runs, we limit c_s to $c_{s,\rm lim} = 10^3$ km s^{-1}, but we have additionally run test cases for $c_{s,\rm lim} = 2 \times 10^3$ km s^{-1} and found no significant differences in the star formation rates (c.f., *Salem and Bryan* (2014)).

For the most expensive simulation, which employs the decoupling mechanism (Run DEC, cf. Sections 2.4.3 & 2.5), we use a raised density floor of 10^{-3} cm^{-3}, which effectively limits the Alfvén speed. In test cases that use reduced diffusion coefficients (which are computationally easier), we found no difference in the results between runs that used the raised density floor of 10^{-3} cm^{-3} compared to the fiducial density floor 5×10^{-7} cm^{-3}.

2.4.1 Gravity

We include self-gravity of baryons (gas and stars) and solve the Poisson equation using the Barnes-Hut tree solver (*Barnes and Hut*, 1986) implemented in FLASH4.2 by Richard Wünsch (*Wünsch et al.* 2017). This solver allows us to use mixed boundary conditions (see Section 2.4.5).

In addition to self-gravity, we include acceleration in the z-direction due to dark matter. This component of the gravitational field assumes that dark matter is distributed according to the Navarro-Frenk-White profile (*Navarro et al.*, 1997) and has the following form:

$$g_{\rm NFW}(z) = -\frac{GM_{200}z}{|z|^3}\frac{\ln(1+x) - x/(1+x)}{\ln(1+c) - c/(1+c)} \tag{2.8}$$

where z is height from the midplane, G is the universal gravitational constant, M_{200} is the virial mass of the halo, $x = |z|c/r_{200}$, c is the halo concentration parameter, and r_{200} is the virial radius defined as the radius of a sphere within which the average density exceeds the critical density at redshift zero by a factor of 200; i.e., $M_{200} = \frac{4}{3}\pi r_{200}^3 200\rho_{\rm crit}$. See Table 1 for the parameter values used in our simulations.

2.4.2 Radiative Cooling

We implemented the *Townsend* (2009) exact cooling method using the *Rosen and Bregman* (1995) piecewise power law form of the cooling function, which extends down to a floor temperature of 300 K. The *Rosen and Bregman* (1995) cooling function is an approximation to the *Dalgarno and McCray* (1972), and *Raymond et al.* (1976) radiative cooling functions and is given by

$$\Lambda(T) = \begin{cases} 0 & \text{if T} < 300 \\ 2.2380 \times 10^{-32} T^{2.0} & \text{if } 300 \leq \text{T} < 2000 \\ 1.0012 \times 10^{-30} T^{1.5} & \text{if } 2000 \leq \text{T} < 8000 \\ 4.6240 \times 10^{-36} T^{2.867} & \text{if } 8000 \leq \text{T} < 10^5 \\ 1.7800 \times 10^{-18} T^{-0.65} & \text{if } 10^5 \leq \text{T} < 4 \times 10^7 \\ 3.2217 \times 10^{-27} T^{0.5} & \text{if } 4 \times 10^7 \leq \text{T}, \end{cases} \tag{2.9}$$

where T is the gas temperature in K and $\Lambda(T)$ is in the units of erg cm^3 s^{-1}. The above cooling function is approximately correct for gas of solar abundance, which is completely ionized at 8000 K. Unlike explicit or implicit solvers, the Townsend integration scheme is exact and does not impose restrictions on the cooling timestep. Our tests confirm that the gas temperature evolution computed using this method follows, down to machine precision, the evolution predicted analytically (see Appendix 2.7).

Table 2.1: Model parameters

Halo	
$M_{200}^{(1)}$	$10^{12}\mathrm{M}_\odot$
$c^{(2)}$	12
Disk	
$\rho_o^{(3)}$	$5.24\ \times 10^{-24}$ g cm^{-3}
$z_o^{(4)}$	0.325 kpc
$\Sigma_o^{(5)}$	100 $\mathrm{M}_\odot$ pc^{-2}
$T_o^{(6)}$	10^4 K
$B_o^{(7)} = B_{o,x}$	1 μG
Star Formation	
$n_{\mathrm{thresh}}^{(8)}$	10 cm^{-3}
$T_{\mathrm{floor}}^{(9)}$	300 K
$m_{*,\mathrm{min}}^{(10)}$	10^5 $\mathrm{M}_\odot$
$\epsilon_{\mathrm{SF}}^{(11)}$	0.05
Stellar Feedback	
$f_*^{(12)}$	0.25
$f_{cr}^{(13)}$	0.1
$\epsilon_{\mathrm{SN}}^{(14)}$	$10^{51}\mathrm{erg}/(\mathrm{M}_{\mathrm{sf}}\mathrm{c}^2)$
$M_{\mathrm{sf}}^{(15)}$	100 $\mathrm{M}_\odot$

Notes. From top to bottom the rows contain: (1) Halo mass; (2) Concentration parameter; (3) Initial midplane density; (4) Initial scale height of the gas disk; (5) Initial gas surface density; (6) Initial temperature; (7) Initial magnetic field strength; (8) Gas density threshold for star formation; (9) Floor temperature; (10) Minimum stellar population particle mass; (11) Star formation efficiency; (12) Fraction of stellar mass returned to the ISM; (13) Fraction of supernova energy bestowed unto cosmic rays; (14) Supernova energy per rest mass energy of newly formed stars; (15) Rest mass energy of newly formed stars per supernova.

2.4.3 Cosmic ray decoupling from the cold interstellar medium

Cosmic rays can be efficiently confined to hot plasmas by scattering off self-excited hydromagnetic waves (*Kulsrud and Pearce* 1969; *Kulsrud* 2005). The relative drift speed of the cosmic rays with respect to the plasma v_D occurs at the local Alfvén speed v_A, unless the hydromagnetic waves are damped. *Kulsrud and Cesarsky* (1971) have shown that ion-neutral damping can significantly boost the relative drift velocity of cosmic rays. Moreover, as the ionization fraction decreases, the Alfvén speed $v_A \propto$ (density of ionized particles)$^{-1/2}$ increases. Both of these effects lead to the decoupling of cosmic rays from the low-temperature ISM.

Note that turbulent damping (*Farmer and Goldreich* 2004; *Lazarian* 2016; *Holguin et al.* 2019), linear Landau damping (*Wiener et al.* 2018), and nonlinear Landau damping (*Kulsrud* 2005) will also increase the relative drift velocity of cosmic rays. All of these damping mechanisms (including ion-neutral damping explored in this work) dissipate cosmic ray streaming energy into heat. This will affect the equation of state, which is different for the waves (depending on the Alfvén Mach number), cosmic rays, and gas, an effect we neglect in the present work.

We note that even in the presence of cosmic rays in the cold ISM, the ionization fraction in most of this phase should be low because it is mostly the low-energy (tens of MeV) cosmic rays that are responsible for the ionization of hydrogen. The ionization cross section of these cosmic rays is very high (*Draine*, 2011) and consequently they typically do not travel far from the sites of their injection. This allows higher energy cosmic rays, that carry most of the energy of the cosmic ray fluid, to propagate in weakly ionized cold ISM where the coupling is relatively weak.

The dynamics of cosmic ray decoupling from the gas is governed by kinetic theory, yet we model cosmic rays as a fluid in order to perform simulations of tractable duration. The expectation from kinetic theory is that cosmic ray pressure and energy density tend toward constant values in space when decoupling operates (cf. *Everett* *and Zweibel* 2011, who also model decoupling via a large diffusion coefficient). We model the decoupling mechanism in the "extrinsic turbulence" framework (*Zweibel*, 2013) in which cosmic rays scatter off waves generated by turbulence driven by external sources rather than the waves generated by the streaming instability. In this model cosmic ray transport proceeds via diffusion rather than streaming, and cosmic rays exert a pressure on the gas but do not heat it (*Zweibel*, 2017)[1].

Cosmic ray streaming and streaming heating was previously investigated in detail in *Ruszkowski et al.* (2017). They found that the streaming speed (i.e., the boost factor f > 1) significantly affects wind launching, while whether or not streaming heating is included does not have any noticeable impacts on the results (*Ruszkowski et al.* 2017, private communication). In this work, we focus on the influence of decoupling on the transport speed.

In order to emulate the decoupling effect in the fluid model, we adopt a simple treatment in which the parallel diffusion coefficient is amplified to large values in low-temperature regions. This has the same effect of increasing the effective transport speed in the low-temperature gas as discussed above. As such, it will smooth the gradients in cosmic ray pressure and energy density, matching the expectations from kinetic theory.

The parallel diffusion coefficient $\kappa_{||}$ can be expressed as $\kappa_{\rm Bohm}/\epsilon$, where ϵ is the ratio of the scattering frequency of cosmic rays on the waves generated by external turbulence to the gyrofrequency c/r_g and $\kappa_{\rm Bohm} = \frac{1}{3} r_g v_p$ is the Bohm diffusion coefficient, r_g is the gyroradius, and v_p is the particle speed (*Schlickeiser*, 1989; *Enßlin*, 2003). The scattering frequency depends on the properties of the MHD turbulence on the scales comparable to r_g. Since we are working in the "extrinsic turbulence" model, the source of the magnetic field perturbations capable of deflecting cosmic rays is most likely compressive waves generated by the Goldreich-Sridhar cascade down to

---

[1] We have in mind here collisionless heating due to excitation and damping of Alfvén waves; the low energy cosmic rays which ionize the gas also collisionally heat it.

this small scale (*Yan and Lazarian*, 2004). Frequent cosmic ray scattering on these perturbations reduces field-aligned diffusion. The scattering frequency is proportional to $\delta B^2/B^2$, where δB^2 is the power in the magnetic fluctuations corresponding to the scale equal to r_g. Thus, $\kappa_{||} \propto B^2/\delta B^2$, and we assume that when significant wave damping is present in weakly ionized regions, the amplitude of the magnetic field perturbations decreases, and the parallel diffusion coefficient is boosted.

As an illustration that increasing the diffusion coefficient has the desired effect of flattening the cosmic ray energy density distribution, let us consider a one-dimensional and steady state form of the cosmic ray energy density equation with spatially constant velocity v_0. For the sake of simplicity, we also neglect supernova heating in this example. In this case, integration of Eq. (5) over z yields

$$\kappa \frac{de_{\rm cr}}{dz} - v_0 e_{\rm cr} = const. \tag{2.10}$$

Let $\kappa = \kappa_0 e^{z/L}$. In this example, low-temperature regions correspond to large values of z. The solution of Eq. (10), which satisfies boundary condition $e_{\rm cr} = e_{\rm cr,0}$ at $z = 0$, is

$$e_{\rm cr} = e_{\rm cr,0} + \frac{\kappa_0}{v_0} \frac{de_{\rm cr}}{dz}\bigg|_0 \left[\exp\left\{\frac{v_0 L}{\kappa_0}\left(1 - e^{-z/L}\right)\right\} - 1\right]. \tag{2.11}$$

For $z \gg L$, $e_{\rm cr}$ approaches a constant as required to match the behavior expected from kinetic theory. Moreover, if $v_0 L/\kappa_0 \ll 1$, the constant value is $e_{\rm cr} \approx e_{\rm cr}(0)$ as expected. On the other hand, in the limit of $z \ll L$,

$$e_{\rm cr} = e_{\rm cr,0} + \frac{\kappa_0}{v_0} \frac{de_{\rm cr}}{dz}\bigg|_0 \left[\exp\left\{\frac{v_0 z}{\kappa_0}\right\} - 1\right] \tag{2.12}$$

which, as expected, matches the solution of an advection-diffusion equation with a constant diffusion coefficient.

In order to capture the effect of decoupling, we implement in the code the following simple dependence of the diffusion coefficient on the gas temperature

$$\kappa_{\parallel}(T) = \begin{cases} 1.0 \times 10^{29}\ \mathrm{cm}^2\ \mathrm{s}^{-1} \text{ if } T < 10^4 K \\ 3.0 \times 10^{27}\ \mathrm{cm}^2\ \mathrm{s}^{-1} \text{ if } T \geq 10^4 K, \end{cases} \tag{2.13}$$

and set $\kappa_{\perp} = 3 \times 10^{26}$ cm^2 s^{-1} for all temperatures. Here, $\kappa_{\parallel}$ and $\kappa_{\perp}$ denote the diffusion coefficient for cosmic ray transport parallel and perpendicular to the magnetic field, respectively.

The adopted cold gas value of the diffusion coefficient is representative of the values inferred for the Galaxy, but the high-temperature value of the coefficient is lower. However, our volume-weighted diffusion coefficient is expected to lie in between these limits and is comparable to that adopted by *Booth et al.* (2013), *Salem and Bryan* (2014), and *Ruszkowski et al.* (2017). This average value is somewhat smaller than the Galactic value (c.f., *Strong and Moskalenko* 1998). However, the level of diffusion inferred from observations depends on the assumptions of the models used to quantify it. Specifically, diffusion coefficients derived from the GALPROP propagation model assume spatially constant diffusion coefficient and/or often assume absence of winds. Interestingly, *Ptuskin et al.* (1997) (see also *Zirakashvili et al.* 1996) consider an analytic model that includes both of these effects. They study cosmic ray driven winds in which they treat streaming in the diffusion approximation and include decoupling due to ion-neutral damping. They find that the level of diffusion required for consistency with the Galactic data is only $\sim 10^{27}$ cm^2 s^{-1} outside regions close to the disk midplane, and significantly higher close to the disk where decoupling operates. The vertical velocity gradient of the cosmic ray accelerated wind in their model is large and similar to the values predicted by simulations (e.g., *Salem and Bryan* 2014). Furthermore, *Jóhannesson et al.* (2016) (see also *Trotta et al.* 2011) demonstrate that propagation parameters derived from low mass isotope data differ significantly from those based on light elements, e.g., B and C, suggesting that these species probe different locations of the ISM where cosmic ray transport may occur at different rates, though their GALPROP models neglect winds. Individual supernova remnants have also been used to put constraints on the diffusion coefficient. These studies suggested that the locally measured diffusion coefficient can be around $\sim 10^{26}$ cm^2/s to $\sim 10^{27}$ cm^2 s^{-1} when isotropic diffusion is assumed and somewhat larger $\kappa_{||} \sim 3 \times 10^{27}$ cm^2 s^{-1}(at 1 GeV) when anisotropic diffusion is assumed (e.g., *Nava and Gabici* 2013 and references therein).

Our approximate treatment assumes that the gas is fully ionized above 10^4 K. The ionization level changes dramatically near this temperature threshold, and we note that the results are only weakly sensitive to the exact choice of this threshold. Consequently, the exact form of the cooling function, and specifically its dependence on the gas ionization near this critical temperature, is not critical to our conclusions.

While we implement decoupling by boosting $\kappa_{||}$ by a factor of thirty in regions with $T < 10^4$ K, we experimented with larger boost factors and found that they did not significantly affect the results. Since the computational timestep is inversely proportional to the diffusion coefficient, we decided to use smaller boost factors to accelerate the computations. Tests of the anisotropic diffusion module are presented in Appendix 2.8.

2.4.4 Star Formation and Feedback

We follow the star formation prescription of (*Cen and Ostriker* 1992; cf. *Tasker and Bryan* 2006; *Bryan et al.* 2014; *Salem and Bryan* 2014; *Li et al.* 2015), in which stars form when all of the following conditions are simultaneously met: (i) gas density exceeds a threshold value of $n_{\rm thresh} = 10$ cm^{-3} (*Gnedin and Kravtsov* 2011; *Agertz et al.* 2013), (ii) flow is convergent ($\boldsymbol{\nabla} \cdot \mathbf{u} < 0$), (iii) cooling time is smaller than the dynamical time $t_{\rm dyn} = \sqrt{3\pi/(32G\rho_b)}$ or the temperature is below the floor of the cooling function (see Section 2.4.2), and (iv) the cell gas mass exceeds the local Jeans mass.

When the above conditions are met, we form a stellar population particle[2] instantaneously. The mass of the particle is $m_* = \epsilon_{\rm SF}(dt/t_{\rm dyn})\rho dx^3$, where dx is the size of the cell in which the particle was formed and $\epsilon_{\rm SF} = 0.05$ is the star formation efficiency (*Tasker and Bryan* 2006; *Ruszkowski et al.* 2017). Due to computational constraints, we prevent an exceedingly large number of stellar population particles from forming by using a minimum stellar mass $m_{*,\rm min} = 10^5$ M$_\odot$. However, even when $m_* < m_{*,\rm min}$, we still permit stars to form with a probability of $m_*/m_{*,\rm min}$ and mass of $m_* = 0.8\rho dx^3$. Whenever a stellar population particle forms, we remove its mass from the gas the moment the stellar population particle appears.

We model stellar feedback by adding to the ISM: gas at the rate of $f_*\dot{m}$, thermal energy at the rate of $(1 - f_{\rm cr})\epsilon_{\rm SN}\dot{m}c^2$, and cosmic ray energy at the rate of $f_{\rm cr}\epsilon_{\rm SN}\dot{m}c^2$, where $\dot{m} = m_*\Delta t/\tau^2 \exp(-\Delta t/\tau)$ and $\tau = \max(t_{\rm dyn}, 10{\rm Myr})$. In order to conserve baryons during this time-dependent feedback process, we reduce the stellar population particle mass at the rate of $f_*\dot{m}$. This mass exchange represents stellar mass loss due to winds and supernovae. We use $f_* = 0.25$, $f_{\rm cr} = 0.1$, and $\epsilon_{\rm SN} = 10^{51}{\rm erg}/(M_{\rm sf}c^2)$, where $\epsilon_{\rm SN}$ is the energy released by supernovae per rest mass energy corresponding to the mass in newly formed stars $M_{\rm sf} = 100$ M$_\odot$ (*Guedes et al.*, 2011; *Hanasz et al.*, 2013; *Ruszkowski et al.*, 2017), which corresponds to a *Kroupa* (2001) initial mass function. Star formation and feedback parameter choices are summarized in Table 1.

2.4.5 Simulation Setup

We simulate a slab of ISM, with box dimensions of (2 kpc)^2×40 kpc. This domain shape and size was motivated by the results of *Hill et al.* (2012), who found that an extended height was crucial in establishing a realistic halo temperature distribution

---

[2] *Nota Bene* A stellar population particle is representative of a star cluster, not an individual star.

in their simulations. We employ periodic boundary conditions on boundaries perpendicular to the disk and "diode" boundary conditions on boundaries parallel to the disk. Diode boundary conditions permit material to outflow from the simulation box but prevent infall (cf., *Sur et al.* 2016). Note that we neglect the magnetic field amplification due to rotational shear and our simulations somewhat enhance gravitational instability since we neglect differential rotation. These caveats are important to keep in mind; however, neglecting differential rotation greatly simplifies the calculation without sacrificing its main objectives.

We use static mesh refinement throughout the duration of the simulations to maximize resolution near the disk. Although using static mesh refinement possibly underestimates shock heating of the halo gas and thus the temperature of the wind, it does not affect our main conclusions (i.e., whether winds are launched since it mainly depends on what happens close to the disk, and the relative differences of wind properties among the three transport cases presented below). We achieve a maximum resolution of 31.25 pc in the disk. Beyond $|z| > 2$ kpc our resolution begins to degrade down to a minimum resolution beyond $|z| > 4$ kpc of 250 pc. One of the factors limiting the simulation timestep is the magnetic field aligned diffusion. Our maximum resolution is comparable to that achieved in *Girichidis et al.* (2016), who also included magnetic field-aligned cosmic ray diffusion but considered a lower maximum value of the diffusion coefficient.

We initialize a constant temperature of 10^4 K and a constant magnetic field of strength 1.0 μG along the (horizontal) x-direction throughout the computational volume. The initial density distribution follows a vertical density profile given by

$$\rho(z) = \begin{cases} \rho_0 \,\mathrm{sech}^2\left(\frac{z}{2z_0}\right) & \rho(z) > \rho_{\mathrm{crit}} \\ \rho_{\mathrm{crit}} & \text{otherwise} \end{cases} \tag{2.14}$$

where ρ_0 is the midplane density, z_0 is the scale height of the gas disk, and ρ_{crit} is the critical density of the universe. Normalization constant ρ_0 is obtained from the disk surface gas density $\Sigma_0 = \int_{-20\mathrm{kpc}}^{20\mathrm{kpc}} \rho(z)dz$. See Table 1 for the adopted parameter values. For a radially exponential gas distribution of $4.1 \times 10^{10}\mathrm{M}_\odot$ in baryons in a Milky Way-type galaxy with scale factor of 3.6 kpc (*Booth et al.*, 2013), the adopted gas surface density Σ_0 corresponds to the gas surface density averaged within a radius of ~10 kpc from the Galactic Center.

The initial setup is in rough hydrostatic equilibrium; that is, the density distribution is such that there would be hydrostatic equilibrium but for the gravity due to the NFW halo. However, gravity due to the NFW halo is small compared to self-gravity near the midplane. Consequently, gas rapidly accretes onto the midplane early in the simulation. We show results for times after 40 Myr, after memory of the initial condition has been forgotten.

2.5 Results and Discussion

We present results from three simulations which include self-gravity, radiative cooling, magnetic fields, star formation and feedback, and cosmic ray pressure forces, but differ in their treatment of cosmic ray transport: in run ADV cosmic rays are advected by gas motions and diffusive cosmic ray transport is neglected; in run DIF cosmic rays are advected by gas motions and additionally the anisotropic diffusion of cosmic rays along magnetic field lines with $\kappa_\parallel = 3 \times 10^{27}$ cm^2 s^{-1} and $\kappa_\perp = 3 \times 10^{26}$ cm^2 s^{-1} is included; run DEC includes cosmic ray decoupling from low-temperature ISM treated via a temperature-dependent diffusion coefficient as described in Section 2.4.3.

In Figure 2.1 we show the projected gas densities in the central $|z| < 6$ kpc at ~170 Myr for each run. In the ADV run (left panel), cosmic rays injected by supernovae are unable to efficiently drive the dense gas away from the midplane. In this case, cosmic rays remain trapped within the disk, provide additional pressure support, and thus puff up the disk. In contrast, in the DIF run (middle panel), cosmic rays are able to diffuse away from the midplane and drive the more tenuous gas located immediately above the midplane away from the disk, thus producing a wind. In the DEC run (right panel), the effects of stellar feedback are even stronger than in the DIF run – faster cosmic ray transport out of the ISM reduces cosmic ray pressure support near the midplane, which leads to enhanced star formation rate, and thus, stronger feedback. This stronger feedback, together with the fact that cosmic rays avoid dense gas in the disk due to their decoupling from the cold ISM phase and preferentially acting on more tenuous gas, leads to the formation of hot, low-density bubbles extending up to ±4 kpc away from the midplane (see right panel in Figure 2.1). The timing of the snapshots shown in Figure 2.1 corresponds to the period following the peak in star formation rate and was chosen specifically to reveal the maximum spatial extent of the hot bubbles.

Previous simulations also found that cosmic rays cannot drive winds without diffusive transport (*Jubelgas et al.* 2008, *Uhlig et al.* 2012, *Simpson et al.* 2016). However, the formation of small scale structure is resolution dependent. We performed an additional ADV simulation at 15.625 pc resolution and still found that no wind was produced. Nevertheless, it is possible that at sufficiently high resolution the thermal energy from supernovae would carve out channels in the gas density. The channels would allow the cosmic rays to escape rather than puffing up the disk. This hypothesis shall be examined by future higher resolution simulations which can better resolve high-density clumps within the disk (but this is beyond the scope of the current work).

To better understand the impact of cosmic ray decoupling on the properties of the ISM, we next consider temperature-density phase plots. Figure 2.2 shows these phase plots for $|z| < 4$ kpc (bottom row) and $|z| > 4$ kpc (top row). The left column shows results from the DIF run and the right from the DEC run. All panels correspond to 170 Myr. One of the most striking differences between these phase plots is the

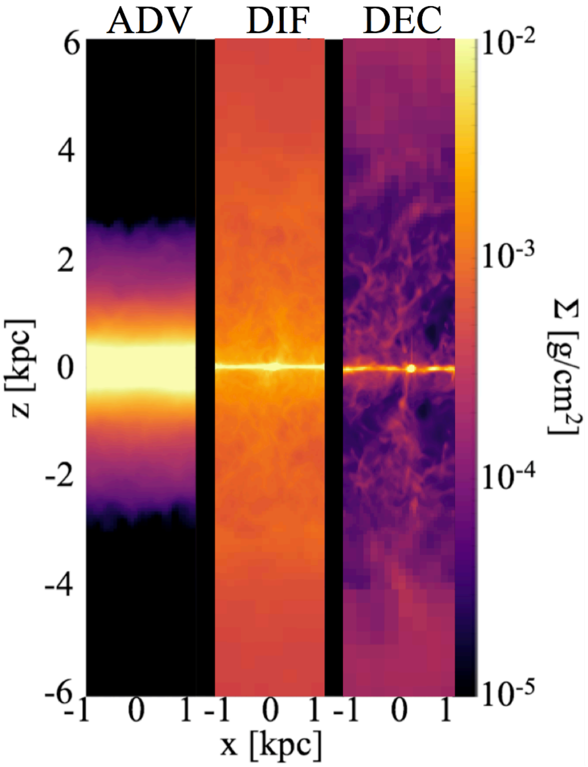

Figure 2.1: Gas mass density projections along the y direction (along the midplane) for the inner $|z| < 6$ kpc. The snapshots are taken at 170 Myr. Panels show three cases that correspond to different treatment of cosmic ray transport: ADV (no cosmic ray transport; left), DIF (magnetic field aligned diffusion; middle), and DEC (temperature-dependent magnetic field aligned diffusion to model cosmic ray decoupling in the cold ISM; right). Strong wind in the cases including transport, and the formation of large low-density cavities due to strong feedback in the DEC case, are evident.

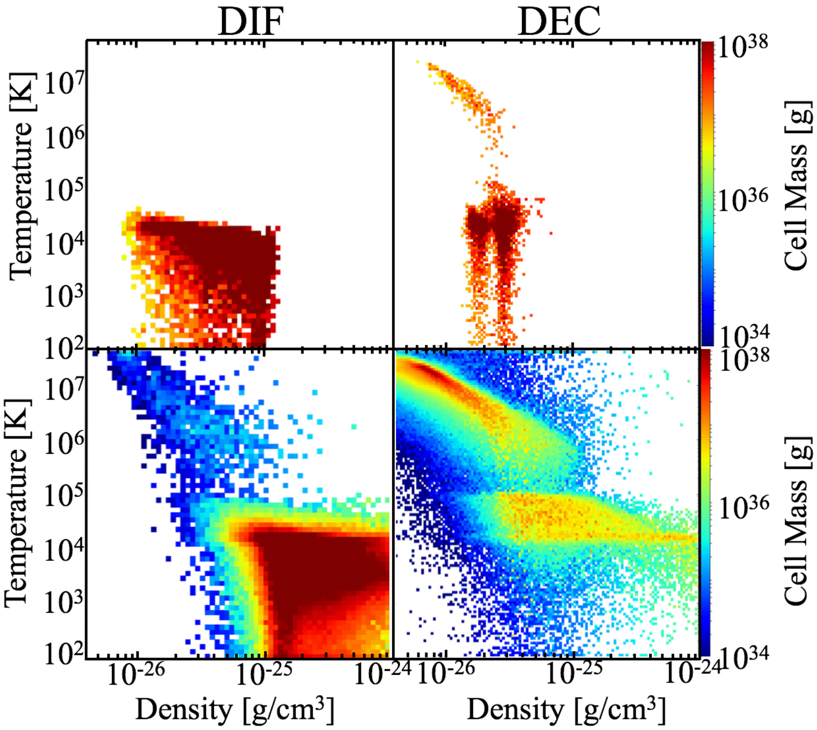

Figure 2.2: Temperature-density phase plots at 170 Myr for $|z| < 4$ kpc (bottom row) and $|z| > 4$ kpc (top row). Left column corresponds to Run DIF and the right one to Run DEC.

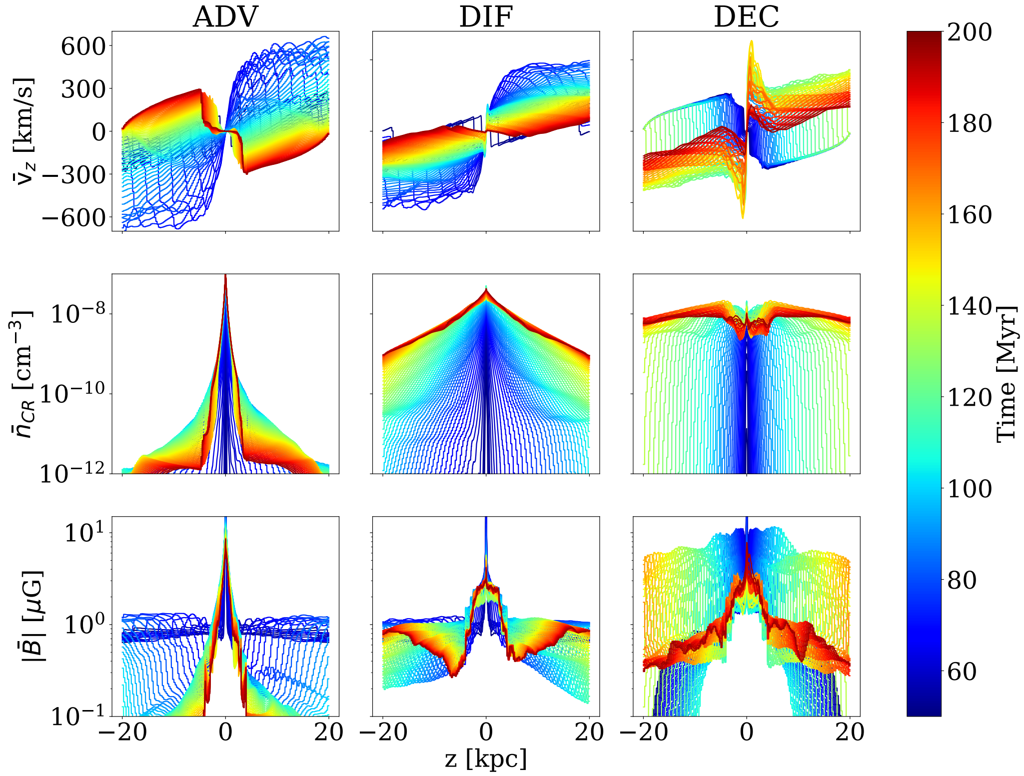

Figure 2.3: Time series of profiles of the wind velocity (top row), the cosmic ray number density (middle row), and the magnetic field strength (bottom row) as a function of height above the midplane. All three variables are volume-weighted. From left to right, columns show results for the ADV, DIF, and DEC cases. The time series span the range from 50 Myr (dark blue) to 200 Myr (dark red).

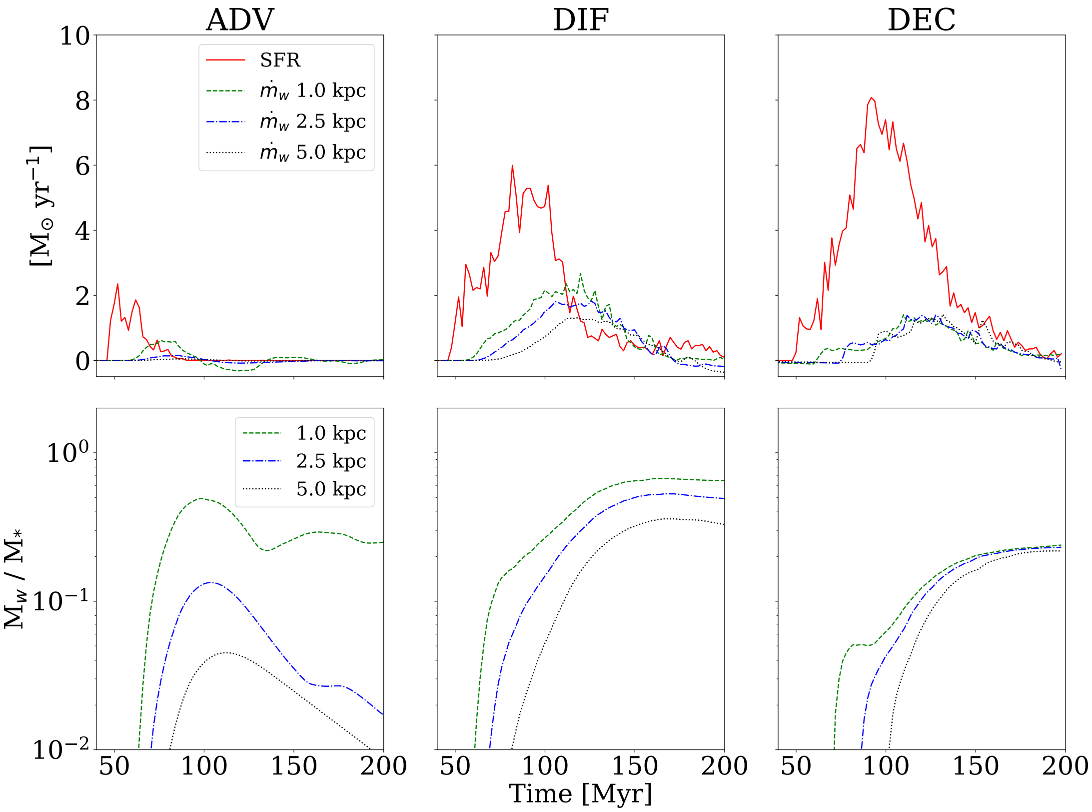

Figure 2.4: Evolution of the mass outflow rate and star formation rate (top row) and integrated mass loading ($M_{\rm wind}/M_*$) (bottom row). Mass outflow rate is measured using surfaces parallel to the disk midplane. Curves corresponding to mass outflow rates are labeled according to the heights (measured from the disk midplane) of these surfaces (see text for details).

difference between the phase plots corresponding to $|z| < 4$ kpc. These plots reveal that the low density bubbles formed in the DEC case (see right panel in Figure 2.1) are very hot ($10^6 - 10^7$ K). This feature is absent in the DIF case. We verified that the hot underdense bubbles are present throughout the $|z| < 4$ kpc region rather than being confined to smaller distances from the midplane. These results also show that the gas in the DEC case is on average hotter than in the DIF case (i.e., even gas with temperatures below 10^4 K is less abundant). As mentioned above, this is a consequence of enhanced stellar feedback in the DEC run. At $|z| > 4$ kpc (top panels), the maximum gas density in the DEC case is lower compared to the DIF run. This is consistent with the gas surface density distributions shown in Figure 2.1. This could again be understood as being due to faster cosmic ray transport in the DEC case. This enhanced transport forces cosmic rays to interact with relatively less dense disk gas, which results in an outflow characterized by lower density.

Figure 2.3 shows the evolution of the vertical wind velocity (top row), cosmic ray number density (middle row), and magnetic field strength (bottom row) as a function of height above the midplane. All three variables are volume-weighted. The cosmic ray number density is computed from the simulation output cosmic ray energy density by $n_{\rm cr} = [(n-4)/(n-3)]e_{\rm cr}/E_{\rm min}$ where $n = 4.5$ is the slope of the cosmic ray distribution function in momentum, and $E_{\rm min} = 1$ GeV is the minimum cosmic ray energy.

From left to right, columns show results for the ADV, DIF, and DEC cases. The profiles are shown from the beginning of star formation at 50 Myr to quiescence at 200 Myr.

We begin the discussion of Figure 2.3 by considering the vertical gas velocity. In the ADV case, inflows (positive/negative "wind" velocity at negative/positive z) are present for most of the simulation time. Note that regions at large heights above the disk contain very little gas in this case. This has to be contrasted with the DIF and

DEC runs that are dominated by outflows. Interestingly, the wind in the DEC case is faster than in the DIF case (e.g., compare green-yellow curves near 140 Myr when the wind is about twice as fast in the DEC run) and lasts longer. Both of these effects are the result of stronger stellar feedback and the fact that it is easier to accelerate lower density gas in the DEC case.

Let us now consider the spatial distribution of cosmic rays and magnetic fields (shown in middle and bottom row, respectively). Cosmic rays are most tightly confined to the midplane in the ADV case. This is consistent with our analysis of the gas density projections (see left panel in Figure 2.1). On the other hand, in both DIF and DEC runs the cosmic rays are much more dispersed than in the ADV case; i.e., at large $|z|$ the cosmic ray number density is much greater for most of the simulated time. Moreover, the DEC run exhibits a much wider distribution of cosmic rays than that seen in the DIF case.

The trends seen in the evolution of the cosmic ray distribution are generally reflected in the evolution of the magnetic field profiles. Specifically, the magnetic field distribution is much broader in the simulations that include cosmic ray transport (DIF and DEC) compared to the ADV case. However, the magnetic field strength is much stronger in DEC than in DIF (except at very late times). In the DEC run, cosmic ray feedback is substantially more explosive than in the DIF run, launching a strongly magnetized outflow.

While we initialize a unidirectional 1 μG magnetic field, that initial field is quickly erased. In the inflow case (initial stage of the ADV case) the field is simply accreted onto the midplane. As we use diode boundary conditions (inflow through the top and bottom boundary is not permitted), accretion leads to the reduction of the magnetic field in the regions away from the midplane. Because no wind develops in this case, the gas density above and below the midplane is also very low as can be seen in the left panel in Figure 1. Thus, we expect the results in the ADV case to be unaffected by our assumption of spatially constant magnetic field, and an initial field decaying with the distance from the midplane should lead to very similar results. The bulk of the magnetic field amplification occurs only near the midplane as a result of turbulent motions associated with star formation and feedback. In the cases that include transport (DIF and DEC), the field is also amplified in the disk due to star formation and feedback, but following its amplification, it is expelled from the disk. During the outflow, the initial field is swept out of the simulation volume through the outer boundaries. We do not expect our assumption regarding the initial magnetic field to affect our conclusions in these cases either. Thus, the system quickly loses memory of the initial field configuration and strength. It is only in the cases that include cosmic ray transport that we expect significant magnetization of the gas at large distances from the disk at late times. This magnetization process occurs earlier in the DEC case compared to the DIF case, because the wind speed is larger in the former case.

The above differences between the evolution of the wind velocity, gas density, temperature, magnetic field strength, and cosmic ray number density will lead to different observational signatures. For example, we expect a stronger, spatially-extended soft X-ray emission when the decoupling mechanism operates. The presence of such emission may mitigate the problem reported by *Peters et al.* (2015), who found that cosmic ray driven outflows eject too little hot gas to match the soft X-ray background. Note that if streaming was additionally included, the coupled regions would be collisionlessly heated by cosmic rays, possibly producing even higher temperatures and stronger soft X-ray emission.

Furthermore, elevated cosmic ray number densities and magnetic field strengths in the halo, combined with shorter advection times than synchrotron cooling times, suggest more extended radio emission in the DEC case than in the DIF case. However, we note that our simulations reflect the cosmic ray proton rather than cosmic ray electron distribution; cosmic ray electrons are subject to energy-dependent losses (synchrotron and inverse Compton cooling) which dominate the nonthermal radio emission. We will investigate radio spectra in future work (e.g., via a Lagrangian tracer particle approach to follow synchrotron aging of electrons co-moving with the wind).

Finally, as the decoupling reduces the amount of time cosmic rays spend in the cold ISM phase, we expect that this mechanism would have implications for the γ-ray emission due to hadronic processes. We defer the study of these effects, and the other observational signatures, to a future publication.

In Figure 2.4, we quantify the properties of the mass flow and compare them to the star formation rates in the ADV (left column), DIF (middle column), and DEC cases (right column). Top row shows the evolution of the star formation rates (solid red lines) and the mass outflow rates computed by integrating mass fluxes through three different pairs of surfaces parallel to the disk. These planes are positioned at ±1 kpc (dashed green lines), ±2.5 kpc (dot-dashed blue lines), and ±5 kpc (dotted black lines). We find that there is essentially no outflow in the ADV case and the star formation in this case is very weak. This is consistent with the findings of a number of authors (e.g., *Salem and Bryan* 2014; *Girichidis et al.* 2016; *Simpson et al.* 2016; *Ruszkowski et al.* 2017). In this case, cosmic rays are confined to the dense disk and the pressure forces they exert are too weak to expel the dense gas from the galaxy. The enhanced pressure support in the disk inhibits the collapse of cold gas clumps and thus significantly suppresses star formation.

This picture is significantly altered when transport processes are included in the simulations. We find that in the DIF case, star formation is enhanced compared to the ADV case, and gas is displaced from the midplane. We observe a significant gas outflow followed by some inflow (the signature of a fountain flow). When the decoupling physics is included, the star formation rate is enhanced further and an outflow is launched, but there appears to be no inflow. Notice that not only is the star formation peak highest in this case, but the duration of the star formation episode is the longest. In DIF and DEC cases, there is a delay between the onset of star formation and the outflow.

The star formation rate increases from ADV to DIF to DEC due to decreasing cosmic ray pressure support in the cold ISM phase caused by faster cosmic ray escape from the disk. However, including energy-dependent losses of cosmic rays could decrease the cosmic ray pressure inside dense regions in the ADV case. In such a case, cosmic rays would additionally enhance the pressure in the ambient medium, boosting the star formation rate in this case relative to the DIF or DEC cases since the Bonnor-Ebert mass goes as $P_0^{-1/2}$ where P_0 is the ambient pressure (*Ebert* 1955; *Bonnor* 1956). Thus, it is possible that a treatment including energy-dependent losses of cosmic rays would find a boosted star formation rate in the ADV case relative to the DIF or DEC cases. We will investigate the effect of energy-dependent cosmic ray transport in future work.

In the bottom row we present the evolution of the integrated mass loading factor: the ratio of the integrated mass in the wind m_w to that in stars m_*. In the early stages of the disk evolution the gas cools and quickly settles very close to the disk midplane. Therefore, in measuring the wind mass, we delay the integration of the disk mass until 40 Myr. This allows us to exclude accretion through the set of planes positioned closest to the disk (±1 kpc) which would appear as a negative wind mass. Thus, this approach allows us to better quantify the true amount of gas expelled to large distances from the midplane over time.

In agreement with the findings presented in the first row, we observe that in the ADV case, the integrated mass loading factor is very low when the mass flux is measured at ±5 kpc from the disk. For smaller heights (±1 kpc) the integrated mass loading is higher and this simply reflects the fact that the disk puffs up due to the increased pressure caused by the inability of the cosmic rays to leave the disk.

As expected, in the cases that include cosmic ray transport, the integrated mass loading factors are much larger compared to the no-transport case. Surprisingly, the level of the integrated mass loading factors is roughly comparable in both the DIF and DEC cases despite the differences in the transport physics that lead to a number of important differences in the properties of the outflows and their observational signatures. This can be understood by the faster wind speed partially compensating for the much lower gas density in the wind for DEC compared to DIF. The DIF run exhibits integrated mass loadings of ∼0.3, which is comparable to that found in other papers (e.g., *Booth et al.* 2013), while the DEC run is somewhat smaller ∼0.2.

2.6 Summary and Conclusions

We perform simulations of cosmic ray feedback and its impact on the launching of galactic winds. In our simulations we find that cosmic ray transport is essential for driving galactic winds by cosmic rays – in the absence of transport effects, cosmic rays alone fail to drive winds, as found in previous studies (*Jubelgas et al.* 2008, *Uhlig et al.* 2012, *Simpson et al.* 2016).

However, a novel element of our simulations is that they incorporate the effect of the ISM temperature on cosmic ray propagation. At low temperatures, when the gas ionization fraction is low, ion-neutral friction can damp waves generated by the cosmic ray streaming instability and cosmic rays can propagate unimpeded through the ISM rather than scatter off these waves; i.e., cosmic rays are said to be decoupled from the ISM. Furthermore, low gas ionization leads to larger ion Alfvén speed and consequently faster cosmic ray transport. Both of these effects result in faster cosmic ray transport in the cold ISM. We model this transport phenomenon by introducing enhanced diffusion in low-temperature regions.

We note here that part of our motivation to treat decoupling via diffusion rather than streaming is to enable comparisons to previous work that also considered diffusion. Our work generalizes previously obtained results by investigating the impact of environment-dependent diffusion. It represents the first attempt to approximate the effects of the decoupling of cosmic rays from the low-temperature plasma on wind launching and the properties of the outflow.

Our simulations focus on a patch of a galactic disk to achieve higher resolution than would be otherwise possible. These simulations address a well-posed question of how the star formation rates and wind properties are affected by the decoupling of cosmic rays from the low ionization phase of the ISM. Our specific conclusions can be summarized as follows.

1. We observe the formation of low density and high temperature bubbles in the simulation that includes cosmic ray decoupling from the ISM. This raises the possibility that this case may result in enhanced soft X-ray emission from edge-on galaxies undergoing intense stellar feedback. We suggest that the formation of these structures is due to a combination of the increase in (i) the star formation rate and (ii) the effective cosmic ray transport speed. Our simulations show that faster transport leads to the expulsion of more tenuous gas from the galaxy because cosmic rays avoid cold and dense gas clouds in the disk and preferentially act on lower density ISM.

2. Our simulations corroborate earlier findings that cosmic ray feedback reduces star formation rates. We emphasize that this does not occur as a result of wind launching. In fact, the impact of cosmic rays on star formation is the strongest when transport processes are neglected and no wind is present. Our results are consistent with other studies in that they demonstrate a monotonic trend for the star formation to increase with the average cosmic ray transport speed. While star formation rate could be moderated by a number of model parameters, cosmic rays play a very important role in shaping the properties of

the outflows and controlling star formation rates.

3. Simulations with decoupling exhibit significantly elevated cosmic ray number densities in the halo at all times compared to the other cases. Combined with the fact the wind speed is generally faster in this case, and that the advection times are shorter while the synchrotron cooling times may be comparable to those observed in the case without decoupling, we speculate that the wider spatial distribution of cosmic rays may result in broader radio halos when the decoupling physics is taken into consideration.

4. Cosmic ray decoupling reduces pressure support near the galactic midplane due to faster cosmic ray escape from the cold ISM regions. This faster transport consequently leads to increased star formation rates and further injection of cosmic rays. This may have implications for hadronic losses and associated γ-ray emission.

5. Compared to the simulations without temperature-dependent cosmic ray transport, in the simulation including decoupling, the wind speeds are larger and the wind duration is longer.

6. The magnetic fields amplified near the midplane, that subsequently reach large distances away from the midplane, are much stronger in magnitude in the simulation including decoupling than in the case with diffusion. Additionally, since the winds are faster in the decoupling case, the dispersal of the magnetic fields occurs at earlier times in this case.

7. While the simulations with decoupling exhibit faster wind speeds compared to the case with diffusion, their winds are characterized by lower gas density. Consequently, wind mass loading factors – quantified in terms of the ratio of the integrated wind mass to the cumulative mass in newly formed stars – appear

to be roughly insensitive to the physics of cosmic ray transport.

8. Simulations with cosmic ray transport included reveal the presence of both fountain flows and net mass loss in the wind.

2.7 Exact cooling scheme test

To test our implementation of the *Townsend* (2009) exact integration radiative cooling scheme, we initialized gas of constant density and temperature in a cubical box with periodic boundary conditions. This setup ensured that, despite the fact the simulation included hydrodynamics, no gas flow developed and the only quantity with time dependence was the temperature that decreased due to radiative cooling.

To compare our implementation to an analytic solution, we simplified the problem and considered only one branch of the cooling function

$$\Lambda(T) = 3.2217 \times 10^{-27} T^{0.5} \mathrm{erg\,cm^3\,s^{-1}} \tag{2.15}$$

that corresponds to the uppermost temperature regime of the *Rosen and Bregman* (1995) cooling curve.[3] In this case, the thermal energy equation $de_g/dt = -n_H^2\Lambda(T)$, where e_g is the thermal energy density, and n_H is the hydrogen number density, has the following simple solution

$$T_f = \left[\sqrt{T_i} - \frac{3.2217 \times 10^{-27}}{3}\frac{n_H}{k_B}t\right]^2, \tag{2.16}$$

where T_f is the temperature after elapsed time t, T_i is the initial temperature, and k_B is the Boltzmann constant.

In the numerical test we set $T_i = 10^7$ K, $n_H = 1$ cm^{-3} and evolved the simulation for a few cooling times $t_{\mathrm{cool}} = e_g/[n_H^2\Lambda(T)]$. The agreement between the analytical

---

[3] The full cooling function implemented in the code, and used in the simulations presented in this paper, is given by Eq. (9).

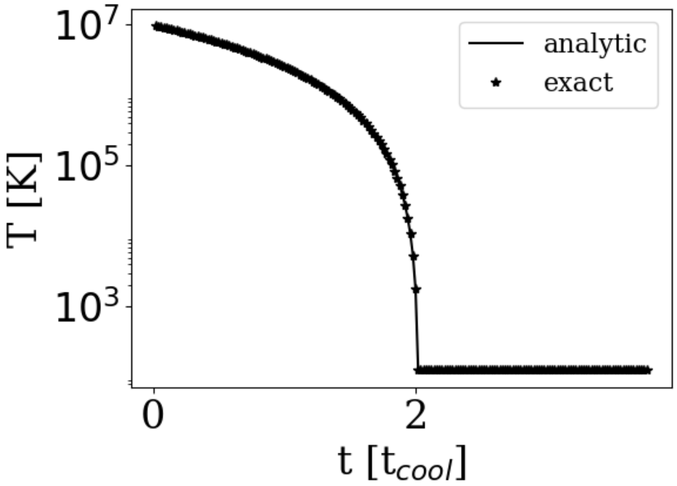

Figure 2.5: Evolution of the temperature obtained using the Townsend integration method (stars) compared to the analytic result (solid line).

result and the simulated solution obtained using the Townsend method implemented in the code was excellent (see Figure 2.5). The simulated temperature evolution agreed with the analytic result to machine precision. Importantly, the temperature did not overshoot the lowest temperature below which the cooling function was set to zero. Other methods may suffer from the overshooting problem in regions where cooling is fast and gas temperatures are low.

2.8 Test of temperature-dependent cosmic ray diffusion module

In order to validate the cosmic ray decoupling module that we implemented, we performed the following test. We set up a simulation with a temperature-dependent diffusion coefficient κ such that $\kappa(T) = T$ and $T(x) = 1 - x^2$. We used constant gas density and vanishing gas velocity throughout the computational domain (note that all quantities are in code units). Our spatial resolution was 64 zones in the x direction and temporal resolution was 10^{-5} time units. The initial cosmic ray energy density was initialized according to

$$e_{\rm cr}(t=0,x) = e_{\rm cr,0} + \frac{35x^4 - 30x^2 + 3}{8}, \tag{2.17}$$

where $e_{\rm cr,0}$ is an arbitrary constant background cosmic ray energy density and the last term in Eq. (B1) is the fourth order Legendre polynomial. These initial conditions are not isobaric. Since we were interested in testing the implementation of the diffusion module alone, we switched off hydrodynamics in this test, which allowed us to neglect pressure forces.

Using the above initial conditions, we solved the diffusion equation

$$\frac{\partial e_{\rm cr}}{\partial t} = \frac{\partial}{\partial x}\left[\kappa(x)\frac{\partial e_{\rm cr}}{\partial x}\right] \tag{2.18}$$

in a domain that was periodic in the x direction. The domain consisted of 64 zones and extended from $-\sqrt{3/7}$ to $\sqrt{3/7}$. These endpoints were chosen to ensure that the initial distribution of cosmic ray energy density had a vanishing slope at the boundaries of the periodic domain. This allowed us to eliminate jumps in energy density of cosmic rays at the boundaries. We then compared our solution to the analytic solution of Eq. (B2) given by

$$e_{\rm cr}(t,x) = e_{\rm cr,0} + \frac{35x^4 - 30x^2 + 3}{8}\exp(-20t). \tag{2.19}$$

Our simulated solution was in perfect agreement with the analytical solution (see Figure 2.6), validating the implementation of the decoupling module.

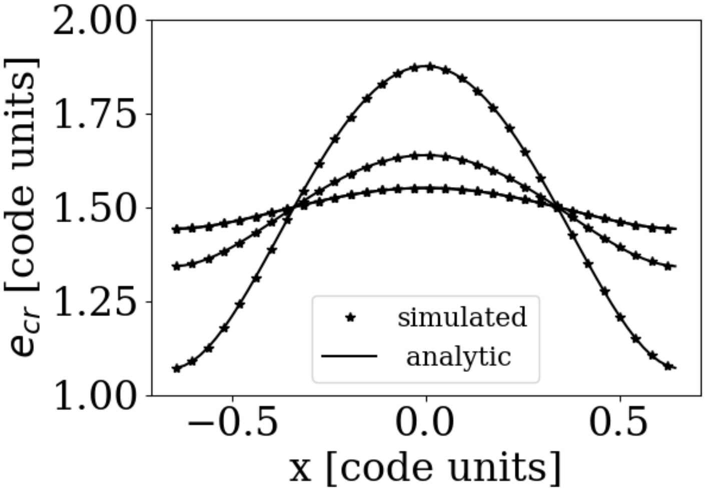

Figure 2.6: The evolution of the cosmic ray energy density due to temperature-dependent diffusion. Diffusion coefficient value close to the origin is largest. Curves correspond to 0.0, 0.05, and 0.1 code time units. Flatter curves correspond to later times. The agreement between the analytic (solid line) and code solution (stars) is excellent.

CHAPTER III

The Survival of Multiphase Dusty Clouds in Hot Winds

3.1 Preface

This chapter is adapted from the work of the same title, submitted to Monthly Notices of the Royal Astronomical Society. I am the lead author, and it is coauthored by Max Gronke. Therefore, some revisions may occur in response to the referee report. My contributions include implementation of the 'Cloud-tracking' scheme in FLASH, running the simulations, and analysis.

3.2 Abstract

Much progress has been made recently in the acceleration of $\sim 10^4\,$K clouds to explain absorption-line measurements of the circumgalactic medium and the atomic phase of galactic winds. However, the origin of the molecular phase in galactic winds has received relatively little theoretical attention. Studies of the survival of atomic clouds suggest efficient radiative cooling may enable the survival of expelled material from galactic disks. Alternatively, atomic and molecular gas may form within the outflow, if dust survives the acceleration process. We explore the survival of molecular, dusty clouds in a hot wind with three-dimensional hydrodynamic simulations in which we include radiative cooling and model dust as tracer particles. We find that molecular gas can be destroyed, survive, or transformed entirely to $\sim 10^4\,$K gas. We establish analytic criteria distinguishing these three outcomes which compare characteristic cooling times to the 'cloud crushing' time of the system. In contrast to typically studied atomic $\sim 10^4\,$K clouds, molecular clouds are entrained faster than the drag time as a result of efficient mixing. Moreover, we find that while dust can in principle survive embedded in the accelerated clouds, the survival fraction depends critically on the time dust spends in the hot phase and on the effective threshold temperature for destruction. We discuss our results in the context of polluting the circumgalactic medium with dust and metals, as well as understanding observations suggesting rapid acceleration of molecular galactic winds and ram pressure stripped tails of jellyfish galaxies.

3.3 Introduction

Since the historic discovery of massive outflowing filaments from M82 (*Lynds and Sandage*, 1963), galactic outflows have been observed ubiquitously (*Veilleux et al.*, 2005, 2020) both locally (*Lehnert and Heckman* 1996; *Martin* 2005; *Rupke et al.* 2005) and at high redshifts (e.g., *Shapley et al.*, 2003). Outflows are crucial in regulating the mass-metallicity relationship in galaxies (*Larson* 1974), polluting the circumgalactic medium (CGM) and intergalactic medium (IGM) with metals (*Mac Low and Ferrara* 1999; *Steidel et al.* 2010; *Booth et al.* 2012). Moreover, galactic outflows may help to address one of the most pressing puzzles in galaxy formation: the missing baryons problem (*Bell et al.* 2003).

While the amount of "baryons" (gas and stars) in galaxy clusters compared to their total mass is roughly consistent with the cosmological baryon fraction observed by *Planck* (*Collaboration et al.* 2020), a discrepancy arises at lower masses, as large as an order of magnitude for L_* galaxies and several orders of magnitude for dwarfs (*Dai* *et al.* 2010). This discrepancy may be explained by galactic outflows either ejecting material from the galaxy or preventing accretion of cosmological gas onto the galaxy. While active galactic nuclei likely dominate the outflow energetics of more massive galaxies than the Milky Way (*Croton et al.* 2006), outflows in lower mass galaxies are consistent with the energy budget of stellar winds and supernovae (*Somerville and Davé* 2015).

In the standard model of stellar feedback (*Chevalier and Clegg* 1985; CC85), supernovae shock-heat gas to $10^{6-7}\,$K, accelerating the gas to high velocities. X-ray observations of hot outflows find superb agreement between the mass outflow rate of hot gas with the CC85 model (*Strickland and Heckman* 2007), yet estimates of net mass loading are far lower than what is needed to regulate star formation (*Mac Low and Ferrara* 1999).

At the same time, millimeter and submillimeter observations detect rapidly outflowing molecular gas around nearby starbursts e.g., NGC 253 (*Bolatto et al.* 2013), the Galaxy (*Di Teodoro et al.* 2020; *Su et al.* 2021), and at high redshifts (z > 4, cf. *Spilker et al.* 2020). Bright CO features close to the launching radius suggest short dynamical timescales, strongly pointing to entrainment of galactic gas (*Walter et al.* 2017).

Classically, the acceleration of a cold cloud in a hot wind is known as the cloud crushing problem (*Cowie and McKee* 1977; *McKee and Cowie* 1977; *Balbus and McKee* 1982; *Stone and Norman* 1992; *Klein et al.* 1994; *Mac Low et al.* 1994; *Xu and Stone* 1995). Since the cloud destruction timescale due to hydrodynamic instabilities is shorter than the acceleration timescale of (hydrodynamic) ram pressure from the wind acting on the cloud (cf. *Klein et al.* 1994), subsequent work has focused on the ability of magnetic fields (*McCourt et al.* 2015; *Berlok and Pfrommer* 2019), conduction (*Armillotta et al.* 2016; *Brüggen and Scannapieco* 2016; *Cottle et al.* 2020) and the Mach cone from a supersonic flow (*Scannapieco and Brüggen* 2015) to prolong the cloud lifetime. However, clouds are nevertheless eventually destroyed by the hot medium.

Recent work (*Marinacci et al.* 2010; *Banda-Barragán et al.* 2016; *Armillotta et al.* 2017; *Gronke and Oh* 2018; *Sparre et al.* 2019; *Sparre et al.* 2020; *Gronke and Oh* 2020; *Li et al.* 2020; *Kanjilal et al.* 2021; *Abruzzo et al.* 2021) finds that efficient radiative cooling can enable a purely hydrodynamic acceleration of cold clouds (and similarly for cold streams, *Mandelker et al.* 2020) in the case of a transonic wind, as occurs at the launching radius of a galactic wind. Initially, mixing reduces the cold mass (which we explain in this work); however clouds that survive can grow an order of magnitude in mass while simultaneously acquiring the momentum of the hot wind.

Alternatively, the cold gas may form *in-situ* as the outflowing wind cools both adiabatically and with increased efficiency radiatively as the density of the wind is enhanced via incorporation of destroyed clouds (*Wang* 1994; *Thompson et al.* 2016). In this model, the cold phase is naturally expected to be co-moving with the hot phase (and growing in mass) for distances greater than the cooling radius[1], a few hundred parsecs above the disk. However, at least some systems exhibit properties apparently incompatible with bulk cooling (*Lochhaas et al.*, 2021). Moreover, in the case of M82 where detailed multiwavelength measurements abound: (i) cold outflowing gas is observed to diminish in mass flux with distance above the disk (consistent with cloud crushing), and (ii) dust is observed to be spatially coincident with outflowing HI and CO gas suggesting survival at least of dust from the galactic disk (*Leroy et al.* 2015).

While atomic gas can plausibly form in the thermal instability model, molecules cannot so simply re-form from the ashes of the mixed gas. Efficient formation of molecules requires cold dust grains that are dynamically ∼stationary with respect to

---

[1] The cooling radius marks the point at which the wind has adiabatically cooled sufficiently that the radiative cooling time becomes shorter than the dynamical time (cf. equation 6 in *Thompson et al.*, 2016)

atomic gas[2] (*Hollenbach and McKee* 1979). Thus, observations of outflowing dust and molecules may provide an interesting diagnostic to break the degeneracies among the various models purporting to explain the presence of high velocity cold gas embedded in hot winds.

Moreover, the transport of dust in galactic winds may explain observations of dust in the CGM. SDSS extinction maps reveal the ubiquity of dust in CGM for galaxies above $10^{10}\,M_\odot$ (*Zahid et al.*, 2013), from distances of 20 kpc to Mpc (*Ménard et al.*, 2010). The detection of dust at high redshift; i.e., by ALMA only 200 Myr after the Big Bang (redshift 8.4; *Laporte et al.* 2017) and by JMT in the Hubble Deep Field (redshift ∼4; *Hughes et al.* 1998), far before the evolution of low mass stars to the AGB phase, suggests supernova remnants act as major dust factories. Indeed, the galactic supernova remnant Cas A plausibly has produced of order $1\,M_\odot$ of dust (*De Looze et al.* 2017; *Bevan et al.* 2017; *Priestley et al.* 2019).

In this work, we extend earlier studies of ∼neutral (10^4 K) gas entrainment by exploring the evolution of ∼molecular (10^3 K) clouds; moreover we extend dust survival studies from high Mach cases appropriate for the interstellar medium to the transonic case relevant to the launching of galactic winds into the CGM. In §3.4, we describe the numerical methods employed. In §3.5, we present our results. In §3.6, we discuss the relation of our results to previous work and highlight where future progress may be made. We summarize and conclude in §3.7.

3.4 Methods

3.4.1 Numerical Setup

We performed our simulations with the Eulerian grid code FLASH 4.2.2 (*Fryxell et al.* 2000; *Dubey et al.* 2008) using the unsplit staggered mesh solver (*Lee and Deane*

---

[2] Since the kinetic energy of the grains must be less than the binding energy of atomic H on the grains.

Table 3.1: Simulation parameters.

Parameter Name	Parameter Value
RiemannSolver	HLLC
slopeLimiter	mc
order	2^a
charLimiting	False^b
use_hybridOrder	True
hybridorderkappa	0.5
cfl	0.2

a. MUSCL-Hancock,
b. Reconstruction in the primitive variables.

2009; *Lee* 2013) to solve the compressible, inviscid fluid equations, including radiative cooling as a sink term. We model dust as passive "tracer" particles to gain insight into the evolutionary history of clouds subjected to a hot wind (cf. §3.4.4 for details). To reduce computational expense, we implemented a "cloud-tracking" subroutine in FLASH (§3.4.3). See Table 3.1 for a list of the particular numerical settings used in our simulations.

To integrate optically thin radiative cooling into our simulations we utilize the *Townsend* (2009) exact integration scheme[3][4] (implemented in FLASH, cf. test in *Farber et al.* 2018), with a piecewise power law fit to the *Sutherland and Dopita* (1993) cooling curve down to 10^4 K, which we extend down to 300 K using the cooling curve of *Dalgarno and McCray* (1972). That is, we compute the cooling rate (shown in Figure 3.1) as

$$\Lambda(T) = c_k \left(\frac{T}{T_k}\right)^{\alpha_k} \tag{3.1}$$

where $\Lambda(T)$ is in the units of erg cm^3 s^{-1}, k indicates the temperature range, and $\alpha_k = \log\left(\frac{\Lambda_{k+1}}{\Lambda_k}\right) / \log\left(\frac{T_{k+1}}{T_k}\right)$; cf. Table 3.2 for the values of the coefficients, indices, and temperature ranges we employed. The above cooling curve assumes gas of solar

---

[3] The Townsend scheme is "exact" because the cooling equation $\frac{\partial e}{\partial t} = -n_H^2\Lambda$ can be integrated analytically if $\Lambda(T)$ is a power law (or other integrable dependence).

[4] Note that the Townsend scheme has no timestep restriction and avoids overcooling inaccuracies of implicit solvers.

Table 3.2: Piece-wise Power Law Fit to the Cooling Curve.

Temperature Range	Coefficient (erg cm^3 s^{-1})	Index
$300\,\mathrm{K} \leq \mathrm{T} < 2000\,\mathrm{K}$	10^{-26}	0.2
$2000\,\mathrm{K} \leq \mathrm{T} < 8000\,\mathrm{K}$	1.5×10^{-26}	0.5
$8000\,\mathrm{K} \leq \mathrm{T} < 10^4\,\mathrm{K}$	3×10^{-26}	19.6
$10^4\,\mathrm{K} \leq \mathrm{T} < 2 \times 10^4\,\mathrm{K}$	2.4×10^{-24}	6
$2 \times 10^4\,\mathrm{K} \leq \mathrm{T} < 2 \times 10^5\,\mathrm{K}$	1.5438×10^{-24}	0.6
$2 \times 10^5\,\mathrm{K} \leq \mathrm{T} < 1.5 \times 10^6\,\mathrm{K}$	6.6831×10^{-22}	-1.7
$1.5 \times 10^6\,\mathrm{K} \leq \mathrm{T} < 8 \times 10^6\,\mathrm{K}$	2.7735×10^{-23}	-0.5
$8 \times 10^6\,\mathrm{K} \leq \mathrm{T} < 5.8 \times 10^7\,\mathrm{K}$	1.1952×10^{-23}	0.22
$5.8 \times 10^7\,\mathrm{K} \leq \mathrm{T}$	1.8421×10^{-23}	0.4

metallicity. We enforce a temperature floor of $T_{\rm cl}$ and we turn off cooling above 0.6 $T_{\rm wind}$[5], $T_{\rm wind}$= χ $T_{\rm cl}$is the temperature of the hot wind.

3.4.2 Initial Conditions

We initialize a stationary, spherical cloud of radius $r_{\rm cl}$, temperature $T_{\rm cl}$, and density $n_{\rm cl}$ in a hot homogeneous wind with a density contrast χ flowing at a ~transonic Mach number, $\mathcal{M} = 1.5$. For the specific physical and numerical values used in our suite of simulations, see Table 3.3.[6] Unless otherwise noted, we shall discuss the $\chi = 10^3$, $T_{\rm cl} = 10^3\,\mathrm{K}$, $r_{\rm cl}/d_{\rm cell} = 16$, $r_{\rm cl} \in (0.01,\, 10,\, 100)\,\mathrm{pc}$ "fiducial" simulations (see Appendix 3.8 for convergence tests).

Our simulation domain consists of a cubical box with highest resolution for the interior ~10 $r_{\rm cl}$ perpendicular to the wind, and uniform refinement in the direction of the wind. We apply outflow (zero-gradient) boundary conditions except for the $-x$ boundary where an inflow (wind) boundary condition is applied.[7] After ±5 $r_{\rm cl}$ from the center of the cloud in directions perpendicular to the wind, we permit resolution

---

[5] Note that our temperature floor crudely approximates the effects of heating terms (e.g., cosmic rays, photoionization from the UV metagalactic background and young stars, and photoelectric heating).

[6] Note that we utilized $n_{\rm cl} = 0.1$ cm^{-3} in all runs. However, the only dynamically important quantities are, e.g., χ, $\mathcal{M}$, and $c_{\rm s} t_{\rm cool}/r_{\rm cl}$ (*Scannapieco and Brüggen*, 2015), so one can renormalize, for instance, the number densities accordingly.

[7] The inflow boundary condition is: $n_{\rm in} = n_{\rm w}, T_{\rm in} = T_{\rm w}, v_{\rm in} = v_{\rm w} = \mathcal{M} c_{s,w}$.

Table 3.3: Run parameters.

χ	$\mathrm{T_{cl}}$ (K)	r_{cl} (pc)	t_{cc} (Myr)	$t_{\mathrm{cool,max}}$ (Myr)	$t_{\mathrm{cool,minmix}}$ (Myr)	$t_{\mathrm{cool,mix}}$ (Myr)	$t_{\mathrm{cool,wind}}$ (Gyr)	$r_{\mathrm{cl}}/d_{\mathrm{cell}}$	L (r_{cl})	status
10^3	400	3	0.83	210	2.3	2.6	0.097	8	256	d[a]
10^3	400	30	8.3	210	2.3	2.6	0.097	8	256	w[b]
10^3	400	100	28	210	2.3	2.6	0.097	8	256	w
10^3	10^3	0.1	0.018	69	1.8	0.32	1.1	8	256	d
10^3	10^3	0.1	0.018	69	1.8	0.32	1.1	16	64	d
10^3	10^3	2	0.35	69	1.8	0.32	1.1	8	256	d
10^3	10^3	10	1.8	69	1.8	0.32	1.1	8	256	d
10^3	10^3	25	4.4	69	1.8	0.32	1.1	8	256	d
10^3	10^3	50	8.7	69	1.8	0.32	1.1	8	256	w
10^3	10^3	100	18	69	1.8	0.32	1.1	8	256	w
10^3	10^3	100	18	69	1.8	0.32	1.1	16	64	w
10^3	10^3	500	87	69	1.8	0.32	1.1	8	256	s[c]
10^3	10^3	1000	180	69	1.8	0.32	1.1	8	256	s
10^3	10^3	1000	180	69	1.8	0.32	1.1	16	64	s
10^3	10^4	3.8	0.21	1.1	2.5	1.6	51	8	256	d
10^3	10^4	380	21	1.1	2.5	1.6	51	8	256	s
10^3	4×10^4	320	8.7	47	47	69	150	8	256	d
10^3	4×10^4	32000	870	47	47	69	150	8	256	s

a. s for survived, b. w for warm survived, c. d for destroyed. Note that we used $\mathrm{n_{cl}} = 0.1\ \mathrm{cm^{-3}}$ in all simulations, whereas one may safely assume molecular clouds have higher densities (and hence (linearly)) smaller radii.

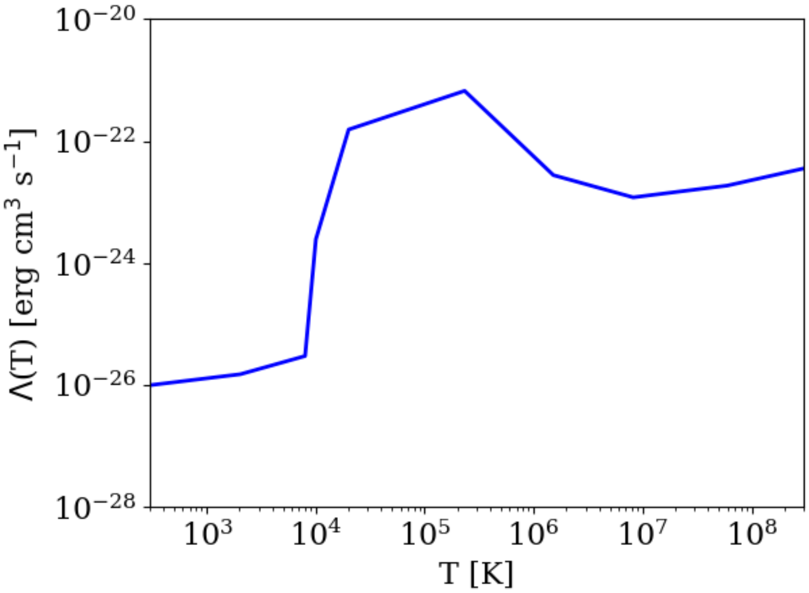

Figure 3.1: Cooling curve used in the presented simulations, utilizing a piecewise power law fit to *Sutherland and Dopita* (1993) above 10^4 K and *Dalgarno and McCray* (1972) below.

to degrade as quickly as possible (note we use 8 cells per block, the FLASH default). See Figure 3.2. Thus, we simulate a large domain perpendicular to the wind direction at minimal computational expense, capturing the proper geometry of the bow shock and minimizing influence of the boundary conditions on the numerical solution (cf. *Scannapieco and Brüggen* 2015; *Martizzi et al.* 2016).

We position the initial center of the cloud to be (7.5, 0, 0) r_{cl} from the center of the inflow boundary. Moreover, we guarantee the front of the bow shock remains in the simulation volume (and that cloud material does not interact with the inflow boundary) by applying a buffer region of extent 4 r_{cl} from the inflow boundary as part of the cloud tracking scheme.

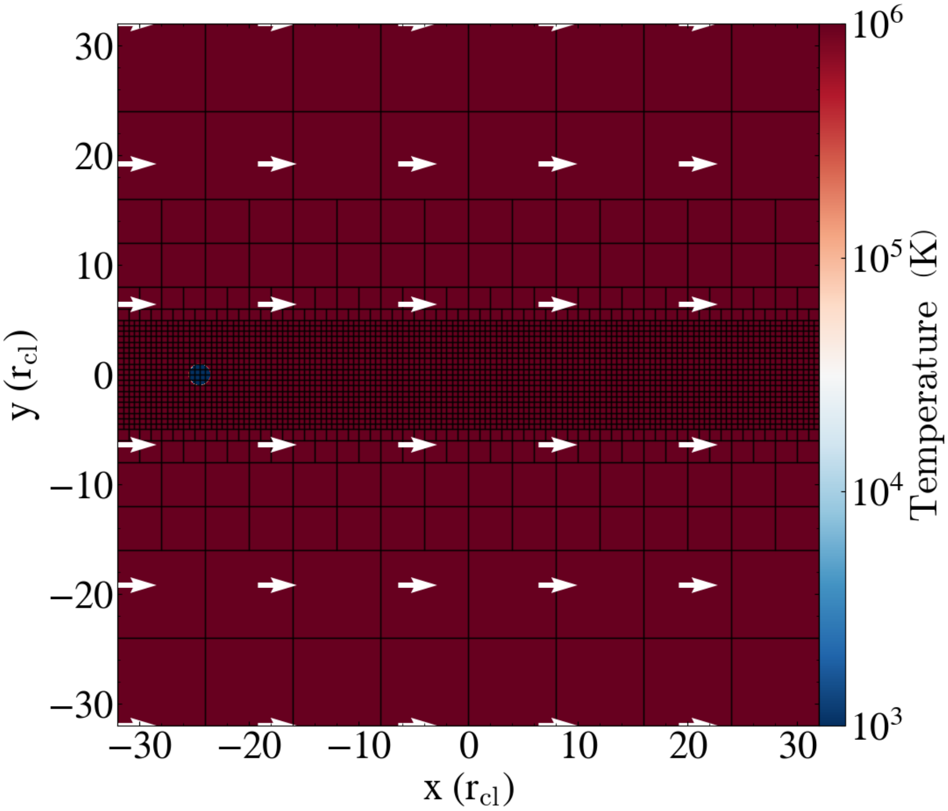

Figure 3.2: Initial conditions showing the grid for one of the fiducial simulations. The pale blue dot indicates our cloud. The white quivers indicate the velocity of the hot wind, which flows in from the -x boundary.

3.4.3 Cloud-Tracking

To reduce the amount of cloud material outflowing from the downstream face of our domain, we implemented a cloud tracking scheme in FLASH (*McCourt et al.* 2015; *Gronke and Oh* 2018). To do so, we follow the evolution of a Lagrangian tracer concentration (C; *Xu and Stone* 1995), which we initialize to $C = 1$ inside the cloud and zero elsewhere. This concentration variable is updated with the same numerical scheme as the other fluid variables, solving the conservation law

$$\frac{\partial \rho C}{\partial t} + \boldsymbol{\nabla} \cdot (\rho C \mathbf{u}) = 0 \tag{3.2}$$

which we use to compute the average cloud velocity

$$\langle u_{\rm cl} \rangle = \frac{\int_{x_{\rm min}}^{x_{\rm cl,0}} u_x C_{\rm cl} \rho \, \mathrm{d}V}{\int_{x_{\rm min}}^{x_{\rm cl,0}} C_{\rm cl} \rho \, \mathrm{d}V} \tag{3.3}$$

where x refers to the dimension in the direction of the initialized flow, $x_{\rm cl,0}$ is the x-coordinate of the initial center of the cloud, $x_{\rm min}$ is the x-coordinate of the minimum of the domain (bordering the inflow face), u_x is the velocity along the x dimension, $C_{\rm cl} = C > \max(C)/3$, and $\mathrm{d}V$ is the cell volume.[8]

Note that shifting to the cloud reference frame[9] (cf. *Dutta and Sharma* 2019) not only reduces box size constraints to track cloud material but additionally reduces advection errors (*Robertson et al.*, 2010).

In our cloud tracking scheme, we added a feature to guarantee no cloud material hits the inflow boundary: if any material with $C > 0.1$ is flowing upstream within a buffer region of size 4 $r_{\rm cl}$ from the inflow boundary, we switch to a reference frame twice the speed of the fastest detected upstream flowing gas. Reference shifting is then paused until all detectable material exits the buffer region (downstream). Subsequently, we resume reference switching to the cloud reference frame as described

---

[8] Note the maximum of C is taken every time step.

[9] subtracting $u_{\rm cl}$ from the inflow, grid, and particle velocities at every timestep.

Table 3.4: Notation.

Name	Property
`LRG`	100 pc
`MED`	10 pc
`SML`	0.01 pc
molecular	$\sim 10^3$ K
atomic	$\sim 10^4$ K
hot	$\sim 10^6$ K
$T_{\rm mix}$	$\left(T_{\rm cl}\, T_{\rm wind}\right)^{1/2}$
$t_{\rm cool,mix}$	$t_{\rm cool}\ \left(\mathrm{T} = T_{\rm mix}\right)$
$t_{\rm cool,max}$	$\max\left(t_{\rm cool}\ (\mathrm{T}\ \text{¡}\ T_{\rm mix})\right)$
$t_{\rm cool,minmix}$	$t_{\rm cool}\ \left(\mathrm{T}(\min(\mathrm{t_{cool}}))\ T_{\rm wind}\right)^{1/2}$

above.

3.4.4 Dust Model

We model dust as 10^6 velocity tracer particles (cf. *Genel et al.* 2013 for a discussion of velocity tracers compared to Lagrangian Monte Carlo tracers), which track the density and the temperature of the gas at each step, interpolated to the position of the particle. Initially, dust is randomly distributed within a cubical subvolume[10] of 0.75 $r_{\rm cl}$ (to ensure no particles are initialized outside the cloud due to discretization of the sphere) in an "alive" state. We set dust particles to a "dead" state if $\mathrm{T} \geq T_{\rm dest}$, which is a parameter we vary. In post-processing we determine the cumulative time each particle inhabits various bins of $T_{\rm dest}$to include the effect of dust surviving in hot gas for a finite 'sputtering' time[11].

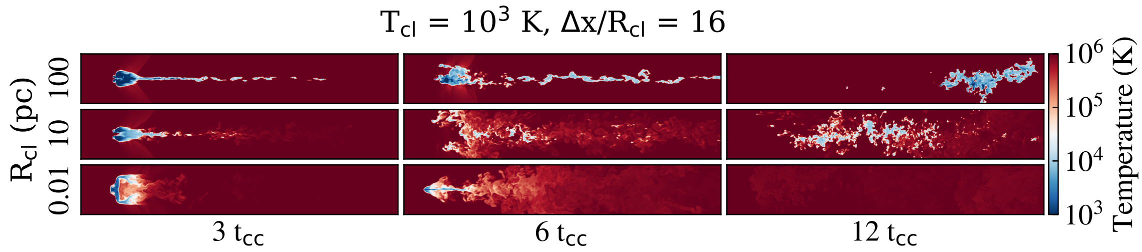

Figure 3.3: Temperature slices along the z-axis for three different cloud sizes (marked on the left). Left-right shows time evolution. Top (100 pc): survival of molecular gas, middle (10 pc): destruction of molecular gas yet survival of atomic gas, bottom (0.01 pc): destruction. Note the simulation domain is much larger than the region shown; however, we zoom in on the cloud material (the highest resolution region). See Figure 3.4 for a zoom-in on the cloud material of interest.

3.5 Results

3.5.1 Three Evolutionary Paths for Cold Clouds

We begin the discussion of our results with the potentially surprising discovery that three evolutionary paths exist for molecular ($T_{\rm cl}$ $\sim$$10^3$ K) clouds[12]. In Figure 3.3 we graphically illustrate the three characteristic evolutionary fates of molecular clouds: (i) survival of molecular gas, (ii) destruction of molecular gas yet survival of atomic gas, and (iii) complete destruction of molecular and atomic cloud material, via incorporation into the hot wind.

Specifically, we show temperature slices (red-blue indicate hot-cold gas) in Figure 3.3, including simulations with $T_{\rm cl} = 10^3$ K and $r_{\rm cl} = 100, 10, 0.01$ pc (from top to bottom; moving forward we refer to these clouds as `LRG`, `MED`, and `SML` as defined in Table 3.4). One can see that while the smallest cloud is being destroyed on a

---

[10] See Appendix 3.10 which shows the initial placement of the particles in this manner doesn't impact survival fraction more than ∼10%.

[11] Physically, the grains are eroded or 'sputtered' during collisions with the thermal gas. Thus large grains diminish in size until they return to the gas phase.

[12] Note that in this work we use 'molecular' as a temperature threshold. As we will discuss below, however, dust is crucial in order to (re-)form molecules, and thus, the coldest gas might in reality be free of molecules (e.g., *Krumholz*, 2012).

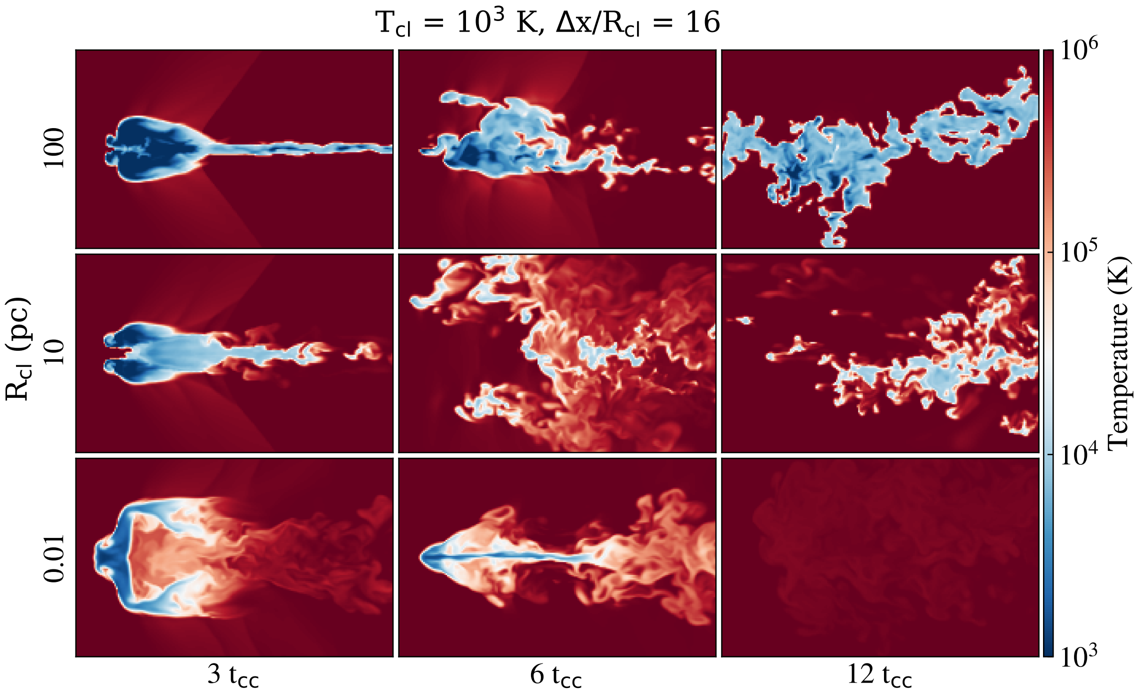

Figure 3.4: Same as Fig. 3.3 but zoomed in on cloud material.

timescale of $\sim 10\, t_{cc}$, the largest cloud clearly survives. The $r_{cl} = 10$ pc cloud is in an interesting intermediate regime: at $t \gtrsim 6 t_{cc}$ no molecular ($T \sim 10^3$ K) gas remains yet the atomic ($T \sim 10^4$ K) phase persists. In contrast, previous work focused on T_{cl} $\sim 10^4$ K clouds, finding the binary result of survival or destruction depending on if the cloud crushing time exceeded the cooling time of mixed gas. We have developed a new survival condition related to the three evolutionary paths (see §3.5.2), as well as a condition which sets when clouds transition from a destruction regime to a growth regime (for clouds that survive; see §3.5.3).

Taking a closer look via Figure 3.4 we see hints of these three fates early in the evolution. At 3 t_{cc} `LRG` has a more extended tail with molecular gas (dark blue). At the same time `MED` has a shorter, wider tail and more atomic gas at the head of the cloud (light blue). For `SML`, in which case cooling is very inefficient, most of the tail has already been incorporated into the hot phase and the interior contains a growing fraction of hot gas.

At 6 $t_{\rm cc}$ (central column in Figure 3.4) `LRG` is nearly entrained ($\Delta v \lesssim 0.1 v_{\rm wind}$) and its molecular gas is largely cocooned by atomic gas. At the same time, `MED` only has atomic gas remaining, which is vigorously mixing with the hot phase. `SML` is not entrained yet at 6 $t_{\rm cc}$ (recall that the acceleration time is $t_{\rm drag} \sim \chi^{1/2} t_{\rm cc} \sim 32\ t_{\rm cc}$ for these simulations); we will analyze the entrainment process further in §3.5.5.

At 12 $t_{\rm cc}$ the large cloud has collected its tail back into a semi-monolithic structure. The molecular gas is now growing in mass as the destructive mixing rate has decayed with the dissipation of turbulence to the point radiative cooling dominates (see §3.5.3 for the condition which sets the destruction vs. growth regime). `MED` has accumulated much atomic gas but it is still in the process of merging (and conversely being incorporated into the hot phase for the smaller cloudlets). `SML` has essentially been completely incorporated into the hot phase by this point.

The substantial growth of the atomic phase hinted by the cocooning phenomenon is seen more clearly in the temperature probability distribution functions for volume (left) and mass (right) of Figure 3.5. The blue, green, orange, and red curves respectively refer to the state at 3, 6, 12, and 24 $t_{\rm cc}$. After a few $t_{\rm cc}$, mixing fills out the intermediate temperature space between the cold and hot phases. While `SML` rapidly disintegrates into solely hot wind material, `MED` and `LRG` clearly demonstrate the growth of the 10^4 K (atomic) phase as a peak distinct from the 10^3 K (molecular) gas.

Let us next take a more granular consideration of the full evolutionary history of the three characteristic clouds, as presented in Figure 3.6. From top to bottom we show time series of the cloud mass, velocity difference between the cloud and wind ("shear"), and fraction of gas which originated in the cloud ("purity" fraction). That is, the purity fraction is the median value of the concentration C. We indicate `LRG` (100 pc) as blue curves, `MED` (10 pc) as green curves, and `SML` (0.01 pc) as red curves.

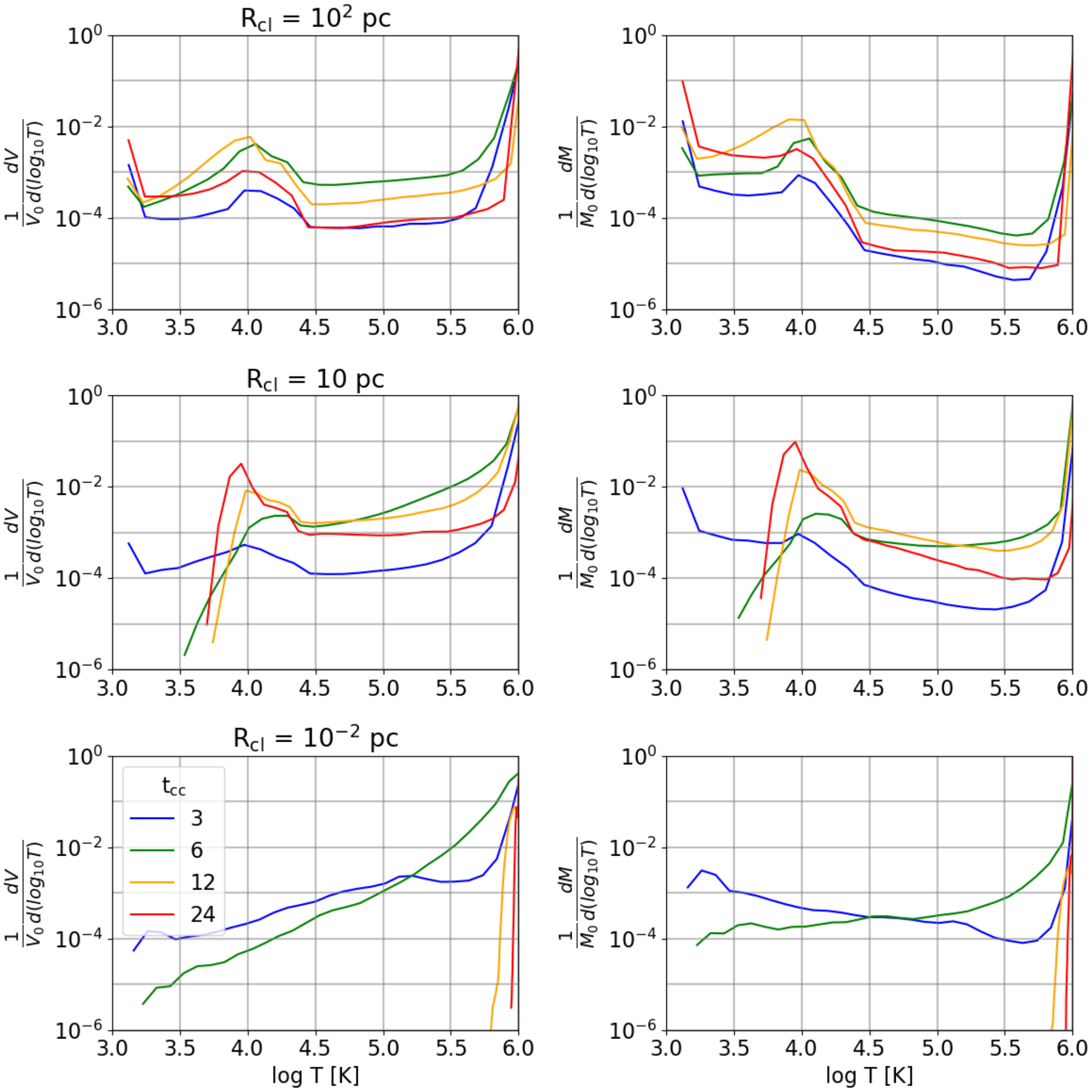

Figure 3.5: Temperature distributions (left: volume, right: mass weighted). Top-bottom: `LRG` (100 pc), `MED` (10 pc), and `SML` (0.01 pc) $T_{\rm cl} = 10^3$ K clouds. `MED` and `LRG` clearly maintain a substantial amount of gas at 10^4 K.

In all the panels of Figure 3.6, solid curves indicate the molecular phase (T ¡ 3 $T_{\rm cl}$), and dashed curves indicate the combination of atomic and molecular phases (T ¡ $T_{\rm mix}$).

The top panel of Figure 3.6 shows the mass evolution of the simulations shown in Figures 3.3 & 3.4 using two different temperature thresholds (note, we test convergence of the mass evolution in §3.8). We see that indeed `MED` loses its molecular gas rapidly compared to `LRG` (the rebirth of the molecular gas at $\sim$30 $t_{\rm cc}$ is explained in §3.5.3). However, after an initial period of loss, `MED` attains more atomic gas compared to `LRG` as a result of rapid mass growth of the atomic phase when the cloud is entrained, (cf. the Δv panel, second row of Figure 3.6). The corresponding drop in purity fraction indicates the clouds are rapidly entrained due to efficient transfer of momentum from the hot wind to the cloud as a result of mixing and cooling (as opposed to small shards of cloud material being efficiently accelerated by ram pressure; cf. *Gronke and Oh*, 2018; *Abruzzo et al.*, 2021; *Tonnesen and Bryan*, 2021).

$T_{\rm cl} = 10^3\,$K clouds clearly exhibit three evolutionary paths. However, what leads to this behavior which clearly differs compared to the well-studied $T_{\rm cl} = 10^4\,$K case? We argue the presence of a local maximum in the cooling time at $\sim 8 \times 10^3\,$K (as opposed to the $\sim$monotonic increase in cooling time with temperature above $\sim 10^4\,$K) is responsible for a semi-stable atomic phase.

3.5.2 Survival Criteria

3.5.2.1 Characteristic Cooling Timescales

In Figure 3.7 we show the isobaric cooling time as a function of temperature assuming pressure equilibrium by the blue curve. The green curves indicate the cloud crushing time of the clouds with the solid, dashed, and dotted curves indicating `LRG`, `MED`, and `SML` respectively.

The first timescale to consider is the cooling time of the mixed gas as considered

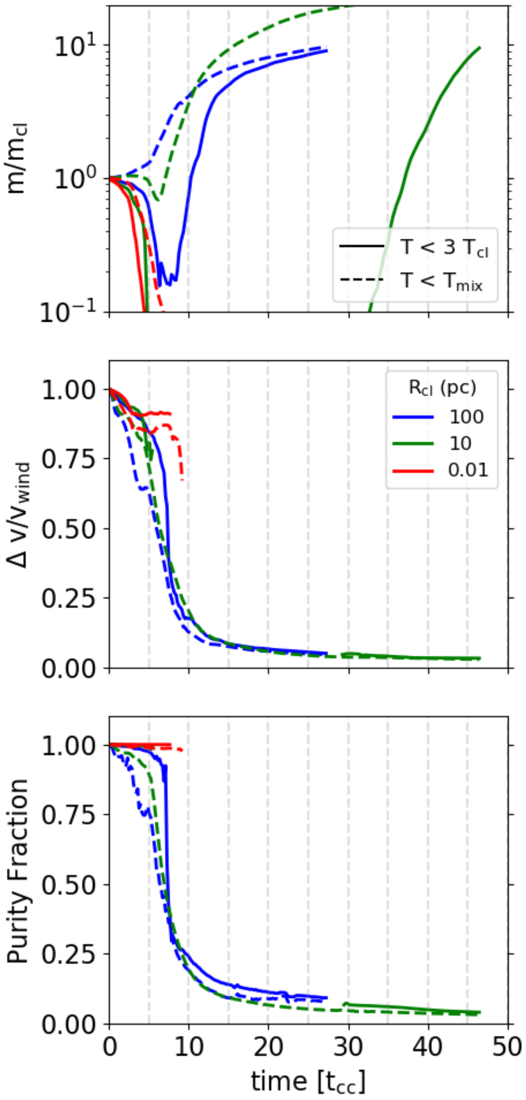

Figure 3.6: Time evolution from top-bottom of: cloud mass, velocity shear between the cloud and the wind, and the fraction of original cloud material (median value of the tracer concentration). Solid lines use a cloud temperature maximum of 3 T_{cl}(molecular gas), while dashed lines use a cutoff at T_{mix}(molecular and atomic gas). Blue, green, and red curves represent `LRG` (100 pc), `MED` (10 pc), and `SML` (0.01 pc) clouds respectively. Note we smooth data every 0.2 t_{cc} (full data contains outputs every 0.02 t_{cc}) to improve presentation clarity.

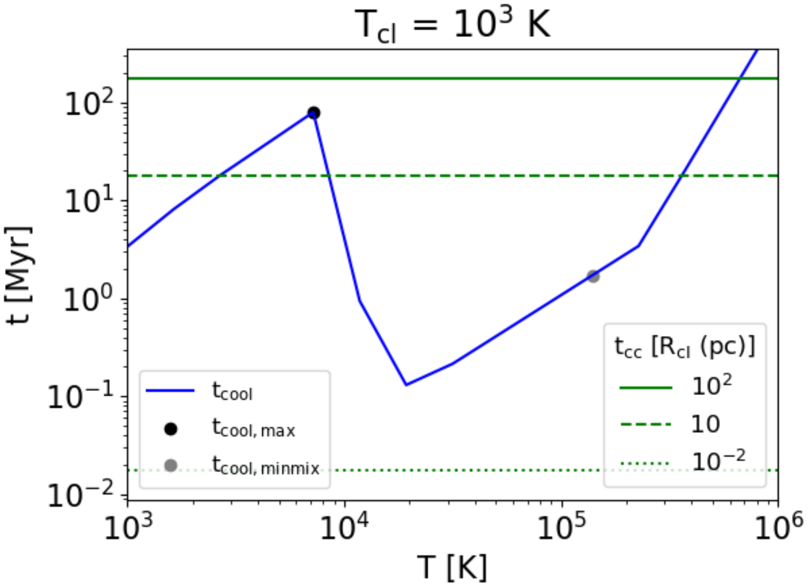

Figure 3.7: Comparison of the isobaric cooling time (blue, solid) to the cloud crushing times (green) of `LRG` (solid), `MED` (dashed), and `SML` (dotted). We have indicated important cooling times with respect to the cloud crushing time which dictate the evolutionary result of the cloud. The maximum cooling time, $t_{\mathrm{cool,max}}$, is indicated as a black point and must be shorter than the cloud crushing time for survival of molecular cloud material. The minimum cooling time of the mixed gas, $t_{\mathrm{cool,minmix}}$, is marked as a grey dot and must be shorter than the cloud crushing time for any cloud material to survive.

by *Gronke and Oh* (2018) as survival criterion for $\sim 10^4\,\mathrm{K}$ gas

$$t_{\rm cool,mix} \equiv t_{\rm cool}\big(T = T_{\rm mix}\big) \tag{3.4}$$

with $T_{\rm mix} = \sqrt{T_{\rm wind} T_{\rm cl}}$ as derived in a simple model of turbulent mixing layers by *Begelman and Fabian* (1990).

Second, we denote the longest cooling time of the gas between $T_{\rm mix}$ and $T_{\rm cl}$ as

$$t_{\rm cool,max} \equiv \max\big(t_{\rm cool}(T < T_{\rm mix})\big). \tag{3.5}$$

As such, $t_{\rm cool,max} = t_{\rm cool,mix}$ if the cooling time curve is monotonically decreasing, as is (roughly) the case for simulations truncating cooling at $10^4\,\mathrm{K}$.

And lastly, the cooling time of the gas with a temperature between the minimum cooling time and the hot gas:

$$t_{\rm cool,minmix} \equiv t_{\rm cool}\Big(\sqrt{T(\min(t_{\rm cool}))T_{\rm wind}}\Big). \tag{3.6}$$

Again, for a monotonic decreasing cooling curve, $t_{\rm cool,minmix} = t_{\rm cool,mix}$ so we recover the traditional, binary survival criterion above $10^4\,\mathrm{K}$. Note that in Eq. (3.6), we also used the geometric mean as an average temperature for the mixed gas – as was done for $t_{\rm cool,mix}$ above. While in practice the relevant cooling times of such mixed gas is some integrated quantity and, hence, dependent of the cooling curve between the two bordering temperatures (see a discussion of the impact of shape of the cooling curve on $t_{\rm cool,mix}$ in *Abruzzo et al.*, 2021), the geometric mean has proven to be a good approximation of it in the $\sim 10^4\,\mathrm{K}$ case (*Kanjilal et al.*, 2021). Note that $t_{\rm cool,minmix} = t_{\rm cool,mix}$ for $T_{\rm cl} \sim 10^4\,\mathrm{K}$ but the generalized form of Eq. 3.6 allows us to consider lower $T_{\rm cl}$, and as we will see below, establish criteria for the different outcomes presented in §3.5.1.

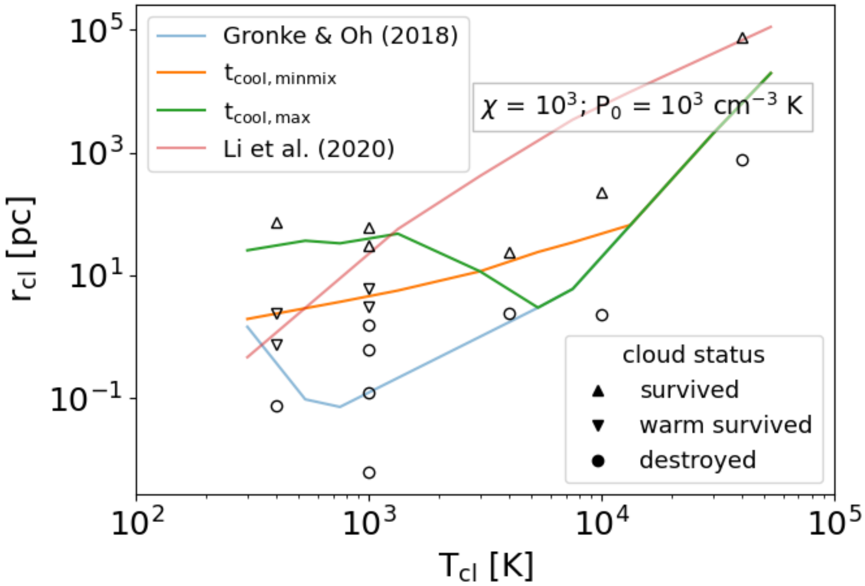

Figure 3.8: Comparison of simulation results. Destruction of all cloud material is indicated as circles. Destruction of the molecular phase and survival of the atomic phase is indicated by upside down triangles. Survival of the molecular phase is marked by triangles. The $t_{\rm cool,max}$ survival criterion (green) correctly predicts survival/destruction of molecular gas while the $t_{\rm cool,minmix}$ survival criterion (orange) predicts persistence of atomic gas vs. complete destruction. We show the $t_{\rm cool,mix}$ ($t_{\rm cool,wind}$) survival criterion of *Gronke and Oh* (2018) (*Li et al.* 2020) as blue (red) curves for comparison.

3.5.2.2 Evaluation of Survival Criteria

In the case of cooling down to 10^3 K, three possible evolutionary results emerge. In the case that $t_{\rm cc} > t_{\rm cool,max}$, molecular cloud material remains present throughout the simulation. When $t_{\rm cool,max} > t_{\rm cc} > t_{\rm cool,minmix}$, molecular cloud material is heated as it gets mixed. The atomic phase survives but is unable to cool efficiently down to the cloud temperature due to disruption via mixing (until the shear velocity driving such mixing sufficiently decays as the cloud is entrained, cf. §3.5.3). Note that when the cloud is entrained atomic cloud material will eventually cool down to the molecular phase (if dust survives, cf. §3.5.6), so this distinction is regarding the evolutionary path rather than the final end state. Last, in the case that $t_{\rm cc} < t_{\rm cool,minmix}$, all cloud material is incorporated into the hot wind, completely destroying the cloud (as in the classical adiabatic case). This picture is consistent with our three fiducial clouds as seen in Figure 3.4. In the next section, we perform a suite of simulations to test the new criteria more rigorously.

In Figure 3.8 we indicate the fate of the clouds we simulated as a function of $T_{\rm cl}$ and (initial) cloud radius ($r_{\rm cl}$). The three evolutionary paths are molecular phase survives (triangles), molecular phase is destroyed but atomic phase survives (upside down triangle), and complete destruction of cloud material (circles). Note that in comparison to Table 3.3, we have renormalized the presented $r_{\rm cl}$ to show results at fixed pressure $P_0/k_B = 10^3\,{\rm cm}^{-3}{\rm K}$. Recall all simulations presented are $\chi = 10^3$. We indicate the expected critical radii for molecular phase survival ($t_{\rm cool,max}$, green) atomic phase survival ($t_{\rm cool,minmix}$, orange), as well as the $t_{\rm cool,mix}$ criterion of *Gronke and Oh* (2018, 2020) and the $\sim t_{\rm cool,wind}$ criterion of *Li et al.* (2020) for reference.

At 4×10^4 K we recover the result of *Gronke and Oh* (2020): survival for clouds with efficient mixing ($t_{\rm cool,mix}/t_{\rm cc} \sim 0.1$) and destruction in the ∼adiabatic case $t_{\rm cool,mix}/t_{\rm cc} \sim 10$. We find disagreement with the $t_{\rm cool,wind}$ criterion of *Li et al.* (2020) in the case of our 10^4 K cloud; however, this is unsurprising given the differences in the physics we include (note that with conduction, *Li et al.* 2020 observe very little gas at intermediate temperatures since conduction removes temperature gradients; cf. §3.6.1.1 for a more detailed comparison with previous work).

Similarly, we observe disagreement with the $t_{\rm cool,mix}$ criterion of *Gronke and Oh* (2018, 2020) at 10^3 K. As the survival criteria are clearly separated at 10^3 K, we perform a higher sampling of cloud radii there to test the criteria. Allowing clouds a factor of two smaller/larger radii than the value indicated by the curve, we find agreement with $t_{\rm cool,max}$ and $t_{\rm cool,minmix}$. Interestingly, *Li et al.* (2020) is ∼consistent with $t_{\rm cool,max}$ at this temperature. We include a few representative cases at 400 K for reference. Note that the hot phase in this case, 4×10^5 K, should be short-lived and therefore the scenario is expected to be useful only for confirming the survival criteria theoretically as it is physically unlikely to be realized. Note the log-scaling so the smaller warm-survived case is only roughly a factor of two discrepant. We defer a study of the more realistic case of $T_{\rm cl} = 400\,{\rm K}$ with $\chi = 10^4$ for future work.

3.5.3 Condition for Mass Loss vs. Growth Phase

Consider anew the cooling time curve in Figure 3.7. If `LRG` has $t_{\rm cc} > t_{\rm cool,max}$, why does it take 10 $t_{\rm cc}$ before the $T_{\rm cl}$ gas starts growing? A similar mass evolution, i.e., a mass loss phase followed by a growth phase has been observed in similar 'cloud crushing' simulations before (e.g., *Gronke and Oh*, 2018; *Sparre et al.*, 2020; *Kanjilal et al.*, 2021; *Abruzzo et al.*, 2021) and in fact might be related to different 'survival criteria' (cf. §3.6.1.1). Here, we provide a simple argument on the transition point between the mass loss and growth phase by comparing (once again) the mixing to the cooling timescales (akin to what has been done in detailed studies focusing on the ISM context; *Hennebelle and Pérault*, 1999; *Saury et al.*, 2014).

Recall that since cooling becomes inefficient below $10^4\,{\rm K}$, gas piles up at $t_{\rm cool,max}$ forming a cocoon of atomic gas around the molecular gas (cf. Figure 3.4). Hence, the mixing time experienced by the $10^3\,{\rm K}$ gas is then given by $t_{\rm dest,mix} \sim (\chi')^{1/2} L/u' \sim (T(t_{\rm cool,max})/T_{\rm cl})^{1/2} r_{\rm cl}/u'$ where we have assumed that the outer scale stays approximately constant, and u' is the 3D turbulent velocity of the 'cocoon', i.e., the $\sim T(t_{\rm cool,max})$ gas. More specifically, we computed the velocity dispersion of gas with T $< T_{\rm mix}$.

Figure 3.9 shows the evolution of the ratio of $t_{\rm dest,mix}$ and the cooling time of the $\sim 10^4\,{\rm K}$ gas $t_{\rm cool,max}$ alongside the cold gas mass evolution (lower and upper panel, respectively). To evaluate $t_{\rm dest,mix}$ we computed u' as the 3D velocity dispersion of the $T < T_{\rm mix}$ gas. If this mixing time is initially shorter than the cooling time, the cloud loses cold gas; however, when the $t_{\rm dest,mix}$ becomes longer than cooling time the cloud enters the growth phase at $\sim$10 $t_{\rm cc}$ as observed for `LRG`. Similarly, `MED` does not re-generate molecular gas until $\sim$30 $t_{\rm cc}$ when the destructive mixing rate set by the turbulent velocity has dropped sufficiently low. Note that this means that for simulations where $t_{\rm dest,mix} > t_{\rm cool,max}$ there is no 'mass loss' phase and the cloud starts growing immediately. This is the case for some of our simulations: (i) $T_{\rm cl} = 400\,{\rm K}$, $\chi = 10^3$, $r_{\rm cl} = 120\,{\rm pc}$; (ii) $T_{\rm cl} = 400\,{\rm K}$, $\chi = 10^3$, $r_{\rm cl} = 40\,{\rm pc}$; (iii) $T_{\rm cl} = 10^3\,{\rm K}$, $\chi = 10^2$, $r_{\rm cl} = 30\,{\rm pc}$.

Figure 3.9 suggests a good agreement between the time at which our simulated clouds enter the growth phase with the $t_{\rm dest,mix}/t_{\rm cool,max} = 1$. This is somewhat surprising since we do only barely resolve the turbulence within the 'cocoon' and, thus, the mixing of the $\sim 10^3\,{\rm K}$ gas seeds. However, as we do resolve the outer scale ($\sim r_{\rm cl}$), and the mixing rate is set by the motion on this scale, the (re)appearance of molecular gas might be robust (cf. discussion in §3.6.4). More detailed, high resolution simulations targeting this process are necessary to study this further. For instance, an interesting avenue for future work is determining the evolution of the turbulent velocity (cf. *Ji et al.*, 2018; *Fielding et al.*, 2020; *Tan et al.*, 2021 for the plane-parallel case) *ab initio*, which would help determine the necessary simulation runtime to capture the mass growth phase.

3.5.4 Comparison between warm and cold clouds

In the following, we include simulations of warm clouds that survive $T_{\rm cl} \in (10^4\,{\rm K}, 4\times10^4\,{\rm K})$ to compare properties of our molecular clouds with previous work.

We now return to compare the time series for atomic and molecular clouds in Figure 3.10. In this case, the red, blue, green, and gold curves refers to the $T_{\rm cl} = 4\times10^4\,{\rm K}$, $10^4\,{\rm K}$, `LRG`, and `MED` clouds. From top-bottom we show the mass evolution, shear velocity, purity fraction, and the dust survival fraction (discussed in more detail below). Both of the $T_{\rm cl} = 10^3\,{\rm K}$ clouds evolve much more rapidly toward their

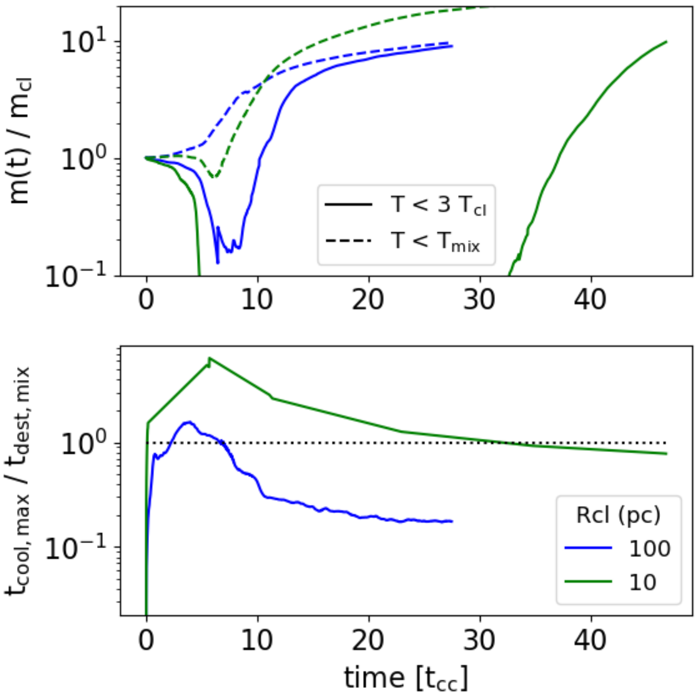

Figure 3.9: Top panel: cold gas mass evolution. Bottom panel: evolution of the mixing timescale $t_{\rm dest,mix} = (T(t_{\rm cool,max})/T_{\rm cl})^{1/2} r_{\rm cl}/u'$ where u' is the 3D velocity dispersion of the $\sim 10^4\,$K 'cocoon' (that is, T ¡ $T_{\rm mix}$) compared to $t_{\rm cool,max}$and $T(t_{\rm cool,max})/T_{\rm cl} = 8$ (cf. §3.5.3 for details). In both cases, clouds grow in molecular gas only after the mixing timescale becomes long compared to the maximum cooling time.

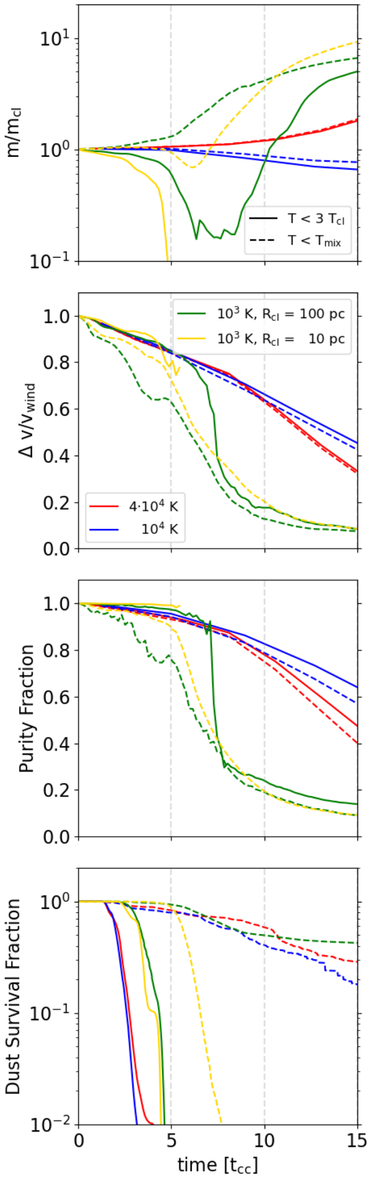

Figure 3.10: Time evolution from top-bottom of: cloud mass, velocity shear between the cloud and the wind, the fraction of original material below the cloud temperature, and the fraction of dust particles that stayed below the cloud temperature. Solid lines use a cloud temperature maximum of 3 $T_{\rm cl}$, while dashed lines use a cutoff at $T_{\rm mix}$. Red, blue, green, and gold respectively refer to $T_{\rm cl}$= 4×10^4, 10^4, 10^3, and 10^3 K clouds with green and gold corresponding to `LRG` and `MED` respectively. Note we smooth data every 0.2 $t_{\rm cc}$ (full data contains outputs every 0.02 $t_{\rm cc}$) to improve clarity of presentation. The $10^4$and 4×10^4 K clouds use $t_{\rm cool,mix}/t_{\rm cc}\sim 0.08$ as in (*Gronke and Oh*, 2018; *Abruzzo et al.*, 2021) and $t_{\rm cool,minmix}/t_{\rm cc}\sim$ 0.01 and 0.1 for the $R = 100$ pc and 10 pc cloud, respectively.

saturated state compared to atomic clouds included for reference, a point we turn to in the next subsection.

Recall that we model dust by initializing 10^6 velocity tracer particles inside the cloud. The bottom panel of Figure 3.10 indicates the fraction of particles that remain in cloud material (the "survival" fraction); we subsequently consider finite sputtering time in §3.5.6. Assuming a destruction temperature $T_{\rm dest} = 3\ T_{\rm cl}$ we find complete destruction of dust. However, permitting dust to survive up to $T_{\rm mix}$ we find roughly 10s% dust survives for `LRG`, while still no dust survives for `MED`.

Interestingly, the dust survival fraction is largest for `LRG`, likely due to the rapid growth of the atomic phase (despite the destruction of all original molecular gas, cf. §3.5.5) and lowest (excluding `MED` which is rapidly mixed away) for the intermediate temperature $T_{\rm cl} = 10^4\,{\rm K}$ cloud which takes longest to be entrained. We have shown only the first 15 $t_{\rm cc}$ of evolution to highlight the correlation of the evolution of the dust survival fraction with that of the shear velocity. Note, however, that the atomic clouds have essentially complete dust destruction as they take roughly 30 $t_{\rm cc}$ to be entrained and dust is continuously destroyed as cloud material gets mixed with the hot wind. However, once a cloud is entrained, the dust survival fraction saturates and `LRG` doesn't significantly change it's survival fraction (cf. Appendix 3.9). In any case, we show the dust survival fraction with the full simulation time for the cold clouds in §3.5.6.

3.5.5 The Sandman: Rapid Entrainment of Molecular Gas

As we saw in Figure 3.6, the surviving clouds are accelerated on a timescale of $\sim 10 t_{\rm cc} \ll t_{\rm drag} \sim 30\ t_{\rm cc}$. The nature of this rapid entrainment is elucidated in Figure 3.11, which shows the phase space of shear between the wind and cloud as a function of temperature of the gas. Yellow (purple) colors indicate large (small) masses in a bin indicative of cloud (wind) material. Black dots indicate the phase location

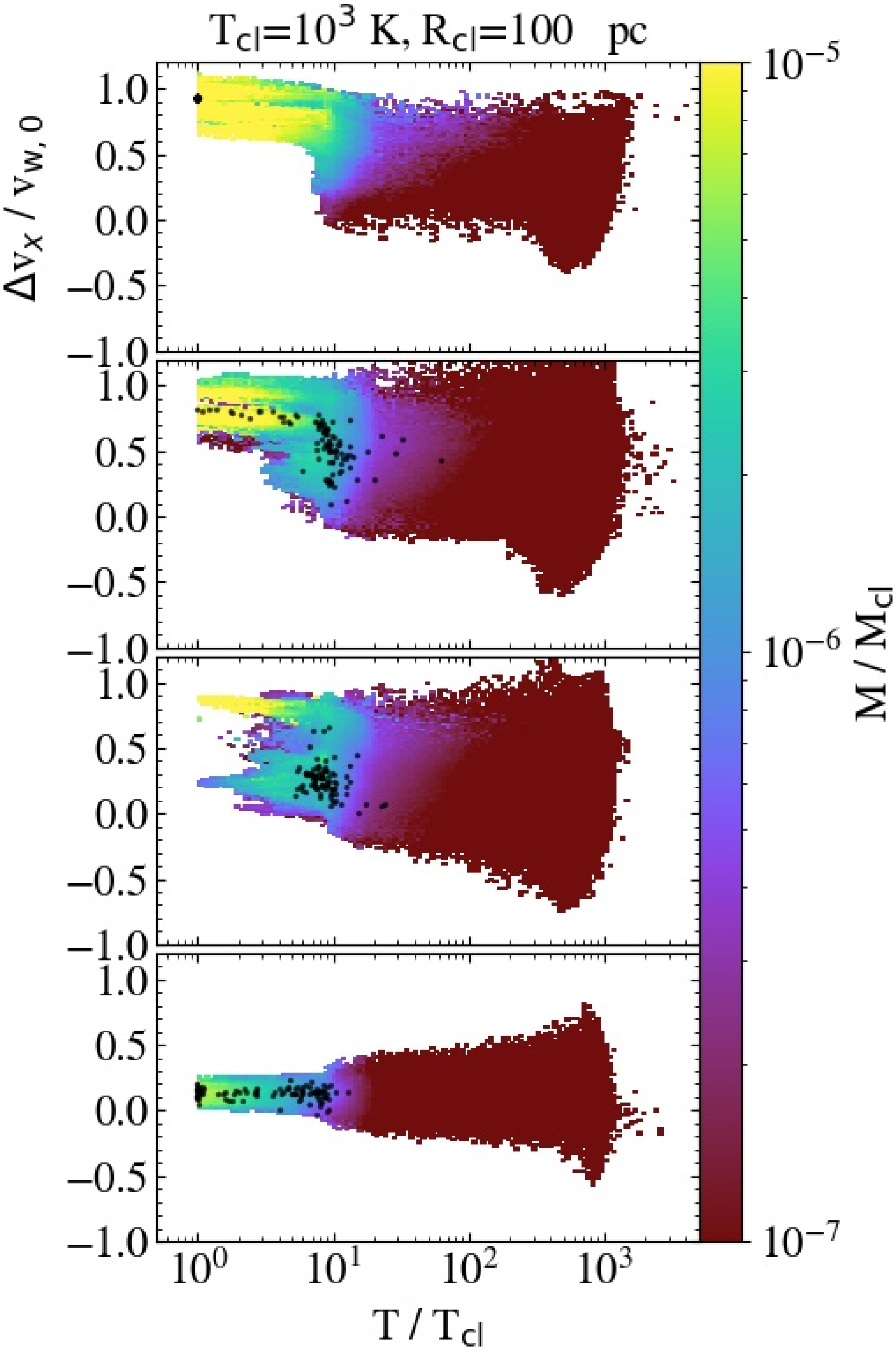

Figure 3.11: Phase plots of the velocity shear (in the wind direction) between the molecular and hot phases vs. temperature. From top to bottom we show the state at 3.2, 6.5, 8.2, and 12.9 t_{cc}, with times selected for clarity of the particle evolution. Tracer particles are overplotted as black dots and reveal entrainment proceeds via heating up cloud material during the mixing process and the mixed entrained cloud material cools back down to the molecular phase.

of tracer particles (note we only show one thousand for clarity), which indicate the original cloud material is heated into the atomic phase and entrained as it mixes with the hot wind. That is, the top panel at 3.2 $t_{\rm cc}$ shows the particles still inside the original cloud. The second panel from top at 6.5 $t_{\rm cc}$ shows particles evolving towards zero shear as they are mixed, exchanging momentum with the hot wind. The second panel from bottom at 8.2 $t_{\rm cc}$ shows most particles are now entrained in the mixed gas. The bottom panel at 12.9 $t_{\rm cc}$ shows that once the cloud material is entrained, it cools back down to the molecular phase.

That is, none of the original material remains in the molecular phase (in agreement with *Tonnesen and Bryan* 2021 at different scales, cf. their Figure 11); as original material is mixed, hot material that was mixed and entrained cools and replaces the original material. For `LRG`, this process occurs sufficiently rapidly that there is always molecular material, although after a relatively short period of time none of it belonged to the original cloud.

Although this suggests that instantaneous destruction of dust is efficient, modifying the sputtering time or destruction temperature can dramatically alter the survival fraction of dust, a point we turn to next.

Note that this process implies that for the rapid entrainment the ‘cocoon’ of warm gas is necessary (which is not the case for the $T_{\rm cl} \sim 10^4\,{\rm K}$ clouds, cf. Figure 3.6). It forms quickly because of the short cooling time of warm material, and is subsequently easier to accelerate due to a lower over overdensity. Mixing and continuous cooling to lower temperatures – as described above – ensures that the molecular gas is also successfully entrained.

3.5.6 Dust Survival

Since molecular H_2 requires re-formation on dust grains, the survival of dust plays a crucial role in the association of our coldest gas with a molecular phase. In this

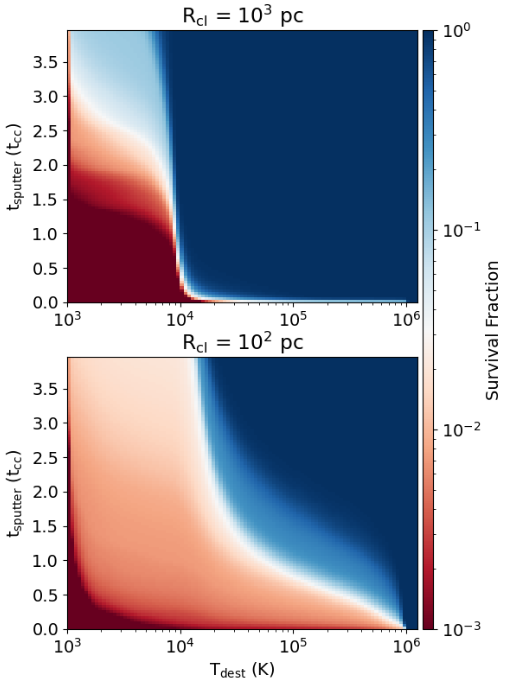

Figure 3.12: Dust survival fraction dependence on destruction temperature (x-axis) and sputtering time (y-axis), measured at the final output for each run (∼25 t_{cc} for `LRG` & 50 t_{cc} for `MED`). Blue (red) colors indicate near complete survival (destruction). Top (bottom) panel: `LRG` (`MED`). Note the very strong cutoff at $\sim 10^4$ K for short sputtering times in the top panel.

section, we consider dust destruction with a simple model that nevertheless brackets more involved modeling depending on the grain size distribution and grain species (see §3.6.4 for additional discussion).

Recall we define dust destruction conservatively such that dust is considered to be immediately destroyed when it encounters hot gas T $\geq T_{\rm dest}$. To bracket the range of possible dust survival, we present in Figure 3.12 the dust survival fraction's dependence on $T_{\rm dest}$ and sputtering time. Note that we measure the dust survival fraction using the full simulation time for each run ~ 25 (50) $t_{\rm cc}$ for `LRG` (`MED`). That is, one can relax our conservative definition of dust destruction by supposing dust can exist for some duration of time $\geq T_{\rm dest}$ before actually being destroyed (as in the case of thermal sputtering for example). We see that 10^4 K acts as a threshold for dust survival in the `LRG` case (particularly for the case of instantaneous destruction, with zero sputtering time) and most of the dust survives if it can survive up to $T_{\rm dest}$ $= 10^5$ K or several $t_{\rm cc}$ in the "hot" phase. In other words, large cloud dust survival depends primarily on $T_{\rm dest}$ and relatively insensitive to the sputtering time, whereas smaller clouds' dust survival depends more crucially on the sputtering time.

Moreover, this suggests dust that mixes out of the cloud remains predominately in the mixed phase, which more moderate temperature and higher density might provide more protection from FUV induced evaporation than if dust immediately inhabited the hot wind phase.

3.6 Discussion

We begin the discussion of our results by comparing to previous work, specifically cloud crushing simulations of $T_{\rm cl} = 10^4$ K clouds (§3.6.1.1) and studies of the survival of molecules & dust in cloud crushing setups (§ 3.6.1.2). Thereafter, we discuss the implications of our work regarding observations of galactic winds, fountain flows, observations of dust and cold gas in CGM (§3.6.2), and star formation in the jellyfish tails of ram pressure stripped galaxies (§3.6.3). We conclude this section by discussing potential caveats to our conclusions (§3.6.4).

3.6.1 Comparison to previous work

3.6.1.1 Cloud Crushing

Recent work on the cloud crushing problem has fixated on the survival criterion for $10^4\,$K clouds. While *Li et al.* (2020) & *Sparre et al.* (2020) find their simulated clouds survive based on the cooling time of the hot wind, *Abruzzo et al.* (2021) & *Kanjilal et al.* (2021) find general agreement with the $t_{\rm cool,mix}$ condition of *Gronke and Oh* (2018). We attribute our atomic clouds surviving with the $t_{\rm cool,mix}$ condition as related to evolving these clouds in a sufficiently large box for a sufficiently long duration to capture the growth regime of our atomic clouds.

Regarding our disagreement with *Sparre et al.* (2020) who perform very similar simulations to ours, a number of departures could explain our different results. As noted by *Kanjilal et al.* (2021), all simulations resulting in a $t_{\rm cool,mix}$ condition were performed with Eulerian grid codes whereas the $t_{\rm cool,wind}$ condition was found with Lagrangian-Eulerian codes. Eulerian codes produce extra mixing due to numerical diffusion. However, as *Gronke and Oh* (2020) found converged results for $\mathcal{M} \sim 1.5$ and numerical diffusion decreases with resolution, we expect our different discretization methods are not a significant concern.

Another difference that may affect the results of *Sparre et al.* (2020) is their use of periodic boundary conditions[13] and a relatively small numerical domain (64 $r_{\rm cl}$ in the flow direction and 16 $r_{\rm cl}$ transverse). However, we expect these numerical differences to play at most a minor role, as *Sparre et al.* (2020) state that their cloud material remains within their box during their simulated time.

---

[13] Note that the periodic boundary conditions transverse to the wind axis could mitigate the cooling flow onto the cloud and tail (cf. figure 3 for the impact of the orthogonal boundary conditions *Gronke and Oh*, 2018).

A possibly more significant difference between our works is related to the temperature floor: we require the minimum gas temperature to be $T_{\rm cl}$ in our simulations whereas *Sparre et al.* (2020) enforce $T_{\rm cl}/2$ (5000 K). If their clouds cool to $T_{\rm cl}/2$ rapidly this would significantly decrease the expected cloud survival radius (cf. Figure 3.8). Moreover, the lower cooling floor may effectively increase their "initial" overdensity by a factor of two, implying a somewhat longer drag time and hence a longer phase in the destruction regime. Similarly, we employ a tabulated power-law cooling function whereas they use a rather more sophisticated method, decomposing cooling into a primordial component (*Katz et al.*, 1996), Compton cooling off the cosmic microwave background (*Vogelsberger et al.*, 2013), and metal-line cooling using Cloudy models (*Ferland et al.*, 2013) with a metagalactic UV background (*Faucher-Giguere et al.*, 2009).

Yet the clearest and likely most significant departure of this work from *Sparre et al.* (2020) is the different definitions of cloud destruction we adopt; whereas we evolve our clouds for at least 25 $t_{\rm cc}$ independent of the cold mass content, *Sparre et al.* (2020) consider a cloud to be destroyed if its mass is not growing at 12.5 $t_{\rm cc}$, and it is clear some of these "destroyed" clouds would survive under our criterion (cf. their 47 pc cloud in Figure A2). That is, our simulations may produce the same results if interpreted uniformly.

As *Li et al.* (2020) include a number of additional physics we neglect, comparison is more difficult. Similar to *Sparre et al.* (2020), possibly the largest departure between our works is related to our different definitions of cloud destruction; *Li et al.* (2020) define a cloud as destroyed when less than 10% of the initial mass remains. Besides the different definitions of cloud destruction, the largest departure is likely their inclusion of conduction. In fact, they find that a cloud with ($T_{\rm wind}$, $r_{\rm cl}$, $n_{\rm wind}$, $v_{\rm wind}$) = (10^7 K, 10 pc, 10^{-2} cm^{-}3, 100 km/s) is destroyed with conduction included but survives when neglecting conduction. For concerns regarding resolution see Appendix 3.8.

3.6.1.2 Cloud Crushing: Dusty Molecular Clouds

Previous work that specifically studied the survival of dust in the cloud crushing problem has fixated on the supernova remnant context (Mach ~ 10, cf. *Silvia et al.*, 2010, 2012; *Kirchschlager et al.*, 2019; *Priestley et al.*, 2019, 2021; *Slavin et al.*, 2020). We focus our comparison on the most similar works to our own, that of *Silvia et al.* (2010, 2012), who performed ENZO (*Bryan et al.*, 2014) simulations treating dust as passive, velocity tracer particles perfectly coupled to the gas. They include radiative cooling but evolve their simulations only $\sim$10 $t_{\rm cc}$ since their cloud leaves the box in that time.

Silvia et al. (2010, 2012) model dust as 4096 tracer particles, with each particle representing a population of grains with a distribution of sizes. They include thermal sputtering in post-processing and find efficient destruction of grains smaller than 0.1 mm, suggesting efficient destruction when inertial sputtering is efficient. They find the amount of dust that survives varies widely depending on the composition (and to a more minor extent on metallicity at $Z > 100 Z_{\odot}$; *Silvia et al.* 2012); single element grains have $> 80\%$ survival while Al_2O_3 is completely destroyed and $MgSiO_3$ has 14% survival. The range of survival is in broad agreement with Figure 3.12 where we observe a range of complete dust destruction to complete dust survival depending upon the sputtering time and destruction temperature.

Our work on the survival of dust complements recent work by *Girichidis et al.* (2021), which studies the *in-situ* formation of molecular gas. *Girichidis et al.* (2021) perform simulations of initially atomic $\sim 10^4$ K clouds subjected to a hot 10^6 K wind with density contrasts 10^{2-3}, including H_2 formation catalyzed by dust grains. They assume a constant dust-gas ratio 0.01 (representative of the ISM), implicitly assuming perfect survival of dust and that dust remains coupled to their clouds. As we have shown, most dust may survive depending on the destruction model, motivating more detailed dust destruction modeling in future work. Their inclusion of effects we neglect, such as self-gravity of the gas, magnetic fields, a chemical network, and various heating terms limits our ability to compare our simulated clouds. In any case, they focus on the initial ($t \lesssim 10t_{\rm cc}$) evolutionary stages of molecular clouds, whereas we study the conditions for molecular cloud survival so again our work is complementary.

3.6.2 Implications for Molecular Galactic Winds and the Circumgalactic Medium

Since the pioneering work of *Spitzer* (1956), the question of the cold gas content of the CGM has persisted. Recent absorption-line measurements by HST/COS detect massive reservoirs of cool 10^4 K gas in the circumgalactic medium (*Werk et al.* 2013). The origins of such gas is difficult to ascertain as it may form via thermal instability (*Field* 1965; *Sharma et al.* 2012; *McCourt et al.* 2012; *Voit et al.* 2015; *Ji et al.* 2018; *Butsky et al.* 2020; *Falle et al.* 2020; *Kupilas et al.* 2021) or be entrained in galactic outflows. While observational constraints of the atomic phase are emerging, the molecular component remains difficult to study. Our finding that molecular gas is suggested to increase deep into the CGM (elaborated below) is intriguing, as such a growth may imply eventual star formation such as recently observed in galactic outflows (*Maiolino et al.* 2017; *Gallagher et al.* 2019). Such stars would possess highly radial orbits, developing the spheroidal component of galaxies and possibly evolving spiral into elliptical galaxies.

3.6.2.1 Clouds in the Galactic Center

Recent 21-cm emission surveys (*McClure-Griffiths et al.*, 2013; *Di Teodoro et al.*, 2018; *Lockman et al.*, 2020) have discovered a large sample of ∼200 neutral hydrogen clouds between ∼0.5-3.5 kpc from the Galactic midplane in the region commonly referred to as the Fermi bubbles (*Su et al.*, 2010). Interestingly, molecular gas is observed to be spatially coincident with at least some of these atomic clouds (*Di*

Teodoro et al., 2020; *Su et al.*, 2021) and similarly for the Small Magellanic Cloud (*McClure-Griffiths et al.*, 2018; *Di Teodoro et al.*, 2019). According to our model, all these clouds may have originally been molecular and either some clouds' molecular content is below the sensitivity limit of existing observations or these clouds were originally in the regime of `MED` placing them in the "warm survived" regime. That is, they only possess neutral gas now but if dust survives, the observed clouds will re-form molecular gas at large scale heights from the disk, deeper into the CGM.

Di Teodoro et al. (2018) observed most clouds to possess a characteristic size of $\sim$10s pc. Given their observed distance from the Galactic center, *Lockman et al.* (2020) estimate the required survival times of the clouds to be $\gtrsim$4-10 Myr. These timescales are rather perplexing in the classical cloud crushing picture because $t_{\rm cc} \sim 0.3\,{\rm Myr}$ (using $v_w = 300\,{\rm km\,s^{-1}}$, $\chi = 10^3$, $r_{\rm cl} = 10\,{\rm pc}$.) – but quite sensible given our results. `MED` is the typical size compared to observations and exhibits a survival time of $\gg 10\,{\rm Myr}$[14].

Our molecular clouds exhibit mass growth of the 10^4 K phase very rapidly, potentially explaining the larger mass in neutral clouds observed at higher latitude by *Di Teodoro et al.* (2018) compared to the low latitude clouds of *McClure-Griffiths et al.* (2013). Note the larger volume sampled and higher sensitivity in the measurements of *Di Teodoro et al.* (2018) partly account for the mass increase, yet they find no evidence for mass loss with increasing latitude. More extensive observations at uniform sensitivity to determine the mass-dependence on latitude (similar to the work by *Lockman et al.* 2020 on the velocity-dependence) may place helpful constraints on cold cloud acceleration models.

---

[14] Our wind speed was 180 km/s, about two times lower than the best fit for *Di Teodoro et al.* (2018). Observed clouds may be at higher overdensities or lower temperatures than simulated; therefore, caution should be used in comparing our results to that of *Di Teodoro et al.* (2018, cf. §3.6.4).

3.6.2.2 Extragalactic Multiphase Winds & CGM

Galactic winds are ubiquitously detected throughout the observable Universe, and we now understand their vital role in galaxy evolution (see reviews by *Rupke*, 2018; *Veilleux et al.*, 2005, 2020). While the driving mechanism of these winds predominantly accelerates hot gas (e.g., supernovae and AGN; *Chevalier and Clegg* 1985) a characteristic feature of these winds is fast moving, cold gas. Thus, we now know that galactic winds are multiphase, i.e., characterized by co-spatial hot ($\gtrsim 10^6\,\mathrm{K}$) and cold ($\lesssim 10^4\,\mathrm{K}$) gas – a picture that is also directly established by observations of nearby galaxies (e.g., *Heckman et al.*, 1995; *Martin*, 2005; *Strickland and Heckman*, 2009).

As eluded to in §3.3, how this much colder gas phase exists in such a hot, violent environment is an outstanding puzzle (see *Zhang et al.*, 2017, for a detailed discussion) to which essentially two classes of solutions have been put forward in the literature: (i) accelerating the cold gas, or (ii) creating the cold phase out of the hot medium. The major obstacle for the former class of models has to overcome is the 'entrainment problem'; that is, the fact that the acceleration time is shorter than the destruction time of the cold gas (in the case of ram-pressure acceleration by a factor of $\chi^{1/2}$, i.e., $\gtrsim 10$ for the temperatures quoted above). Thus far in the literature cooling (*Armillotta et al.*, 2016; *Gronke and Oh*, 2018), magnetic fields (*Dursi and Pfrommer*, 2008; *McCourt et al.*, 2015), or 'shielding effects' (*McCourt et al.*, 2018) have been suggested as potential solutions to this problem. For the second class of models in which the cold gas is forming from the hot medium, the cooling time of the (expanding) hot wind has to be shorter than other dynamical timescales (notably $\sim r/v_{\mathrm{wind}}$) which is the case for a certain part of the parameter space (*Wang*, 1994; *Thompson et al.*, 2016; *Bustard et al.*, 2016; *Scannapieco*, 2017; *Schneider et al.*, 2018; *Kempski and Quataert*, 2020; *Lochhaas et al.*, 2021).

The fast accelerating field of detections of an even colder, molecular gas phase embedded in galactic winds (e.g., *Fischer et al.*, 2010; *Cicone et al.*, 2014, 2018) as well as of dust in the winds of the CGM (*Ménard et al.*, 2010; *Peek et al.*, 2015) offer an opportunity to differentiate between the mechanisms at play; in order to (re-)form efficiently, dust is a crucial ingredient (*Draine*, 2011). However, as dust gets destroyed in the hot medium (a) through shocks on a $\lesssim 1000\,\mathrm{yr}$ timescale (*Dwek et al.*, 1996; *Ferrara and Scannapieco*, 2016); i.e., nearly instantaneously, and (b) through thermal sputtering on a timescale of $\sim 5.5(0.01\,\mathrm{cm}^{-3}/n)[(2\times10^6/T)^{2.5}+1]\,\mathrm{Myr}$ (*Tsai and Mathews*, 1995; *Gjergo et al.*, 2018). Combined, these effects make hot galactic winds a hostile environment for dust as was pointed out by *Ferrara and Scannapieco* (2016). These authors simulated dust destruction in a hot, outflowing wind parcel and found survival times of only $\sim 10^4$ years and conclude that the detection of molecules in quasar outflows is difficult to explain theoretically.

The results of this work show that (a) the direct acceleration of molecular ($\lesssim 1000\,\mathrm{K}$) gas by a hot wind is possible if $t_{\mathrm{cool,max}}/t_{\mathrm{cc}} < 1$ is fulfilled. This criterion corresponds to a gas cloud of size

$$r_{\mathrm{cl}} \gtrsim r_{\mathrm{cl,max}} \equiv 50\,\mathrm{pc}\frac{T_{\mathrm{cl,3}}^{1/2}\mathcal{M}_{1.5}}{P_3\Lambda_{-26}(T_{\mathrm{max}})} \tag{3.7}$$

where $T_{\mathrm{cl,3}} \equiv (T_{\mathrm{cl}}/10^3\,\mathrm{K})$, $\mathcal{M}_{1.5} \equiv (\mathcal{M}/1.5)$, and $\Lambda_{-26}(T_{\mathrm{max}}) \equiv (\Lambda/10^{-26}\mathrm{erg\,s^{-1}\,cm^3})$ is the cooling curve evaluated at $T_{\mathrm{max}} \sim 8000\,\mathrm{K}$. Note that this equation is only valid when T_{cl} ¡ 8000 K.

Furthermore, even for smaller clouds we show that (b) the 'atomic' $\sim 10^4\,\mathrm{K}$ gas can survive the ram pressure acceleration process if $t_{\mathrm{cool,minmix}}/t_{\mathrm{cc}} < 1$, corresponding to a geometrical criterion of

$$r_{\mathrm{cl}} \gtrsim r_{\mathrm{cl,minmix}} \equiv 7\,\mathrm{pc}\frac{T_{\mathrm{cl,3}}\chi_3\mathcal{M}_{1.5}}{P_3\Lambda_{-21.6}(T_{\mathrm{minmix}})} \tag{3.8}$$

where $\chi_3 \equiv (\chi/10^3)$ and $\Lambda_{-21.6}(T_{\mathrm{minmix}}) \equiv (\Lambda/10^{-21.6}\mathrm{erg\,s^{-1}\,cm^3})$ is the cooling curve evaluated at $T_{\mathrm{minmix}} \sim 2\times10^4\,\mathrm{K}$. Note the above equation is accurate within a factor of two for $200\,\mathrm{K} < T_{\mathrm{cl}} < 5000\,\mathrm{K}$. For $T_{\mathrm{cl}} < 200\,\mathrm{K}$, $\Lambda(T_{\mathrm{minmix}})$ jumps sharply four orders of magnitude and thus one must include the actual value of $\Lambda(T)$. Thus, because embedded in this gas the sputtering timescale of dust becomes very long (see above), it can survive, and allow the formation of molecules at larger distances.

These considerations suggest that detections of molecules and / or dust outflowing at distances $d \gtrsim \tau_{\mathrm{sputter}}/(4\,\mathrm{Myr}) v_{\mathrm{wind}}/(250\,\mathrm{km\,s^{-1}})\,\mathrm{kpc}$ or a $\sim$ constant molecular abundance as a function of radius can be interpreted as signs of successful cold gas acceleration. Thus far, only a few of such cases are studied (e.g., *Walter et al.*, 2017) but future observations will enlarge the sample size and allow for a detailed mapping of the destruction and / or entrainment process as a function of distance for a range of galaxies.

Such observations could in principle detect also the second signpost of cold gas acceleration permitted and facilitated by cooling discussed in §3.5.5, namely the very rapid acceleration due to an initial phase of mass loss followed by growth. Specifically, cold gas is detected moving 'unnaturally' fast – already at the hot gas velocity within distances of $d \lesssim v_{\mathrm{wind}} t_{\mathrm{drag}} \sim 50 \chi_3 r_{\mathrm{cl}}/(50\,\mathrm{pc})\,\mathrm{kpc}$ – which would give direct evidence for an efficient mass / momentum transfer from the hot to the cold medium via cooling.

3.6.3 Implications for Jellyfish Galaxies

Galaxies undergoing extreme ram pressure stripping host multiphase tails extending ~100 kpc (e.g., D100 in the Coma Cluster, *Jáchym et al.* 2017; cf. the GASP survey for additional examples, *Poggianti et al.* 2017b). Recent multiwavelength measurements have detected signatures of molecular gas, dust, and star formation in a growing sample (cf. *Moretti et al.* 2018) of "jellyfish" galaxy tails, named in relation to the appearance of their star-forming tails, extending roughly 100 kpc from their galactic disks (*Cortese et al.* 2007). Widespread star formation in ram-pressure stripped tails is enticing theoretically, as it could significantly contribute to the observed intracluster light.

However, the fact that molecular gas has been observed in these tails is theoretically puzzling since molecular gas is difficult to directly strip (*Tonnesen and Bryan* 2012). High-resolution CO measurements of three Virgo cluster galaxies by *Lee et al.* (2017) indicate spatial coincidence of molecular gas with the stripped HI, but no clear sign of molecular gas stripping. Additional evidence suggests most of the molecular gas observed in jellyfish tails likely formed *in-situ*: *Moretti et al.* (2018) observed four jellyfish galaxies with massive molecular tails (15-100% of the stellar mass in the disk). Each galaxy had a similar amount of molecular gas in the disk to normal galaxies, suggesting inefficient stripping of disk molecular gas. Moreover, the molecular tail gas mass was comparable to the mass in neutral hydrogen that was stripped.

Only in the most extreme cases of jellyfish galaxies is direct ram pressure stripping of molecular gas observed. ALMA observations of ESO137-001 close to the center (∼250 kpc) of the Norma cluster (*Jáchym et al.*, 2019) detect ∼kpc sized molecular cloud complexes, likely dynamically stripped while the spiral arm was unwound (ESO137-001's extant HI disk is only ∼1 kpc). Even in this case, the observations are surprising since the cloud crushing time of this molecular cloud complex is relatively short compared to the time from which it was expected to be stripped.

Our work elucidates these observations of molecular gas in jellyfish tails. We naturally expect ∼kpc molecular clouds to survive intact. Moreover, we have shown that dust can survive the acceleration process for $10^3\,$K clouds and hence stripped dusty, atomic gas can condense to form molecules. That dust survives ram pressure stripping is consistent with imaging from *HST* (*Elmegreen et al.*, 2000; *Cramer et al.*, 2019) and *Herschel* (*Cortese et al.*, 2010). Moreover, in our model the cold gas mass can naturally exceed the original stripped mass by accreting ICM material. This picture is validated by the detection in JO201 of a metallicity gradient from the disk towards the tail, suggesting disk material mixes with the ICM (*Bellhouse et al.*, 2019).

Further validation of our model explaining molecular gas in jellyfish tails is suggested by combining our results with the work of *Tonnesen and Bryan* (2021). The variety of cloud sizes and densities found to be stripped from galactic disks in *Tonnesen and Bryan* (2021) suggests some clouds will be similar to our `LRG` and `MED` fiducial cloud runs. Since we find that abundant dust can survive, molecules can form, leading to subsequent star formation as observed. However, more detailed comparisons will require simulations including density contrasts of $\chi = 10^{4-5}$, which we leave for future work. Similarly, including magnetic fields and self-gravity in future work may help constrain star formation in jellyfish tails (*Müller et al.*, 2021).

3.6.4 Caveats

We neglect a number of potentially important physical effects that may modify the results of this work, namely viscosity (*Li et al.*, 2020; *Jennings and Li*, 2020), conduction (*Brüggen and Scannapieco* 2016; *Armillotta et al.* 2017; *Li et al.* 2020), external turbulence (*Vijayan et al.*, 2018; *Banda-Barragán et al.*, 2018, 2019; *Tonnesen*, 2019; *Schneider et al.*, 2020), magnetic fields (*Grønnow et al.*, 2018; *Gronke and Oh*, 2020), and cosmic rays (*Wiener et al.*, 2017, 2019; *Brüggen and Scannapieco*, 2020; *Bustard and Zweibel*, 2021).

While conduction can play a role in the shape of the cold gas (*Brüggen and Scannapieco*, 2016), and certainly does affect observables (*Tan and Oh*, 2021), detailed simulations of turbulent radiative mixing layers have shown that the mass transfer between the phases is not affected by conduction in the 'strong cooling' regime (*Ji et al.*, 2018; *Fielding et al.*, 2020; *Tan et al.*, 2021). This is because turbulent diffusion dominates over thermal conduction, and the mass transfer rate is set by mixing on large scales and not by the microscopic (thermal or numerical) diffusion between the gas phases. This also implies that only the large scales (in our case $\sim r_{\rm cl}$) need to be resolved in order to obtain a converged mass growth rate (*Tan et al.*, 2021).

We expect non-thermal components like cosmic rays and magnetic fields to affect our results. Prior studies focusing on $T_{\rm cl} \sim 10^4\,{\rm K}$ have in particular found that magnetic fields can suppress mixing (e.g., *Ji et al.*, 2018, in a plane-parallel setup); thus, we expect the mass growth rates to potentially change. Interestingly, while ‘magnetic draping’ has been invoked to shield the cold gas, for larger overdensitites this effect becomes subdominant and for $\chi \gtrsim 100$, i.e., the ones considered in this study, it is not sufficient to make the gas survive until entrainment (*Gronke and Oh*, 2020; *Cottle et al.*, 2020). We therefore do not expect our survival criteria to change dramatically with the inclusion of magnetic fields.

Similarly with cosmic rays: while their non-thermal support would decrease the overdensities of our blobs (e.g., *Butsky et al.*, 2020), and thus allow, for instance, for faster entrainment, this would only affect χ and hence the timescales considered by at maximum a factor of a few.

We considered only an (initially) laminar wind impinging the cloud from one direction whereas in reality galactic winds have a non-radial component (*Vijayan et al.*, 2018; *Schneider et al.*, 2020). This turbulence will affect the cold gas (and the cooling flow, cf. *Dutta et al.* 2021) and a detailed study of this effect is an interesting avenue for future work. However, we note that the non-radial component is subdominant over the shock caused by the wind part and is, thus, arguably less responsible for the destruction of the cold gas (see, e.g., figure 21 in *Schneider et al.*, 2020, showing the non-radial component to be $\mathcal{M} \lesssim 0.1$). This is consistent with the findings of *Li et al.* (2020) who concluded that turbulence would not affect their results significantly.

In this work, we used the fixed effective cooling curve introduced in §3.4.1. In particular, we neglected metallicity, heating, and ionization effects which introduce additional dependencies on Λ. We note, however, that (a) the here derived criteria are general and can be adapted to a changed cooling curve, and (b) that our survival criteria imply column densities of $N \gtrsim r_{\rm cl,minmix} n \sim 10^{19}\,{\rm cm}^{-2}$ (since $r_{\rm cl,minmix} \propto 1/n$; *Gronke and Oh*, 2020), i.e., the surviving objects are self-shielded. A spatially varying cooling curve, e.g., due to mixing of different metallicity gas or ionization, might have interesting effects for the mixing process and is an interesting avenue for future work.

Since we study the early evolution of relatively diffuse molecular clouds, we neglect self-gravity. However, as the molecular clouds grow in mass they may exceed the Jeans mass, become self-gravitating, and form stars (cf. § 3.6.3). We plan to include self-gravity in future work to determine the propensity of molecular galactic outflows to become starforming (as recently observed, e.g., *Gallagher et al.* 2019) and to study the observed star formation in jellyfish tails (*Vulcani et al.*, 2018).

Perhaps of most concern to the conclusions of our work is the neglect of detailed dust modeling. We present our results in a general fashion, that is, as a function of destruction temperature and sputtering time (cf. §3.5.6) to allow for more more sophisticated dust models to be mapped onto them. We expect our chosen parameter range to bracket the more detailed dust models.

For instance, as *Kirchschlager et al.* (2019) show thermal sputtering alone destroys only 20% of dust in their model, whereas in combination with inertial sputtering nearly all dust is destroyed (cf. their figure 22). Therefore, our treatment of instant dust destruction when dust encounters the hot phase roughly approximates the effect of efficient inertial sputtering shifting the dust distribution to small sizes followed by efficient thermal sputtering in the hot phase (that is, $\rm t_{sputter} \rightarrow 0$). Allowing longer thermal sputtering times may be seen as decreasing the efficiency of inertial sputtering since in such a case larger grains will be present. Similarly, considering a range of destruction temperatures allows one to consider the survival of more volatile/robust grain species. We hope to explore these effect and perform detailed dust modeling in future work.

We furthermore hope to extend this work to higher Mach numbers as well as overdensitites, and more realistic wind geometries that we omitted in this work.

3.7 Conclusions

We perform simulations of molecular clouds subjected to a hot wind. In our simulations we find that generally dust and moleculas can survive ram pressure acceleration, if $t_{\mathrm{cool,max}}/t_{\mathrm{cc}} < 1$. However, we also show that the survival of dust depends on the time it can withstand a hot surrounding, as no gas stays cold the entire time but instead molecular gas mixes with the hot wind during the acceleration process and cools back to lower temperatures. Our simple model is consistent with previous work considering dust destruction in supernova remnant shocks (*Silvia et al.*, 2010; *Priestley et al.*, 2019; *Kirchschlager et al.*, 2019; *Slavin et al.*, 2020). Moreover, we find the $t_{\mathrm{cool,mix}}/t_{\mathrm{cc}} < 1$ condition of *Gronke and Oh* (2018) determines whether $\sim 10^4$ K clouds survive or are ablated by the hot wind, in agreement with recent studies (*Abruzzo et al.* 2021; *Kanjilal et al.* 2021).

A novel aspect of our work is the consideration of dust destruction in molecular clouds in a galactic wind context. We model dust as one million passive velocity tracer particles, assuming perfect coupling to the gas. In post-processing we determine the ability of dust to survive the acceleration process with a simple model, depending on the time (t_{sputter}) dust is in contact with hot gas (T $> T_{\mathrm{dest}}$). Our specific conclusions are as follows:

1. *Survival Criteria for Molecular Gas.* We discover a three-path solution for the evolution of molecular ($\sim 10^3$ K) clouds subjected to a hot (10^6 K) wind. Radiative cooling becomes inefficient below the temperature at which hydrogen becomes predominantly neutral, forming a local maximum in the cooling time curve $t_{\mathrm{cool,max}}$ $\sim$8000 K. By considering a variety of initial cloud sizes for $T_{\mathrm{cl}} =$

10^3 K clouds we find survival for cold gas requires $t_{\rm cool,max}/t_{\rm cc} < 1$, yet atomic (~$10^4$ K) gas can persist so long as cooling is more efficient than mixing between the atomic cloud phase and the hot wind; that is, $t_{\rm cool,minmix}/t_{\rm cc} < 1$. These two possible evolutionary paths merge and recover to the survival condition of *Gronke and Oh* (2018) for $T_{\rm cl} \geq 10^4$ K as the cooling time curve is monotonic for T $\geq 2{\times}10^4$ K.

2. *Growth vs. Mass Loss Condition for Surviving Clouds.* Even when molecular gas survives there is typically a period of mass loss before the molecular mass eventually grows (up to 10 times the initial mass). We determined $t_{\rm cool,max}/t_{\rm dest,mix} < 1$ is the condition for mass growth. That is, efficient gas cooling below the peak of the cooling time curve $t_{\rm cool,max}$ must exceed the instantaneous mixing rate, set by the eddy turnover time $t_{\rm dest,mix}$(which can initially be much smaller than the cloud crushing time, but grows long as the turbulent velocity drops as the cloud becomes entrained). This result might explain similar growth profiles observed previously in the literature (e.g., *Sparre et al.*, 2020; *Kanjilal et al.*, 2021; *Abruzzo et al.*, 2021).

3. *Fast Entrainment of Molecular Gas.* We find molecular clouds are entrained much more rapidly than atomic clouds at the same initial overdensity $\chi = 10^3$ and similar cooling efficiency; this is faster than the acceleration time $t_{\rm drag}$ theoretically expected from our initial conditions. Our simulated molecular clouds are rapidly cocooned by a warm 10^4 K phase which efficiently exchanges momentum with the hot gas, allowing for the molecular phase to be accelerated ~3 times faster than direct mixing between the molecular and hot phases. This helps to explain observations of molecular gas rapidly outflowing from galaxies close to the expected launching radius (cf. *Veilleux et al.*, 2020).

4. *Survival of Dust.* In simulations of molecular clouds that survive the acceler-

> ation in a hot wind, we find that the survival of dust is possible but depends sensitively on the destruction temperature and cloud size. For $T_{\mathrm{dest}} \geq 10^4\,\mathrm{K}$, unless dust can inhabit atomic-hot gas for > 30 Myr in the case of large clouds we find $> 90\%$ of dust will be destroyed. Destruction temperatures slightly above $10^4\,\mathrm{K}$ allow nearly all dust to survive in ∼100 pc clouds, whereas ∼10 pc clouds require dust to persist in hot gas at least a few Myr. The rather sharp transition between the vast majority of dust surviving versus destroyed may allow observations of dust in galactic winds and ram pressure stripped tails to constrain models of dust destruction.

While these results help to understand molecular gas dynamics – and the survival of dust – in galactic winds, many open questions remain such as the inclusion of more relevant physics, the expansion of the considered parameter space, and boundary conditions closer to reality. We plan to pursue these in future work.

3.8 Resolution Convergence

We performed simulations with the same setup as `LRG` at two times coarser and two times higher resolution (8 and 32 cells per cloud radius) to test convergence. We find larger initial destruction of molecular gas and a longer period before growth of the low resolution run (8 cells per cloud radius), whereas the fiducial (16 cells per cloud radius) and high resolution (32 cells per cloud radius) evolve remarkably similarly. Note that both low and high resolution simulations were performed with the same box dimensions as the fiducial run (see Table 3.3).

3.9 Dust Survival Fraction Convergence

To investigate the convergence of the dust survival fraction, we perform simulations at $\chi = 10^2$ since the dynamical time is shorter and hence the simulations arrive

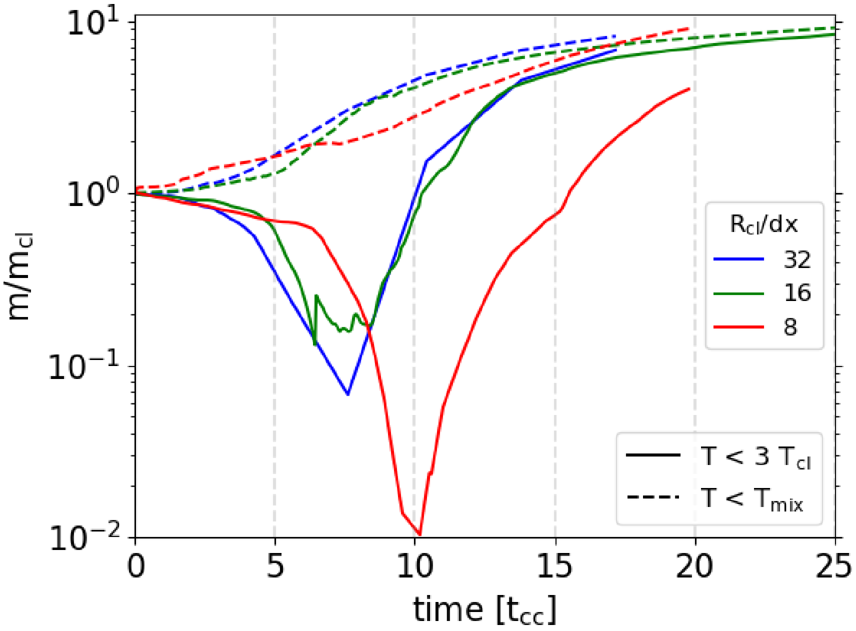

Figure 3.13: Mass growth converges with increasing resolution. We are showing here the $T_{\rm cl} = 10^3\,$K, $r_{\rm cl} = 100\,$pc (`LRG`) run. The red, green, and blue curves refer to 8, 16, and 32 cells per cloud radius resolution respectively. Solid (dashed) curves indicate the mass in the molecular)atomic and molecular) phase(s).

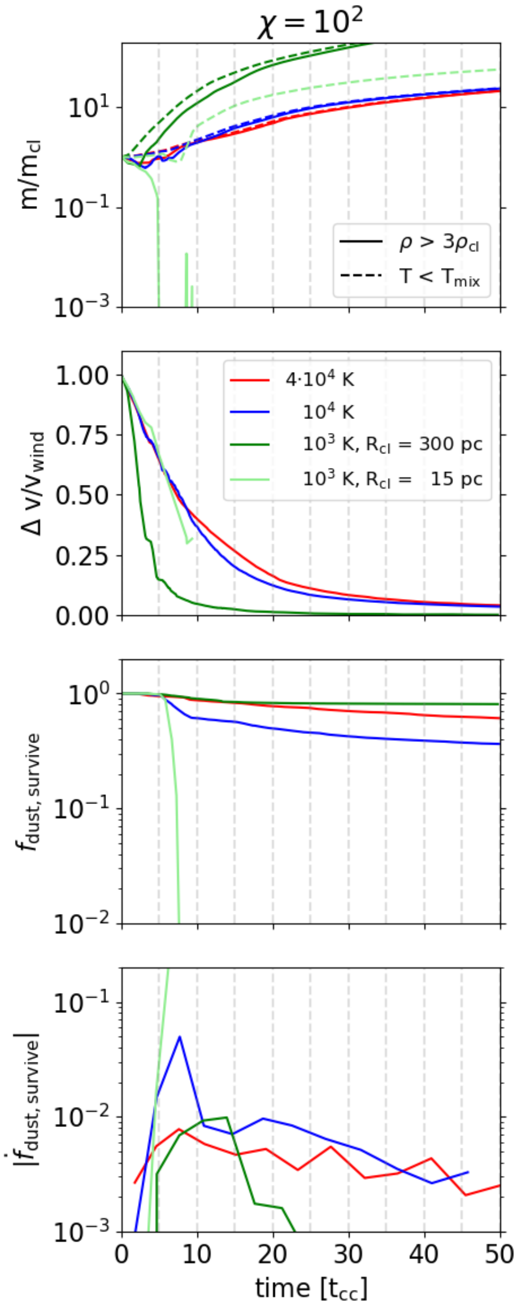

Figure 3.14: Dust survival fraction converges as shear velocity asymptotes to zero. The bottom row shows the logarithmic slope of the dust survival fraction, demonstrating convergence (with simulation time) of the destruction rate.

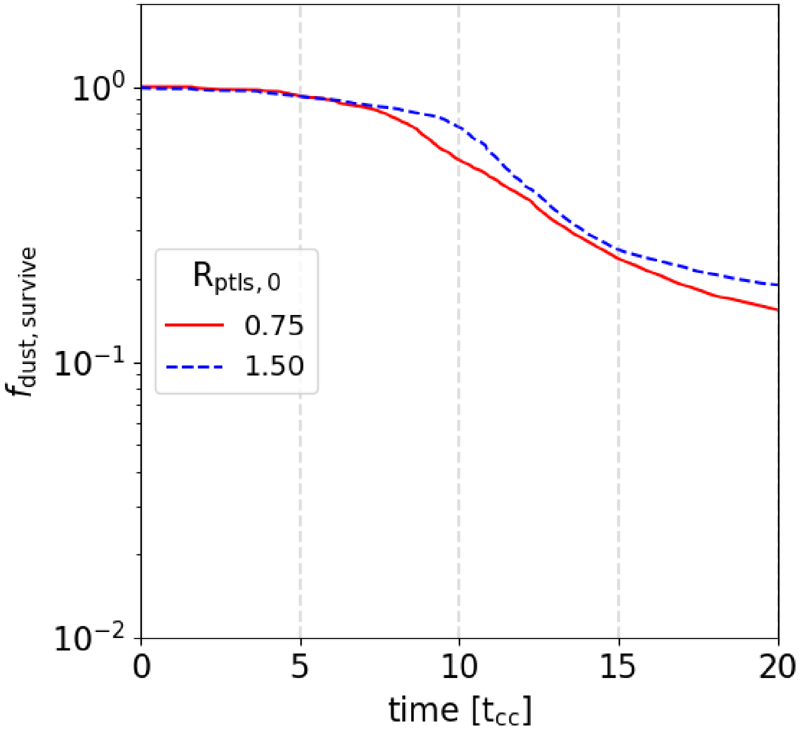

Figure 3.15: Dust survival fraction does not strongly depend on initial placement of dust.

at a saturated state more readily than at higher overdensities. In Figure 3.14 we see that the dust survival fraction (third row) has ∼saturated as the shear velocity approaches zero, as evidenced by the time derivative of the survival fraction (fourth row) dropping below 10^{-2}. Also note that the mass growth has similarly saturated; dust survival and mass growth are anticorrelated at late times since they both involve mixing of cloud and wind material.

3.10 Dust Initial Conditions

To determine the impact of our placement of dust within a subvolume of the initial cloud, we performed one simulation in which dust was initialized randomly uniformly within 1.5 r_{cl} from cloud center. We neglected dust initially placed outside the cloud from the dust survival fraction analysis, reducing the number of dust particles involved in the analysis to $\sim$300,000. From Figure 3.15 one can see the initial placement of dust only has a $\sim$10% impact on the survival fraction.

CHAPTER IV

Stress-Testing Cosmic Ray Physics: The Impact of Cosmic Rays on the Surviving Disk of Ram Pressure Stripped Galaxies

4.1 Preface

This chapter is adapted from the work of the same title, submitted to Monthly Notices of the Royal Astronomical Society. I am the lead author, and it is coauthored by Mateusz Ruszkowski, Stephanie Tonnesen, and Paco Holguin. Therefore, some revisions may occur in response to the referee report. My contributions include running and analyzing the models. Mateusz Ruszkowski, Stephanie Tonnesen, and Paco Holguin contributed valuable analysis and modeling advice that helped shape this project. Paco Holguin contributed code to model cosmic-ray cooling from Coulomb collisions and hadronic interactions. Note that I contributed code for a subgrid momentum stellar feedback module to "Cosmic-Ray-driven Outflows from the Large Magellanic Cloud: Contributions to the LMC Filament" by Chad Bustard, Ellen G. Zweibel, Elena D'Onghia, J. S. Gallagher III and Ryan Farber, published in The Astrophysical Journal 2020, vol. 893, p. 29.

4.2 Abstract

Cluster spiral galaxies suffer catastrophic losses of the cool, neutral gas component of their interstellar medium due to ram pressure stripping, contributing to the observed quenching of star formation in the disk compared to galaxies in lower density environments. However, the short term effects of ram pressure on the star formation rate and AGN activity of galaxies undergoing stripping remain unclear. Numerical studies have recently demonstrated cosmic rays can dramatically influence galaxy evolution for isolated galaxies, yet their influence on ram pressure stripping remains poorly constrained. We perform the first cosmic-ray magneto-hydrodynamic simulations of an L_* galaxy undergoing ram pressure stripping, including radiative cooling, self-gravity of the gas, star formation, and stellar feedback. Although the gas removal rate is relatively insensitive to cosmic ray physics, we find that cosmic rays significantly modify the phase distribution of the remaining gas disk. In addition, we find that galaxies undergoing ram pressure stripping exhibit enhanced gas accretion onto their centers, which may explain the prevalence of AGN in these objects and may help to constrain cosmic ray calorimetry or transport processes. Moreover, the microscopic transport of cosmic rays plays a key role in modulating the star formation enhancement experienced by spirals at the outskirts of clusters compared to isolated spirals. In agreement with observations, we find cosmic rays significantly boost the global radio emission of cluster spirals. These results suggest observations of galaxies undergoing ram pressure stripping may place novel constraints on cosmic-ray calorimetry and transport.

4.3 Introduction

Galaxies exhibit strikingly different properties depending upon the local density of their environment (*Dressler*, 1980). Spirals inhabiting high density environments such as clusters ("cluster spirals") tend to be redder, more anemic in neutral hydrogen gas, have lower star formation rates, and stronger magnetic fields than their more isolated counterparts in the field (*Hubble and Humason*, 1931; *Butcher and Oemler Jr*, 1978; *Boselli and Gavazzi*, 2006).

Multiband observations of relatively isolated star-forming spirals orbiting in cluster environments ubiquitously detect copious amounts of multiphase gas pointing away from cluster center in 'tail' structures extending up to 100 kpc (e.g., in X-rays, *Sun et al.* 2006, 2009; in Hα, *Zhang et al.* 2013; in 21-cm emission *Oosterloo and van Gorkom* 2005; in CO, *Jáchym et al.* 2017; *Moretti et al.* 2018; and see the GASP survey for more examples *Poggianti et al.* 2017b).

The relative motion between the intracluster medium (ICM) and the galaxy's interstellar medium (ISM) can lead to gas removal from the disk if the ram pressure (RP) $P_{\rm ram} = \rho v^2$ exceeds the gravitational restoring force per unit area $P_{\rm grav}$ (*Gunn and Gott III*, 1972; *Roediger*, 2009). This ram pressure 'stripping' (RPS) should lead to eventual quenching of star formation with most of the gas expected to be stripped on the first infall (*Jaffé et al.*, 2015).

However, observations of cluster spirals undergoing RPS can detect moderate *enhancements* of star formation (*Vulcani et al.*, 2018). This star formation enhancement may be related to observations of high efficiency neutral to molecular gas conversion in RPS galaxies (*Moretti et al.*, 2020a,b), suggesting compression-induced star formation. Moreover, recent observations by the GASP survey suggest the AGN fraction is strongly enhanced relative to the field (*Poggianti et al.*, 2017a; *Radovich et al.*, 2019).

Some hydrodynamical simulations have studied the effect of RP on the surviving gas disk. *Schulz and Struck* (2001) coined the term "disk annealing", or the compression of the inner surviving disk via angular momentum transport. *Tonnesen and Bryan* (2009) found that at low RP strengths, more gas was compressed than removed by the ICM, and *Tonnesen* (2019) argued that early compression could have a long-lasting impact on the amount of gas that is stripped.

Additional simulations have focused on the impact of RP on the star formation rate (SFR) of galaxies, although no consensus has been reached. While many simulations predict that in some cases RP can cause a modest increase in the disk SFR (*Kronberger et al.*, 2008; *Steinhauser et al.*, 2016; *Ruggiero and Lima Neto*, 2017; *Lee et al.*, 2020), some find that the global SFR is suppressed (*Tonnesen and Bryan*, 2012; *Roediger et al.*, 2014; *Lee et al.*, 2020), and others find that in a few cases the SF can be boosted by a factor of several (*Bekki*, 2013). These simulations span a range of galaxy masses, RP strengths, and numerical implementations, and therefore cannot yet be combined into a coherent picture.

A growing body of literature has simulated the impact of magnetic fields on ram pressure stripped galaxies. While magnetohydrodynamic (MHD) simulations have shown that draping of a magnetized ICM (*Lyutikov*, 2006; *Ruszkowski et al.*, 2007, 2008; *Dursi and Pfrommer*, 2008; *Pfrommer and Dursi*, 2010; *Ruszkowski et al.*, 2014) helps to reproduce the smooth (as opposed to clumpy) morphology of RPS tails in agreement with recent observations (*Müller et al.*, 2021), they find little impact on the gas stripping rate compared to purely hydrodynamic simulations (*Ruszkowski et al.*, 2014). However, *Ruszkowski et al.* (2014) find an increase in magnetic pressure along the disk due to draping. Similarly, simulations with disk magnetic fields find little impact on the stripping rate as long as the gas surface density is not impacted (*Tonnesen and Stone*, 2014; *Ramos-Martínez et al.*, 2018). Interestingly, *Ramos-Martínez et al.* (2018) find magnetized, flared disks act to deflect ICM material towards the galactic center region.

In contrast, the effect of cosmic rays (CR) on RPS remains largely unexamined. *Bustard et al.* (2020) performed simulations including CR, radiative cooling, and the derived star formation history of the Large Magellanic Cloud. They showed cosmic-ray driven galactic winds in combination with RPS can contribute to the Magellanic

Stream. To our knowledge, CR have never been studied for more massive L_* galaxies in a cluster environment. Yet CR have shown to play a crucial role in the evolution of isolated galaxies (*Enßlin et al.*, 2007; *Everett et al.*, 2008; *Uhlig et al.*, 2012; *Booth et al.*, 2013; *Salem and Bryan*, 2014; *Simpson et al.*, 2016; *Girichidis et al.*, 2016, 2018; *Pfrommer et al.*, 2017a,b; *Wiener et al.*, 2017, 2019; *Ruszkowski et al.*, 2017; *Farber et al.*, 2018; *Butsky and Quinn*, 2018; *Heintz and Zweibel*, 2018; *Holguin et al.*, 2019; *Chan et al.*, 2019; *Ji et al.*, 2020; *Hopkins et al.*, 2020, 2021; *Semenov et al.*, 2021, see *Zweibel* 2017 for a review).

Including CR is essential to understanding the physics underlying observations of RPS galaxies. The nonthermal pressure of CR tends to produce disks of larger scale-height, which should be more easily stripped. Likewise, CR driven galactic winds tend to be cooler and higher density than thermal outflows, suggesting more efficient removal of the neutral medium from galaxies. On the other hand, previous work has shown CR suppress the star formation rate in galaxies, as their nonthermal pressure counteracts contraction of gas to star-forming densities. Cosmic ray models with consequently reduced stellar feedback may exhibit weaker outflows, diminishing the amount of gas that is stripped.

Beyond the dynamics of RPS, CR are fundamental towards understanding radio continuum observations of RPS galaxies, the measurements of which indicate a global radio excess compared to the far-infrared (FIR) to radio correlation (FRC) (*Dickey and Salpeter*, 1984; *Beck and Golla*, 1988; *Yun et al.*, 2001; *Paladino et al.*, 2006). Since enhanced star formation would boost both the radio and the FIR (*Lacki et al.*, 2010), previous work suggested magnetic compression by the ICM wind on the leading edge of the galaxy could explain the boosted radio emission (*Scodeggio and Gavazzi*, 1993).

However, *Murphy et al.* (2009) utilized *Spitzer* FIR and VLA radio continuum imaging to show a *paucity* of radio emission on the leading edge of the galaxy's orbital motion, precisely where one would expect magnetic compression to dominate. Nevertheless, they observe global radio enhancement. The local radio deficits with global radio enhancement was confirmed by *Vollmer et al.* (2009, 2010, 2013) in Virgo cluster galaxies with multiwaveband measurements. They propose that both the local deficits and global enhancement of radio emission can be explained by variations in the cosmic-ray electron number density.[1] Although the magnetic field is compressed on the leading edge, cosmic-ray electrons may be easily stripped and their consequently low density suppresses the radio emission. Meanwhile, shocks driven into the ISM by the interaction with the ICM can re-accelerate CR, boosting the global radio emission. However, *Pfrommer and Dursi* (2010) suggest magnetic draping can explain the deficits in radio emission.

In this work, we determine the impact of CR and their transport, on properties of galaxies undergoing RPS. The outline of this paper is as follows: In §4.4 we describe the initial conditions, boundary conditions, galaxy model, and numerical methods utilized to perform this work including magnetohydrodynamics (MHD), CR, radiative cooling, self-gravity of the gas, star formation, and stellar feedback. In §4.5 we present and discuss our results. In §4.5.1 we consider the morphological evolution of the simulations we performed, finding CR crucially modify the outflows in isolated galaxies, yet do not evidently modify the morphology when galaxies undergo RPS. Thus, the stripping rates analyzed in §4.5.2 do not show much difference with or without CR. However, in §4.5.3 we find cosmic rays protect low-temperature gas from being stripped, possibly helping to explain observations of molecular gas in RPS tails. Cosmic rays dramatically influence star formation, as we show in §4.5.4. Intriguingly, we find in §4.5.5 that CR modify the accretion rate onto the galactic center with important implications for observations of AGN in RPS galaxies. The transport of CR fundamentally impacts the radio emission, which we discuss in §4.5.6.

---

[1] The radio emission is expected to be produced via synchrotron emission as the CR electrons gyrate along magnetic field lines.

We indicate limitations of our study and directions for future work in §4.6. Finally, we conclude in §4.7.

4.4 Methods

4.4.1 Numerical Techniques

We performed our simulations using the adaptive mesh refinement MHD code FLASH 4.2.2 (*Fryxell et al.*, 2000; *Dubey et al.*, 2008), with the directionally unsplit staggered mesh (USM) solver (*Lee and Deane*, 2009; *Lee*, 2013). The USM is a finite volume, high order Godunov scheme that utilizes constrained transport to satisfy the solenoidal constraint of Maxwell's equations to machine precision.

Additionally, we include self-gravity, radiative cooling, star formation and feedback as source and sink terms in the MHD equations. We include the passive advection of a concentration variable C, used to mark the initial disk gas[2]. We further extend the MHD equations to include CR as a second ultrarelativistic fluid (*Yang et al.* 2012; *Yang et al.* 2013; *Yang and Ruszkowski* 2017; *Ruszkowski et al.* 2017; *Holguin et al.* 2019); see *Farber et al.* (2018) for the system of equations we solve.

To include self-gravity of the baryons (gas and stellar population particles[3]) we solve the Poisson equation using the Huang & Greengard multigrid solver in FLASH (*Huang and Greengard*, 1999; *Ricker*, 2008). The multigrid solver implemented in FLASH extends *Huang and Greengard* (1999) for compatibility with FLASH's numerical structure, namely, finite volume discretization of the fluid equations with shared data on an oct-tree mesh, enabling efficient parallelization. That is, the multigrid method utilizes a direct solver for individual mesh blocks; see *Ricker* (2008) for further details.

---

[2] We set C = 1 in the disk and zero elsewhere.

[3] We utilize static potentials to include the gravitational influence of pre-existing stars; stellar population particles form during the simulation runtime.

We utilized the hybrid scheme for radiative cooling and heating of *Gnedin and Kravtsov* (2011). The implementation automatically switches between an explicit and implicit solver depending on the timestep constraint, enabling efficient and accurate treatment of radiative cooling and heating. For the rates, we interpolate to the nearest temperature and density using a table generated with Cloudy (*Ferland et al.*, 1998) assuming a constant solar metallicity and a constant metagalactic UV background; see, e.g., *Semenov et al.* (2021) for further details.

To accelerate the computations we impose a minimum timestep $\mathrm{dt}_{\mathrm{min}} = 10^4$ yr. We do so while maintaining numerical stability by limiting the bulk and generalized sound speeds to

$$v_{\mathrm{max}} \leq C_{\mathrm{cfl}} \frac{\Delta x}{\Delta t_{\mathrm{min}}} \tag{4.1}$$

where $C_{\mathrm{cfl}} = 0.2$ is the Courant-Friedrichs-Lewy number and Δx is the width of a cell.

We impose the speed limit via dissipation of thermal and CR energy such that the generalized sound speed obeys the speed limit $c_s = \sqrt{(\gamma_{\mathrm{th}} p_{\mathrm{th}} + \gamma_{\mathrm{cr}} p_{\mathrm{cr}})/\rho}$ and similarly for the bulk speed. Rather than limiting the Alfven speed directly, we utilize the hybrid Riemann solver implemented in FLASH, as modified to utilize the HLLC Riemann solver in smooth regions and the LLF Riemann solver in shock-detected regions for increased numerical stability (Dongwook Lee, priv. comm., 2020).

We perform our simulations in a box of dimensions (-32 kpc, 32 kpc)^3 with the galaxy centered at the origin with the spin axis pointing in the z-direction. We uniformly resolve —z— ¡ 4 kpc with 7 levels of refinement such that our galactic disk achieves a resolution of 127 pc and resolution degrades away from the galactic disk to a base grid with 4 levels of refinement and a physical resolution of ∼1 kpc.

Note that our box is relatively small to minimize the resolution elements covering —z— ¡ 4 kpc; we adopt such a step-wise refinement pattern to avoid “corners” of different resolution elements, which we found produced spuriously reflected waves and generated unphysical structures in the magnetic field.

We employ diode boundary conditions (modified to prevent inflow while including self-gravity, see Appendix 4.8) on all box faces. For the `FaceOn` and `EdgeOn` runs, after waiting 40 Myr to allow the initial conditions to relax, we inject a wind through the -z and -y boundaries, respectively, following the parameters of *Ruszkowski et al.* (2014). That is, we model an ICM wind with a density of $\mathrm{n_{wind}} = 5 \times 10^{-4}\,\mathrm{cm}^{-3}$, temperature $\mathrm{T_{wind}} = 7 \times 10^{7}\,\mathrm{K}$, magnetic field strength of $2\,\mu\mathrm{G}$ perpendicular to the wind, zero along the direction of the wind, and a maximum wind speed of 1300 km/s. We use an accelerating profile of the wind speed to model the orbital motion of the galaxy falling towards the center of the cluster (*Tonnesen*, 2019), following the model of *Ruszkowski et al.* (2014), namely $v_w(t) = f(t) v_{\mathrm{max,w}}$ where

$$f_{\mathrm{in}}(t) = 1 - \begin{cases} 1 - 1.5x^2 + 0.75x^3 & \mathrm{if} x \leq 1 \\ 0.25(2-x)^3 & \mathrm{if} 1 < x < 2 \\ 0 & \mathrm{if} x \geq 2 \end{cases} \tag{4.2}$$

with $x \equiv t/\Delta t$ and $\Delta t \approx 59\,\mathrm{Myr}$. That is, the wind reaches maximum velocity at 158 Myr (since we delay onset of the wind 40 Myr) and is constant thereafter. See Table 4.1 for a list of the parameters employed in this study.

4.4.1.1 Star Formation and Feedback

We employ the star formation and stellar feedback prescriptions used in the ART (*Kravtsov*, 1999; *Kravtsov et al.*, 2002; *Rudd et al.*, 2008; *Gnedin and Kravtsov*, 2011) simulations of galaxy evolution (*Semenov et al.*, 2016, 2017, 2018, 2021). That is, we permit gas to form stars when the gas density exceeds a critical value $n_{*,\mathrm{min}} = 1\,\mathrm{cm}^{-3}$ with the star formation rate density ρ_* parameterized to match the Kennicutt-Schmidt relation (*Schmidt*, 1959; *Kennicutt Jr*, 1998):

Table 4.1: Numerical Parameters.

Name	Value
dt_{min}	10^4 yr
C_{cfl}	0.2
$\rho_{*,\mathrm{min}}$	1 cm^{-3}
E_{SN}	10^{51} erg
f_{th}	0.717
f_{cr}	0.1
$\kappa_{\parallel}$	$3 \cdot 10^{28}$ cm^2 s^{-1}
$\kappa_{\perp}$	0
$M_{*,\mathrm{disk}}$	10^{11} $M_{\odot}$
$M_{*,\mathrm{bulge}}$	10^{10} $M_{\odot}$
$M_{\mathrm{gas,disk}}$	10^{11} $M_{\odot}$
$M_{\mathrm{DM,core}}$	$1.1 \cdot 10^{11}$ $M_{\odot}$
$r_{0,*,\mathrm{disk}}$	4 kpc
$r_{0,\mathrm{gas,disk}}$	7 kpc
$r_{0,*,\mathrm{bulge}}$	0.4 kpc
$z_{0,*,\mathrm{disk}}$	0.25 kpc
$z_{0,\mathrm{gas,disk}}$	0.4 kpc
$\mathrm{R}_{\mathrm{disk}}$	26 kpc
$\mathrm{B}_{0,\mathrm{x}}$	1 μG
a_0	10^3
$\rho_{0,\mathrm{CGM}}$	9.2×10^{-5} cm^{-3}
$\mathrm{T}_{0,\mathrm{CGM}}$	4.15×10^6 K
$\mathrm{n}_{\mathrm{wind}}$	5×10^{-4} cm^{-3}
$\mathrm{T}_{\mathrm{wind}}$	7×10^7 K
$\mathrm{v}_{\mathrm{max,wind}}$	1300 km/s
$\mathrm{B}_{\perp,wind,1}$	2×10^{-6}G
$\mathrm{B}_{\perp,wind,2}$	2×10^{-6}G
$\mathrm{B}_{\parallel,wind}$	0
$\mathrm{L}_{\mathrm{box}}$	64.8 kpc
$\mathrm{dx}_{\mathrm{min}}$	127 pc
$\mathrm{dx}_{\mathrm{max}}$	1 kpc
$\lvert\mathrm{z}\rvert_{\mathrm{dx,min}}$	4 kpc

$$\dot{\rho}_* = \epsilon_{\rm ff} \frac{\rho}{t_{\rm ff}} \tag{4.3}$$

where $\epsilon_{\rm ff}$ is the star formation efficiency per free-fall time $t_{\rm ff}$. We set $\epsilon_{\rm ff} = 0.01$ in agreement with observationally inferred low local star formation and long galactic depletion times of star-forming gas (see, *Krumholz and Tan* 2007; *Leroy et al.* 2017; *Semenov et al.* 2018).

When the gas density of a cell exceeds the minimum density for star formation we create a stellar population particle with the mass proportional to N, where N is the number of occurrence, drawn from a Poisson distribution, characterized by the expected value $\lambda = \rho_* dV dt/m_*, min$. However, we limit the value of N to not exceed $m_{\rm gas}/m_{*,\rm min}$, where $m_{*,\rm min} = 10^4\,M_\odot$ is the minimum stellar population mass we enforce to avoid creating a computationally intractably large number of particles. We also require the total stellar population particle mass not to exceed $2/3\ m_{\rm gas}$ to avoid consuming all the gas in the cell. Upon creation of the stellar population particle, we remove its mass from the gas in the cell it inhabits.

For 40 Myr immediately succeeding the creation of a stellar population particle we apply feedback from massive stars, modeling proto-stellar jets, massive stellar winds and radiation pressure, preceding type II supernovae. We sample our stellar population particles with a Chabrier IMF to determine the contribution from massive stars $\gtrsim 8\,M_\odot$. For each massive star we inject $0.1\ \times 10^{51}$ erg as cosmic-ray energy, as well as thermal energy and momentum according to the subgrid model of *Martizzi et al.* (2015).

The *Martizzi et al.* (2015) momentum feedback subgrid model takes into account local conditions and our resolution to inject the appropriate amount of momentum produced during the (unresolved) Sedov-Taylor phase (see also *Walch and Naab* 2015; *Kim and Ostriker* 2015; *Iffrig and Hennebelle* 2015). We boost the injected momentum by a factor of 5 to account for the unresolved clustering of supernovae (*Gen-*

try et al., 2017, 2019), the influence of CR on the supernova momentum deposition (*Diesing and Caprioli*, 2018) and to account for advection errors (*Agertz et al.*, 2013; *Semenov et al.*, 2018).

4.4.1.2 Cosmic Ray Models

We bracket the parameter space of CR transport and calorimetry via three cases: (1) No CR (`NoCR`), i.e., modeling the case of complete calorimetry. (2) CR that simply advect with the thermal gas (`ADV`). This case models unresolved tangled structure of the magnetic field in the galactic disk, preventing CR from escaping into the circumgalactic medium (CGM) or effectively a strong suppression of cosmic-ray diffusion and cooling near star formation sites (*Semenov et al.*, 2021). (3) Cosmic rays anisotropically diffuse along magnetic field lines with a diffusion coefficient parallel to the magnetic field of 3×10^{28} cm^2 s^{-1} and zero perpendicular diffusion (`DIF`). We note that these three cases are meant to bracket the possible results of more detailed CR transport modeling, which remains highly uncertain (see the dozens of models of *Hopkins et al.* 2021).[4]

4.4.2 Galaxy Model

We model a massive spiral galaxy with a flat rotation curve $v_{\rm disp} = 200\,{\rm km/s}$, composed of a gaseous disk, hot halo, stellar disk, stellar bulge, and dark matter halo initially in hydrostatic equilibrium (see *Tonnesen and Bryan* 2009; *Tonnesen and Bryan* 2010).

To directly follow *Roediger and Brüggen* (2006) we use a Plummer-Kuzmin potential for the stellar disk (*Miyamoto and Nagai*, 1975), a Hernquist profile for the stellar bulge (*Hernquist*, 1993), and a *Burkert* (1995) potential for the dark matter

---

[4] That is, `ADV` can represent the limiting case of very slow CR transport, `NoCR` models the limit of very fast transport, and the diffusion coefficient adopted for `DIF` is a moderate value that should be near the peak wind driving efficincy (*Salem and Bryan*, 2014) and is motivated by models of cosmic-ray propagation (see *Grenier et al.* 2015 and references therein).

halo [5] (see Table 4.1 for the masses and scale lengths of each component).

We employ the same magnetic field configuration initial conditions as model TORL of *Tonnesen and Stone* (2014). Namely, we initialize the magnetic field to be weak in the galactic central region (where the velocity field changes rapidly), peaking in strength a few kpc from the galactic center, diminishing gradually with increasing galactic radius, and set to zero outside the disk. That is, we employ the following vector potential (with A_z set to a constant outside the disk)

$$A_x = A_y = 0 \tag{4.4}$$

$$A_z = \sqrt{a_{zf}} e^{-6R_{\rm cyl}} \frac{-6\sin(2.5R_{\rm cyl}) - 2.5\cos(2.5R_{\rm cyl})}{6^2 + 2.5^2} \tag{4.5}$$

$$a_{zf} = 1000(-|z| + 1)^{80} \tag{4.6}$$

Note that the cutoff in magnetic field strength at the disk-edge ensures the magnetic pressure is subdominant to the thermal pressure, reducing disk expansion as well as growth of the magnetic field due to shear between the disk and the CGM.

The plasma beta, which is the ratio of thermal to magnetic pressures, $\beta \equiv P_{\rm gas}/P_{\rm mag}$ ranges from 100 to a maximum of ~2 in the disk midplane a few kpc from the galactic center region (see Figure 2 of *Tonnesen and Stone* 2014). Since the magnetic pressure is subdominant to the thermal pressure the magnetic field does not have a strong effect on the disk. The chosen magnetic field morphology enables easier comparison to our previous work (*Tonnesen and Stone*, 2014) as it is reproducible, reduce variability due to instabilities, and are divergence-free.

---

[5] This potential is consistent with observed rotation curves (*Trachternach et al.*, 2008).

Table 4.2: Nomenclature.

Name	Description
f_{th}	thermal fraction of SN energy.
f_{cr}	cosmic-ray fraction of SN energy.
dx	cell width.
MHD	Magnetohydrodynamics.
USM	Unsplit Staggered Mesh.
RPS	Ram Pressure Stripping.
SFR	Star Formation Rate.
SNe	Supernovae.
ICM	Intra-cluster Medium.
CGM	Circum-galactic Medium.
`Isolated`	No ICM wind.
`FaceOn`	ICM wind parallel to galactic spin axis.
`EdgeOn`	ICM wind perpendicular to galactic spin axis.
`NoCR`	No cosmic rays.
`ADV`	Cosmic rays only advect.
`DIF`	Cosmic rays advect and diffuse.

4.5 Results & Discussion

We begin the presentation of our results in Section 4.5.1 by graphically illustrating the nine runs we have analyzed and indicating their morphological evolution in Figures 4.1 through 4.3. Then we explore the impact of CR on the stripping rates in Section 4.5.2 and the gas phase distribution in Section 4.5.3. In Section 4.5.4 we discuss the impact of CR and their feedback on the star formation rate in galaxies undergoing RPS at cluster outskirts. We consider the impact of CR on the accretion of gas toward the galactic center in 4.5.5. See Table 4.2 for our nomenclature.

4.5.1 Galactic Morphology

In this section we analyze the morphological evolution of galactic disks. We performed a grid of nine simulations, composed of three CR models and three galaxy models. We performed simulations (a) without CR (`NoCR`), (b) where CR purely advect with the gas (`ADV`), and (c) including the anisotropic diffusion of CR along

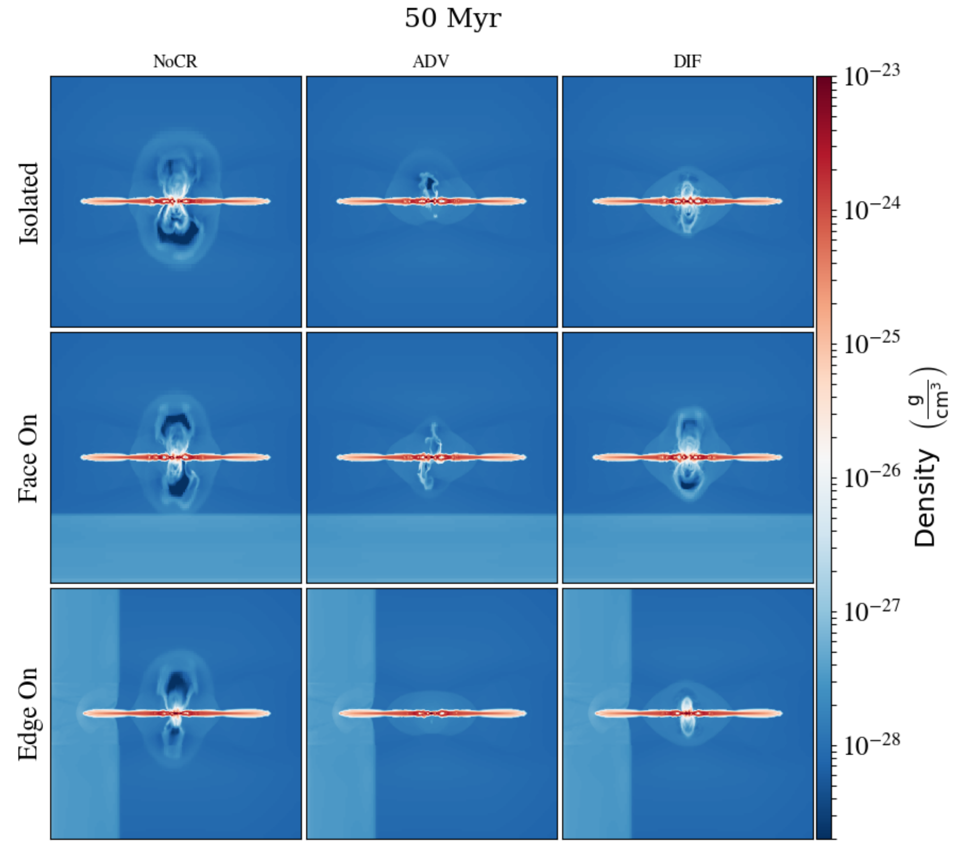

Figure 4.1: Slice plots at 50 Myr, shortly after the galaxies encounter an ICM wind (when appropriate). `NoCR` (left), `ADV` (middle), and `DIF` (right) physics cases are displayed for the `Isolated` (top), `FaceOn` (middle), and `EdgeOn` (bottom) runs. Red colors indicate high density while blue colors indicate low densities.

magnetic field lines (`DIF` see Section 4.4.1.2 for further details). For each CR model we simulated (i) field galaxies not subject to any ICM wind (`Isolated`), and galaxies falling into a cluster such that the spin axis points (ii) face-on (`FaceOn`) or (iii) orthogonal to (`EdgeOn`) the direction of the orbital motion.

In all cases, the gas distribution collapses towards the midplane as a result of radiative cooling removing thermal pressure support. The resulting high densities at the midplane allow stars to form, whose feedback begins to launch a nuclear outflow (see Section 4.4.1.1 for further details on our star formation and feedback methods). After 40 Myr the star formation and feedback cycle is well underway yet still quite similar for all physics cases (see Figure 4.6). At this time we turn on the ICM wind (for non-`Isolated` runs). At 50 Myr (see Figure 4.1) the ICM wind has just begun to interact with the `FaceOn` & `EdgeOn` runs. At this time, the `NoCR` runs have the most extended outflow structure while the `ADV` runs have a relatively weak wind.

As expected from the classical Gunn & Gott model for RPS, the ensuing ISM-ICM interaction proceeds from the outermost radii of the disk, where gas is beginning to be stripped by 100 Myr (see Figure 4.2). The `Isolated` runs have now developed more extended galactic wind structures into the CGM. Note the `DIF` run has developed a frothy higher density galactic wind structure compared to the relatively low density "mushroom" ejecta of the `NoCR` case, while the weaker galactic wind in the `ADV` case has not propagated as far into the CGM as `NoCR` or `DIF`. The higher density outflow driven with CR is consistent with previous models of isolated galaxies with cosmic-ray feedback (see *Girichidis et al.* 2018).

Meanwhile, cases with an ICM wind are beginning to diverge from their `Isolated` galaxy counterparts. Most noticeable is the higher density of the ICM ($\rho \sim 10^{-27}$ g cm^{-3}) compared to the CGM ($200\rho_{\rm crit} \sim 10^{-28}$ g cm^{-3}). In the `FaceOn` runs the development of a bowshock ~20 kpc upstream of the disk is quite evident. Moreover, RPS has begun to affect the disks: the outermost portion of the disks are slightly

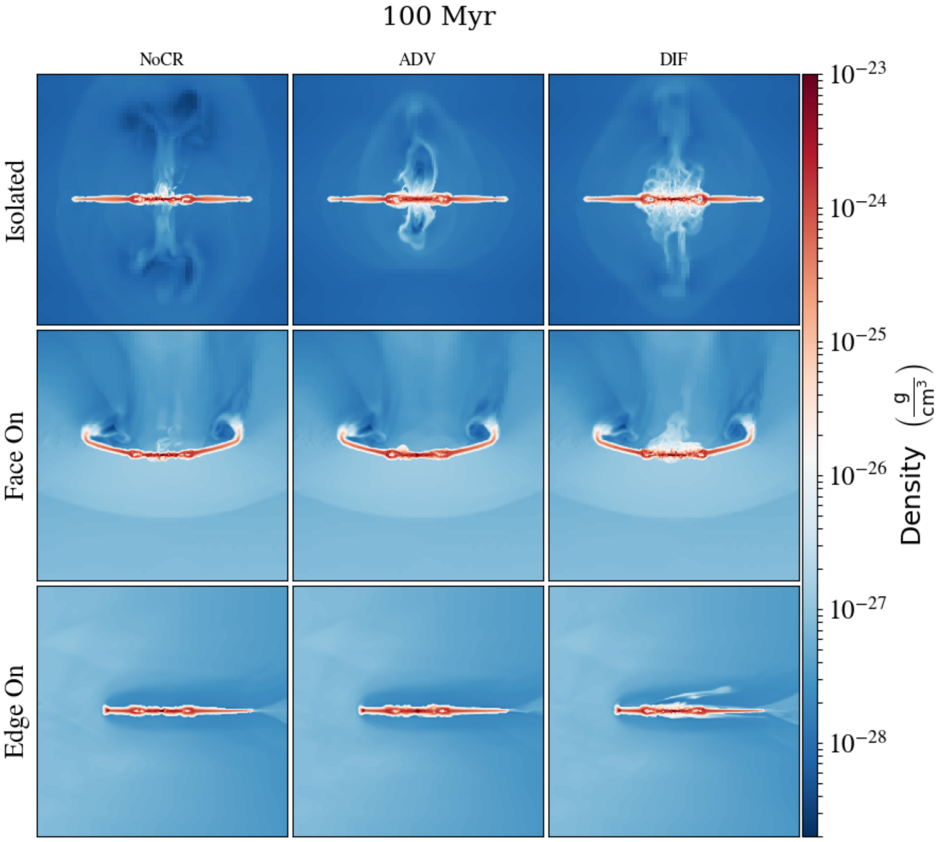

Figure 4.2: Same as Figure 4.1 but at 100 Myr. Galactic winds have developed for the `Isolated` galaxies while for `FaceOn` disk gas is bowed backward due to ram pressure. The galactic wind material is absent in the case of `EdgeOn` as it is readily stripped.

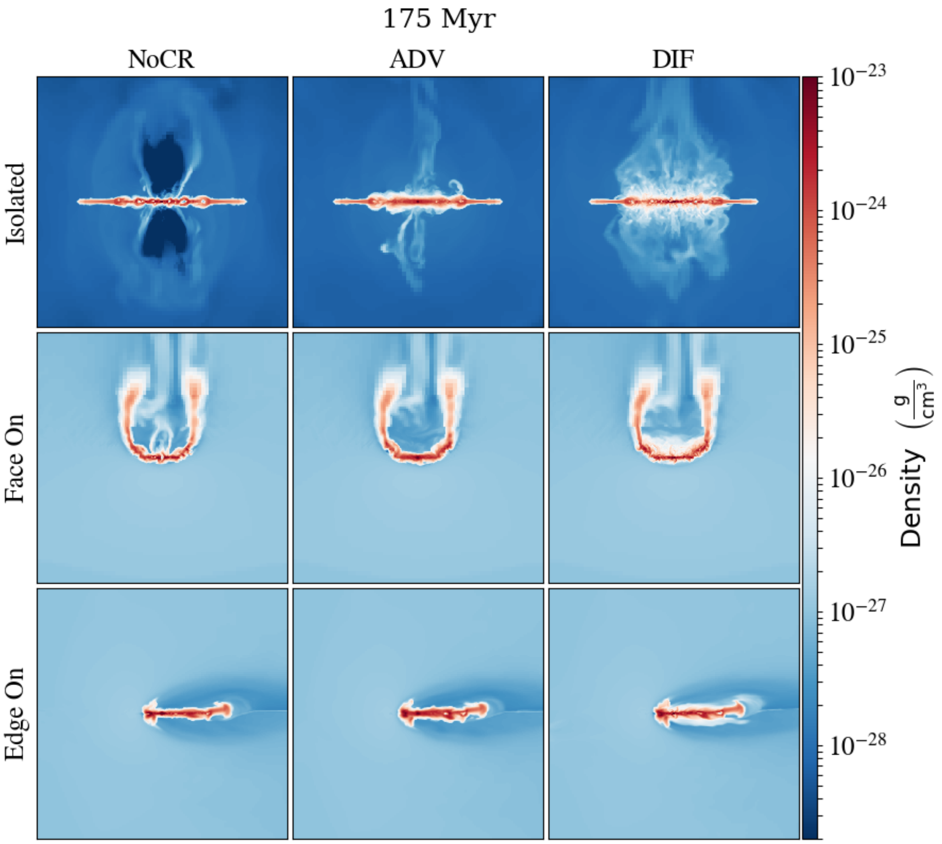

Figure 4.3: Same as Figure 4.1 but at 175 Myr. The `Isolated` galaxies' winds have continued to expand into the CGM. The `FaceOn` and `EdgeOn` galaxies' disks are distorted due to the ram pressure of the ICM wind.

bowed downstream from the RP of the colliding ICM wind.

For the `EdgeOn` runs the disks are slightly pushed downstream at 100 Myr (see Fig. 4.2), with notably absent galactic wind bubbles – stripping of galactic wind material has been "caught-in-the-act" for the `DIF` case. Otherwise the galaxies in the `EdgeOn` case do not appear very disturbed.

As the ICM-ISM interaction proceeds, the `FaceOn` and `EdgeOn` cases diverge more drastically from the `Isolated` galaxies. At 175 Myr (see Figure 4.3) the galactic winds of the `Isolated` runs' have further developed. The `NoCR` run has evacuated a large scale, biconical, low density ($\rho \sim 10^{-29}\,\mathrm{g\ cm^{-3}}$) cavity from its nuclear region into the CGM, in shape reminiscent to the Fermi bubbles (*Su et al.*, 2010). In contrast, the `DIF` run has developed a frothy, disk-wide outflow whose relatively high-density ($\rho \sim 10^{-26}\,\mathrm{g\ cm^{-3}}$) is in better agreement with observations of the CGM (*Werk et al.*, 2013). Note that stellar feedback similarly occurs to a larger radius in the disk now in the `NoCR` case as can be noted by the slightly thicker disk compared to the disk outskirts. In the `ADV` case, the outflow has largely shut off and the gas at large scale heights from the disk is returning in a fountain flow. The main impact of cosmic-ray feedback in this case is the thickening of the gaseous disk due to the nonthermal pressure provided by CR, which efficiently suppresses star formation.

Meanwhile, the pushing of the now maximum RP wind (see Section 4.4.1 for the acceleration profile) has bowed back the `FaceOn` disks. Stripping from the ends of the warped disk gas downstream (and out of the computational domain) is evident possibly forming a tail structure (but studying the RPS tail is beyond the scope of this work). The high-density disk gas for the `FaceOn-ADV` run is thicker than the other physics cases. Reminiscent of the frothy outflow of the `Isolated` disk, the `FaceOn-DIF` case exhibits a low density skin of gas surrounding the higher density midplane gas as seen in white in our slices. The low density skin possesses a larger scale height downstream, as it is protected by the "shadow" of the disk.

While the `FaceOn` disks are severely warped downstream, the `EdgeOn` disks appear to exhibit a fairly strong compression on the leading edge, forming a comet-like structure with a distinct high density "head" just upstream of (stellar) galactic center and a tail of dense disk gas downstream. Again, the `ADV` run exhibits a somewhat thicker structure of dense disk gas while the `DIF` galaxy possess a low density skin, as an outflow (which is rapidly stripped) is driven by diffusing CR.

While we have indicated the most salient differences between our CR physics cases,

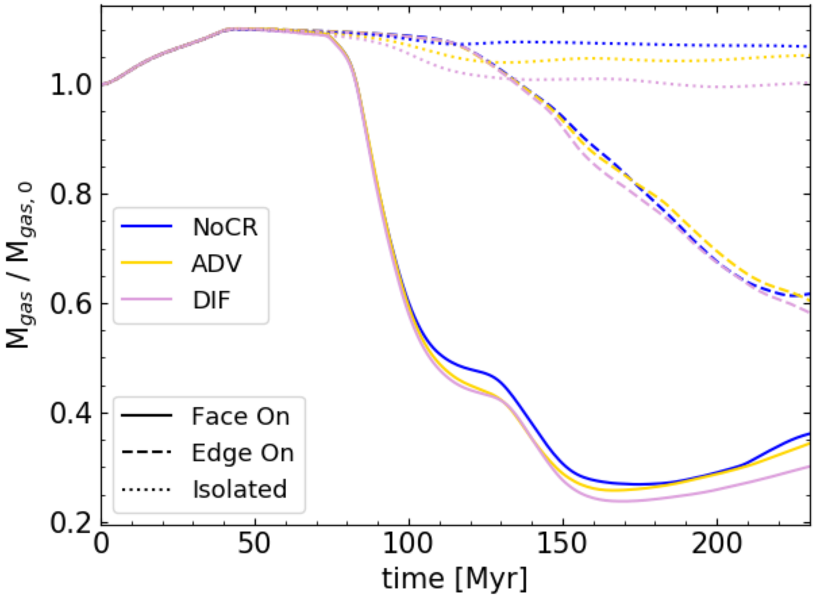

Figure 4.4: Evolution of the gas mass in the disk as a function of time. We define disk gas mass to possess a concentration tracer threshold $C > 0.6$ within a cylinder of radius 28.6 kpc and height ±1 kpc from the midplane.[7] Cosmic ray physics cases `NoCR`, `ADV`, and `DIF` are indicated as blue, gold, and plum curves, while the ICM wind types are indicated as solid, dashed, and dotted curves for `FaceOn`, `EdgeOn`, and `Isolated` respectively. The stripping rate appears to be fairly insensitive to cosmic ray physics.

the most striking observation is how relatively *similar* the morphology is for galaxies subjected to RPS. This is shocking especially after one considers the radical differences of the galactic winds of the `Isolated` cases. Nevertheless, previous studies have found RPS proceeds at a rate largely unaffected by nonthermal forces (e.g., magnetic fields, see *Tonnesen and Stone* 2014; *Ruszkowski et al.* 2014), as suggested by the good agreement between observations and the Gunn & Gott criterion. In the next section, we investigate the impact of CR on the RPS rate.

4.5.2 Stripping

To determine the impact of CR physics on the RPS rate, we investigate the amount of gas remaining in the disk in our simulations. We define disk gas as possessing a tracer fraction $C > 0.6$ contained within a cylinder of radius 28.6 kpc and height ±1 kpc from the disk midplane.

In Figure 4.4 we show the mass in the disk as a function of time for our nine simulations. We utilize solid, dashed, and dotted lines to indicate the `FaceOn`, `EdgeOn`, and `Isolated` runs while blue, gold, and plum curves represent `NoCR`, `ADV`, and `DIF` physics cases. During the first 40 Myr the disk mass increases due to radiative cooling induced collapse onto the disk midplane. The disk mass stabilizes until ~75 Myr when the impact of the ICM wind begins to differentiate the evolution.

From 75-150 Myr the `FaceOn` runs are efficiently stripped of ~80% of their disk mass. As some stripped material enters the "shadow" of the remaining disk and is protected from acceleration to the escape velocity, some material falls back onto the disk from ~175-230 Myr. In contrast, the `EdgeOn` runs are more slowly stripped (maintaining $\gtrsim$90% of their initial disk gas mass by 150 Myr and ~60% by 230 Myr) owing to the reduced cross-section for ISM-ICM interaction, in agreement with previous work (*Roediger and Brüggen*, 2006; *Jáchym et al.*, 2009). The `EdgeOn` runs lack a fallback episode owing to the lack of protective "shadow."

Meanwhile, the `Isolated` runs maintain most of their disk mass as expected with the disk gas mass loss due primarily to galactic winds. Interestingly, the `ADV` run ejects more disk gas mass initially than the `NoCR` run due to the contrast between the hot, low density cavities driven in the `NoCR` case compared to the `ADV` case (see Figure 4.3). Both `ADV` and `DIF` runs exhibit periodic fountain flows (see the oscillatory behavior of the dotted lines) or accretion dominating over the outflow, whereas the `NoCR` disk gas mass is monotonically decreasing.

As anticipated from the largely similar evolution of the `NoCR`, `ADV`, and `DIF` cases of the `FaceOn` and `EdgeOn` runs (see Figures 4.1-4.3), the stripping rates do not differ widely between the physics cases (not more than ~15%, see Figure 4.4). However, knowing that the `Isolated` runs produce quite distinct galactic wind structures, the fact that CR play a minor role in the removal of gas from RPS galaxies is quite surprising. Nevertheless, we find CR physics does play a role in modifying the temperature-density phase space of cluster spirals, which we discuss next.

4.5.3 Gas Phase Distribution in the Disk

While the morphology and stripping rates are similar across our three cosmic-ray physics cases (`NoCR`, `ADV`, and `DIF`), examining the galactic disk in detail suggests CR play an interesting role in modifying galactic properties. We start with the phase space distributions of disk[8] gas temperature and density at 175 Myr in Figure 4.5. The columns from left-right show `NoCR`, `ADV`, and `DIF` physics cases respectively, and the rows from top-bottom display `Isolated`, `FaceOn`, and `EdgeOn` runs.

In agreement with previous work, the `Isolated` runs (top row) indicate that including CR permits the presence of low-density, low-temperature gas, as CR provide nonthermal pressure support (*Ji et al.*, 2020; *Butsky et al.*, 2020). Note the low temperature ridge at $T \sim 10^2\,\mathrm{K}$ (absent in `NoCR` runs). The low temperature ridge is dimmer (less yellow) for the `DIF` run related to less CR pressure in the disk supporting that gas. The ridge has a low-mass component extending to lower temperatures in the `DIF` case related to adiabatic cooling of the galactic wind.

Note that once the wind has impacted the galaxies, we expect that low-density gas will be preferentially removed due to its lower restoring force. Indeed, in the `NoCR` run this is clearly seen in both the `FaceOn` and `EdgeOn` runs at all temperatures. We also see a small increase in the amount of dense gas, particularly in the `EdgeOn` run, in agreement with our visual impression of gas compression in Figures 1-3.

However, the gas distribution is somewhat different in the stripped galaxies with CR. While above $\sim 10^4\,\mathrm{K}$, low density gas seems to be removed, at cooler temperatures more low-density gas survives than in the `NoCR` wind runs. We can understand this

---

[8] Note that we select ‘disk’ gas by applying a concentration threshold of $C > 0.6$ and require gas to fit within a cylinder of radius 28.6 kpc and height ±1 kpc from the midplane.

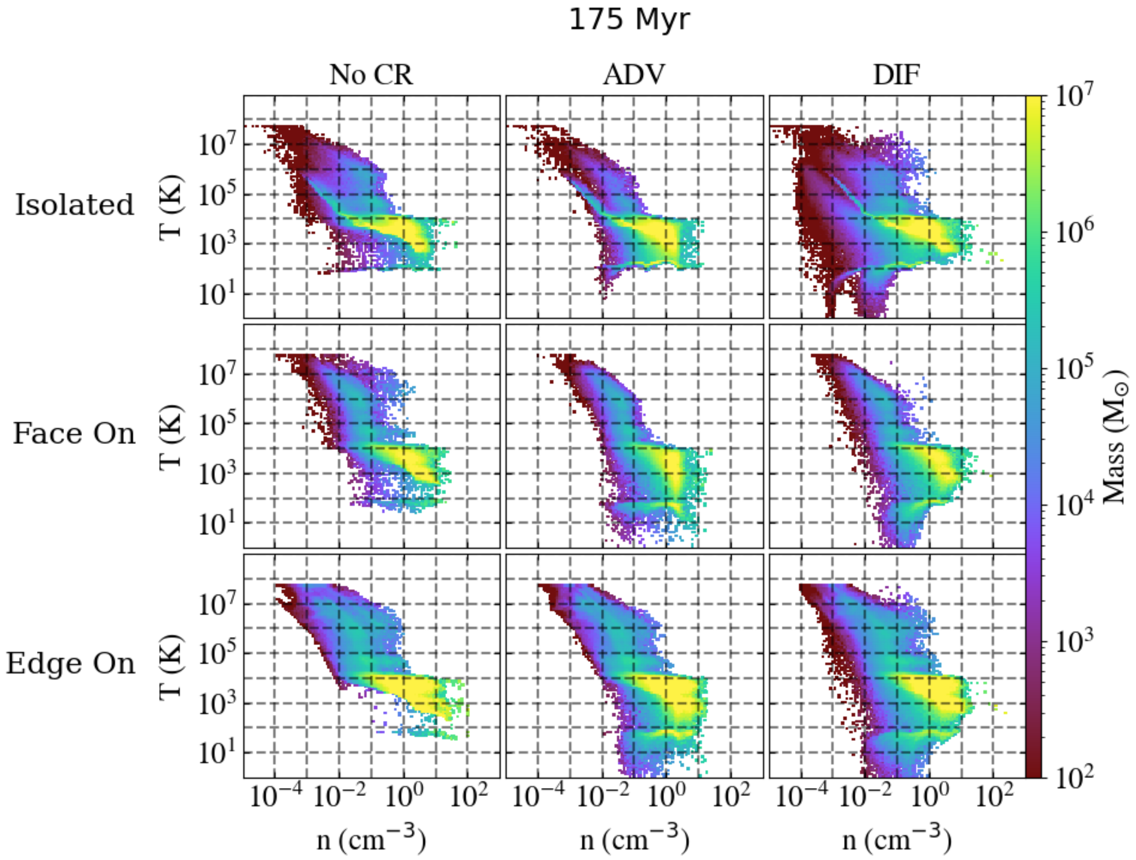

Figure 4.5: Gas temperature vs. number density phase plots at 175 Myr. The left, center, and right columns display `NoCR`, `ADV`, and `DIF` physics cases respectively, while the top, middle, and bottom rows show `Isolated`, `FaceOn`, and `EdgeOn` ICM wind (or lack thereof) run types. Bright (dark) colors indicate regions with much (little) gas mass. Dashed lines are intended to ease comparison across the various runs.

by the low-temperature ridge in the isolated versus wind runs.

The low temperature ridge is at slightly lower temperatures when RPS is turned on due to enhanced nonthermal pressures. An elevated magnetic field strength due to compression of the disk is the source of nonthermal pressure in the `NoCR` case. The low temperature ridge gets brighter when including CR and is brighter for `ADV` than `DIF` related to the concentration of CR in the disk. As we will show, CR production is enhanced due to increased SFRs with RP. The low temperature feature extends to lower temperature in the `DIF` case due to CR outside the disk. Although CR are swept away quickly in the `EdgeOn` case (as seen in Figure 4.3), they are also constantly replenished by star formation and subsequent feedback. In summary, the inclusion of CRs allows low-temperature, low-density gas to survive in ram pressure disks due to an increase in non-thermal pressure.

The `NoCR` runs show that RPS efficiently strips low density gas. However, galaxies subjected to RPS (middle and bottom rows) including CR (middle and right columns) contain low density gas that is otherwise stripped in the `NoCR` runs (left column; bottom left portion of each plot).

Probably the most interesting result is that RPS increases the amount of low-temperature gas and this RPS-induced is effect is stronger when CR are included (see §4.7).

4.5.4 Star Formation

Let us begin by examining the physical SFR in the top panel of Figure 4.6. As previously, we use blue, gold, and plum curves to respectively indicate `NoCR`, `ADV`, and `DIF` cases while solid, dashed, and dotted lines refer to the ICM wind cases of `FaceOn`, `EdgeOn`, and `Isolated`. All physics cases and ICM wind runs have similar SFR up to roughly 100 Myr. After that point, the ICM-ISM interaction begins to take effect with the SFRs clearly diverging. For all ICM wind runs `NoCR`, `DIF`, and `ADV`

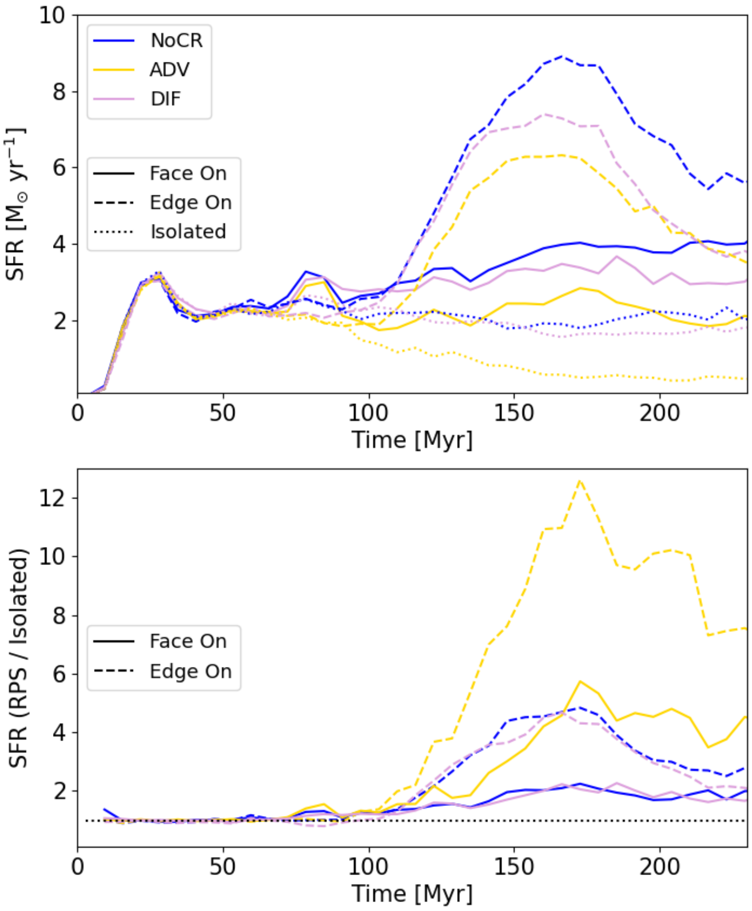

Figure 4.6: Time series of SFR (top) and ratio of SFR of the `FaceOn` (solid) or `EdgeOn` (dashed) runs to the `Isolated` (dotted) runs. `NoCR`, `ADV`, and `DIF` are marked as blue, gold, and plum colors, respectively. Clearly the `NoCR` runs have the highest SFR and `ADV` receives on average the largest boost in SFR when a galaxy is subjected to an ICM wind.

clearly have the highest to lowest respective SFRs with the `EdgeOn` runs exhibiting demonstrably higher SFR than `FaceOn` runs at 175 Myr.

Comparing the SFR of RPS galaxies to their isolated counterparts is more readily achieved looking at ratios in the bottom panel of Figure 4.6. Again, we observe significant departures in the SFRs of different ICM wind or cosmic-ray physics cases only after 100 Myr. Subsequently, `FaceOn-DIF` and `FaceOn-NoCR` show moderate enhancement of SFR over their `Isolated` counterparts in best agreement with observations (~ 0.2 dex enhancement of star formation, see *Vulcani et al.* 2018).

The `FaceOn-ADV` run achieves peaks of 4-6 times the value of `Isolated-ADV` (which is largely quiescent due to the buildup of cosmic-ray energy). The `NoCR-EdgeOn` run similarly initially attains a boost 4 times the `Isolated` run at 175 Myr. The `EdgeOn-ADV` run shows the most dramatic boost in SFR, exceeding an order of magnitude at ∼175 Myr. Since a fluid dominated by CR has an adiabatic index of 4/3 whereas a thermal plasma has an adiabatic index of 5/3, the CR fluid is more compressible. Thus, when the ICM wind impacts the disk in the `ADV` run which is dominated by cosmic-pressure, there is a larger increase in the density than the `DIF` or `NoCR` cases, explaining the boost in SFR.

Clearly the `EdgeOn-ADV` run is inconsistent with the much more modest boosts in star formation found by *Vulcani et al.* (2018); in fact, all the `EdgeOn` runs appear to be inconsistent with observations. *Roediger and Brüggen* (2006) found inclination makes a minor difference to RPS until $\gtrsim 60^o$, suggesting most spiral galaxies falling into a cluster can be modeled as `FaceOn`. Although both `FaceOn-DIF` and `FaceOn-NoCR` are consistent with observed SFR enhancements, the degeneracy may be broken when we consider the evolution of mass at the galactic center below.

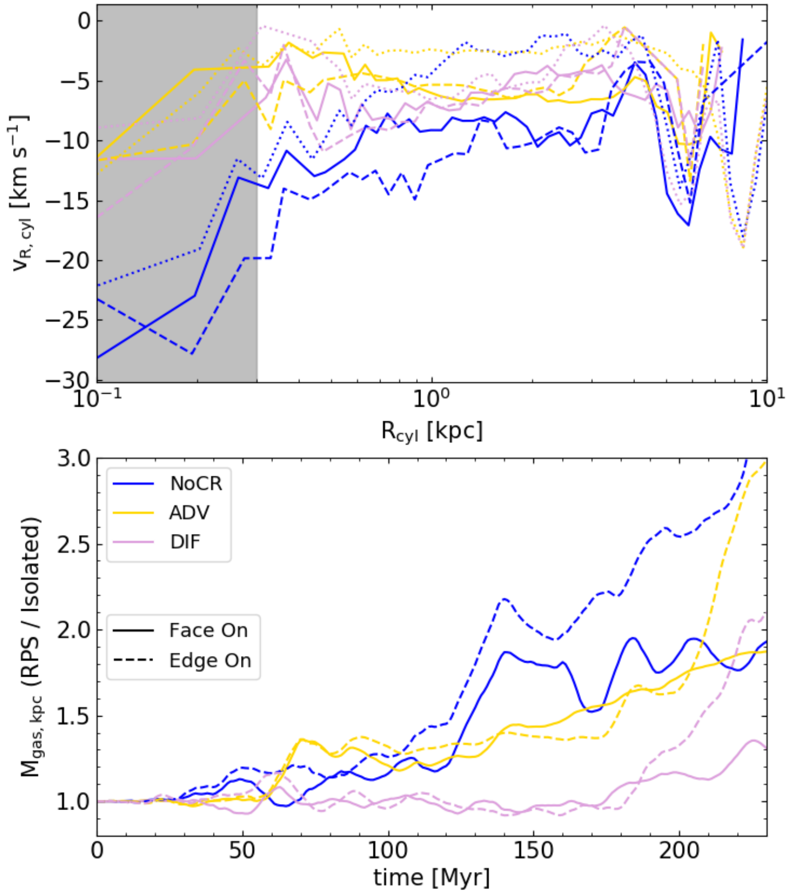

Figure 4.7: Top: Time-averaged negative (gas flowing towards the galactic center) cylindrical radial velocity as a function of cylindrical radius. The greyed out region samples less than 10 cells linearly so we caution against over-interpretation. Bottom: galactic center mass ratios of ram pressure stripping runs to `Isolated` counterparts, in this case defined as a sphere of radius 1 kpc centered on the galactic center. `NoCR`, `ADV`, and `DIF` physics cases are shown as blue, gold, and plum curves respectively. `FaceOn` and `EdgeOn` ratios are indicated by solid and dashed markers respectively.

4.5.5 Feeding the AGN: Accretion onto the Galactic Center

While the SFR plots appear degenerate between the `DIF` and `NoCR` models, the galactic accretion rate (Figure 4.7) appears to tell a different story. The top panel indicates the accretion rate of material flowing in the disk plane towards the galactic center. That is, we select disk gas (tracer concentration $C > 0.6$ within a cylinder of radius 28.6 kpc and height ±1 kpc from the midplane) and take a one-dimensional profile of the radially inward flowing velocity. We time-average the radial velocity at each radius from 100 - 230 Myr[9]. We indicate the `NoCR`, `ADV`, and `DIF` models as blue, gold, and plum curves, with the `FaceOn`, `EdgeOn`, and `Isolated` galaxies marked as solid, dashed, and dotted. In general, we see that RPS galaxies have enhanced accretion rates, in qualitative agreement with observations finding RPS galaxies have much higher AGN fractions than galaxies in the field (*Poggianti et al.*, 2017a; *Radovich et al.*, 2019). Moreover, the runs with CR appear to suppress galactic accretion, as the `NoCR` run clearly has the strongest accretion rate independent of inclination. Together with the SFR results, this suggests CR must be more weakly coupled to the disk gas. That is, either CR are transported faster or they rapidly experience strong Coulomb and hadronic losses. The accretion rate for the `Isolated` runs appear to be consistent with recent cosmological models that also find cosmic rays suppress accretiont (*Trapp et al.*, 2021).

For a clearer picture of the accretion onto the galactic center, we show in the bottom panel of Figure 4.7 the time evolution of the gas[10] mass within a sphere of radius 1 kpc emanating from the galactic center as a ratio of RPS runs to their `Isolated` counterparts. For example, we indicate with a blue solid curve the central 1 kpc gas mass for the ratio of `FaceOn-NoCR` to `Isolated-NoCR`. Until about 100 Myr, the galactic central mass is largely indistinguishable between ICM wind types and

---

[9] The SFR begins to divrge between the different runs at 100 Myr. We confirmed our results averaging 50 - 230 Myr.

[10] Note that the mass converted into stars is relatively modest and does not impact our conclusions.

CR physics cases (~20% difference). Subsequently, the ISM-ICM interaction drives accretion towards the galactic central region. The nonthermal pressure of CR suppress accretion and as a result, the central gas mass is nearly double for `FaceOn-NoCR` compared to `FaceOn-DIF`. In general, the `NoCR` runs exhibit the largest central masses followed by the `ADV` and then `DIF` runs.

At the end of our simulations, the `DIF` run has the least mass accreted in the galactic center. This may suggest CR suffer strong ~calorimetric losses, or that the diffusion coefficient must be much faster to reduce the coupling to disk gas, if strong accretion is required to match observations of high AGN fraction in RPS galaxies. However, we note that although weaker, the `DIF` RPS runs nevertheless have an elevated accreted mass in the galactic center compared to `Isolated` (that is, the ratio is greater than one); it would be interesting if future work can tease out the required accretion to trigger AGN.

Note that even in the `Isolated` runs the galactic center mass increases by a factor of two for cosmic-ray runs and a factor of four for `NoCR` (not shown here). Our magnetized disk is subject to the magnetorotational instability (MRI; *Balbus and Hawley* 1991) beyond ~4 kpc where the angular velocity begins to diminish radially outward (*Hawley and Balbus*, 1999). Since the MRI growth rate is proportional to orbital frequency, growth is strongest for the inner parts of the disk (e.g., ~120 Myr at 4 kpc and ~800 Myr at the disk edge; for more discussion see *Tonnesen and Stone* 2014). We also expect gravitational torques (i.e., self-gravity) to transport angular momentum. Thus, we expect some accretion of mass towards the galactic center even for `Isolated`. Moreover, since the magnetic field in the disk is strengthened for disks subjected to RPS (see middle panel of Figure 4.8), the increase in accretion for RPS runs compared to `Isolated` could be due to more efficient MRI.

The enhanced accretion of `NoCR` runs over those with CR, particularly over `DIF` runs, is potentially constraining of CR transport and calorimetry.

4.5.6 Radio Emission

RPS galaxies are observed to possess enhanced global radio emission, existing as outliers to the otherwise very tight FRC (*Murphy et al.*, 2009; *Vollmer et al.*, 2013). However, it is unclear if the excess compared to the FRC is due to stronger magnetic fields, elevated CR number densities $n_{\rm cr}$, or both. In Figure 4.8 we determine the relative contribution of these components to a synchrotron radio emission proxy ($n_{\rm cr}B^2$).

In the top panel of Figure 4.8 we see that RPS elevates the $n_{\rm cr}$ by a factor of a few for `ADV` runs and about one magnitude for `DIF` runs compared to their `Isolated` galaxy counterparts, likely related to RPS boosting the SFR (see Figure 4.6). We highlight that the lower $n_{\rm cr}$ for `DIF` compared to `ADV` must be due to the transport of CR out of the galactic disk, as more CR are injected for the `DIF` run (it has a higher SFR than `ADV`). Similarly, the boost in $n_{\rm cr}$ is very similar in the `FaceOn` and `EdgeOn` runs even though the boost in SFR is different, again suggesting transport dominates the $n_{\rm cr}$ evolution. Surprisingly, `ADV` has a smaller boost in $n_{\rm cr}$ despite having a larger boost in SFR than `DIF`for runs including RPS. This may suggest fewer CR are stripped in the `DIF` case. Clearly, exploring the boost in $n_{\rm cr}$ represents an interesting avenue for future research.

Yet the elevated radio emission in RPS galaxies is not only due to the elevated CR number density; in the middle panel of Figure 4.8 we see that the magnetic field strength is similarly boosted by a factor of a few. We also note that the magnetic field strength in the `NoCR`runs are boosted by a similar amount. It is somewhat surprising that the magnetic field strength is so similar for all runs with a wind, independent of CR transport or wind orientation. On the one hand, one would expect stronger magnetic field strengths for the `EdgeOn` runs as they exhibit higher SFRs (see top panel of Figure 4.6). On the other hand, compression of the disk magnetic field should be more effective for the `FaceOn` run, given the larger cross-sectional area of

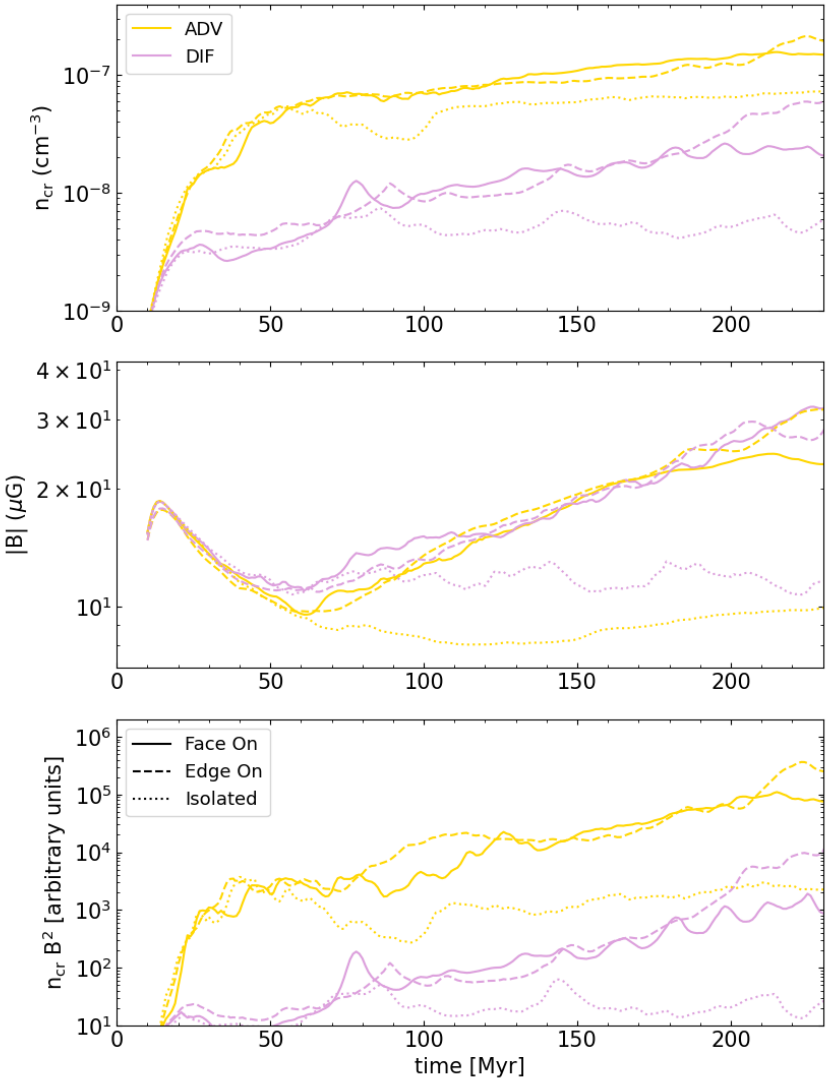

Figure 4.8: Time series profiles of cosmic ray number density (top), magnetic field strength (middle), and proxy for radio synchrotron (bottom). Gold (plum) curves indicate `ADV` (`DIF`) physics cases. Solid, dashed, and dotted curves indicate `FaceOn`, `EdgeOn`, and `Isolated` runs respectively. RPS both boosts —B— and $n_{\rm cr}$ by a factor of a few, producing a $\sim$2 magnitude boost in expected radio emission.

the galaxy presented to the ICM wind. We plan on disentangling these effects in future work.

However, since the synchrotron emission depends steeply on the magnetic field strength, the combined effect is a boost of two to three magnitudes, as seen in the bottom panel of Figure 4.8.

Clearly, CR transport plays a crucial role in driving the radio emission. We neglect more detailed analysis such as considering spatial maps of the radio emission with comparison to observations of local deficits observed by *Murphy et al.* (2009) as our CR model follows the protons whereas electrons generate the radio emission via synchrotron emission. Future work will use a spectral treatment of CR (*Yang and Ruszkowski*, 2017) to directly model the propagation and cooling of CR primary electrons, as well as the generation of secondaries.

4.5.7 Implications for Jellyfish Galaxies

Recent observations have discovered multiphase tails of stripped gas, extending up to ∼100 kpc from the disk (see *Poggianti et al.* 2017b). Detections of molecular gas and star formation (e.g., *Moretti et al.* 2018) in these tails are difficult to reconcile with theoretical work suggesting dense gas is not readily stripped (e.g., *Tonnesen and Bryan* 2012). Regardless of the removal, cold, molecular gas should be rapidly heated and mixed with the ambient hot ICM (*Cowie and McKee* 1977; *McKee and Cowie* 1977; *Balbus and McKee* 1982; *Stone and Norman* 1992; *Klein et al.* 1994; *Mac Low et al.* 1994; *Xu and Stone* 1995). In contrast, the presence of star formation suggests stripped gas not only survives but attains sufficient mass to induce gravitational collapse.

High resolution 3D cloud-crushing simulations suggest efficient radiative cooling enable clouds to not only survive but grow in mass (*Gronke and Oh*, 2018, 2020; *Sparre et al.*, 2020; *Li et al.*, 2020; *Kanjilal et al.*, 2021; *Abruzzo et al.*, 2021, Farber

& Gronke 2021). *Tonnesen and Bryan* (2021) study the survival of cold clouds in RPS tails, finding the fate of cold gas may depend on ICM properties. Even in the destruction regime, molecular material may form on short time scales when dust is present (*Girichidis et al.*, 2021).

We find that CR provide nonthermal pressure support for a diffuse molecular phase (see Figure 4.5). At later times when a galaxy encounters the higher density of cluster cores, it is likely this diffuse molecular gas will be stripped, even if dense molecular cores remain unperturbed. If blobs of diffuse molecular gas are sufficiently large to satisfy the Farber & Gronke criteria then these clouds may grow in mass and eventually become starforming. However, the impact of CR on cloud crushing remains relatively unexplored (see *Wiener et al.* 2017, 2019; *Brüggen and Scannapieco* 2020; *Bustard and Zweibel* 2021). In future work, we will explore these issues in greater depth.

4.6 Caveats and Future Work

Resolution. Our physical resolution of ∼127 pc is similar to that used in previous works including magnetic fields (*Tonnesen and Stone*, 2014; *Ruszkowski et al.*, 2014; *Ramos-Martínez et al.*, 2018). Although we include nonthermal physics and stellar feedback neglected by previous hydrodynamical studies, it is true such hydro studies were performed at high resolution (∼40 pc) limiting the ability to compare with our work. We plan on running higher resolution models in future work.

Box Size. Our relatively small box size $(\sim 64\ \mathrm{kpc})^3$ and resolution degrading from the galactic disk limits our ability to study the fate of stripped gas: do CR enable stripping of diffuse molecular material that can survive and compose observed molecular tails? Do CR couple with the stripped gas? How do observed radio tails constrain CR transport? We plan to investigate such stimulating problems in future work.

Wind Profile. We utilized a relatively simple model for the relative motion between our simulated galaxy and ICM. That is, we assume a fixed magnetic field strength, density and temperature. We do vary the wind velocity, modeling the galaxy falling from rest into the cluster; however, we have a constant wind for ∼150 Myr (for the ICM wind details, see §4.4.1). In reality, a galaxy falling into a cluster should sample a hotter, denser, and faster wind as it plunges towards the center of the cluster and diminishing thereafter. We note that the time we simulate the galaxy only traverses $\lesssim$ 0.3 Mpc. Thus, our galaxy samples cluster outskirts and our model is not implausible.

Neglected Physics. Cosmic rays are efficiently coupled to thermal plasma by scattering off waves they self-excite. The distribution of CR thus drifts with respect to the thermal plasma at the local Alfven velocity (*Kulsrud and Pearce*, 1969; *Zweibel*, 2017). However, wave damping processes such as ion-neutral friction (*Kulsrud and Cesarsky*, 1971; *Farber et al.*, 2018; *Bustard and Zweibel*, 2021), turbulent damping (*Farmer and Goldreich*, 2004; *Lazarian*, 2016; *Holguin et al.*, 2019), linear Landau damping (*Wiener et al.*, 2018) and nonlinear Landau damping (*Kulsrud*, 2005) enable CR to stream super-alfvenically and enable CR to heat the gas (mediated by the growth and subsequent damping of hydromagnetic waves).

Our neglect of CR streaming in addition to collisional loss processes (e.g., Coulomb and hadronic) will reduce the CR energy, transferring it to the thermal gas. However, our `NoCR` runs can effectively model CR losses proceeding very rapidly and thus comparison between the `NoCR`, `ADV`, and `DIF` simulations should bracket the inclusion of CR losses. The enhanced transport of CR away from the cold, dense mid-plane due to ion-neutral damping may help to reduce CR suppression of the centralized accretion flow we observe in our simulations, see Figure 4.7.

However, significant uncertainties in CR transport remain (*Hopkins et al.*, 2021). Recent work suggests CR may not completely decouple in the neutral medium (due to the "bottleneck" effect; *Wiener et al.* 2017, 2019; *Bustard and Zweibel* 2021) if pressure anisotropy can act as an efficient mechanism to grow hydromagnetic waves (*Zweibel*, 2020). Even in the absence of pressure anisotropy, dust grains may grow (or damp, depending on their transport relative to the Alven speed) hydromagnetic waves, even in molecular phases of low ionization fraction (*Squire et al.*, 2021). Exploring detailed models of (novel) cosmic-ray transport is beyond the scope of this work. Importantly, our results suggest CR transport can be effectively constrained in RPS studies, motivating future work on this topic.

We additionally ignore physics such as radiation pressure, anisotropic conduction, viscosity, and interactions with external galaxies as they are beyond the scope of this paper.

4.7 Conclusions

We performed the first cosmic-ray MHD simulations of an L_* cluster galaxy subjected to ram pressure stripping, including radiative cooling, self-gravity of the gas, star formation, and stellar feedback. Our main conclusions are summarized as follows.

1. Cosmic rays do not dramatically change the ram pressure stripping rate. This is true for the extreme cases of pure cosmic ray advection and diffusion without collisional losses and independent of the galaxy's inclination to the ICM wind. In all cases the stripping rates do not differ more than $\sim$15% in the 230 Myr of evolution we simulate.

2. The nonthermal pressure provided by cosmic rays permits a stable low temperature, low density phase, which persists even with ram pressure stripping. Since low density gas is typically preferentially stripped, the additional cosmic ray pressure likely supports this gas against ram pressure stripping. Interestingly, ram pressure stripping increases the amount of low-temperature gas in disks surviving both face-on and edge-on winds, particularly when cosmic rays are

included.

3. The observed *moderate* enhancement of star formation for cluster spirals undergoing ram pressure stripping places strong constraints on our models. Most of our simulations exhibit too large of a boost, attaining values $\sim$4-6 times greater for ram pressure stripped galaxies compared to isolated ones. We highlight that all of the `ADV` simulations over-enhance SFRs with respect to observations, while the `FaceOn-NoCR` and `FaceOn-DIF` models are in plausible agreement with the observed enhancement.

4. We find that cosmic rays suppress accretion of gas along the disk towards the midplane, even in isolated cases. Conversely, observations of cluster spirals indicating a high AGN fraction and bulge-dominated spirals (density-morphology relation) suggest enhanced gas accumulation in the nuclear region of galaxies undergoing ram pressure stripping. These observations appear to favor cosmic rays suffering rapid catastrophic losses or very efficient transport out of the disk. We suggest observations of ram pressure stripped galaxies may place novel constraints on cosmic-ray physics.

5. In agreement with radio observations, our galaxy models suggest ram pressure stripped galaxies boast enhanced radio emission compared to their counterparts in the field. We find magnetic field strengths boosted by a factor of a few, and cosmic ray number densities enhanced by a factor of ten for the diffusion model and by a factor of a few for the advection model. Cosmic ray transport thus may play a crucial role in understanding the enhanced radio emission above the far-infrared to radio correlation for cluster spirals.

4.8 True Diode Boundary Conditions

Diode boundary conditions allow material to flow out of the computational domain but are intended to prevent inflow. In FLASH, boundary conditions apply conditions to *cell-centered* values of ghost cells which border the physical computational domain. The default diode boundary condition implementation in FLASH simply replaces the velocity component component normal to the boundary with zero when it is negative. However, since the Riemann problem solves for the fluxes at cell *interfaces* to update hydrodynamic terms, even if the ghost cell-centered velocity is zero, an inflowing velocity at the ultimate interior cell (UIC) will result in an inflow accross the interface. This problem generically leads to non-conservation of mass when gravitational acceleration is present (as well as similar acceleration profiles).

Therefore, we apply the diode condition to the UIC cells, guaranteeing the flux across the physical domain boundary does not permit inflows. This simple, yet effective modification ensured conservation of mass. In our test, we initialized an 8^3 box with a static gas of uniform temperature $7 \times 10^7\,\mathrm{K}$ and density $10^{-27}\mathrm{g\ cm}^{-3}$. We turned off magnetic fields, cooling and heating, and star formation and feedback. However, we maintained the static potentials described in Section 4.4.1. In Figure 4.9 we show default (corrected) diode boundary conditions with solid blue (red dashed) curves, with the corrected diode boundary conditions indicating marked improvement.

We note that with large box sizes and higher resolution such that the acceleration at the UIC vanishes, non-conservation of mass also vanishes. Related to computational constraints, we were unable to perform our fiducial simulations in larger box sizes (except at lower resolution).

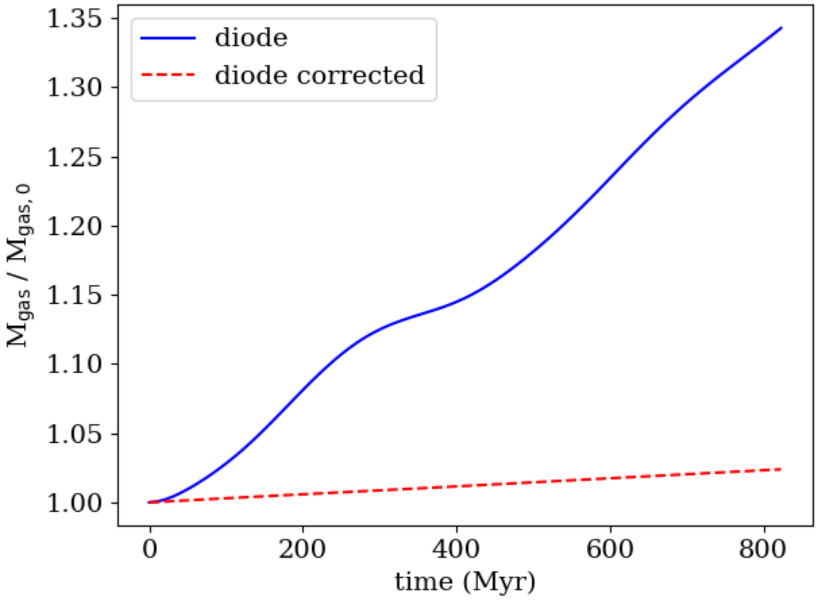

Figure 4.9: Conservation of mass with time. The solid blue (dashed red) curves indicate the default (corrected) diode boundary conditions. The corrected diode boundary conditions show marked improvement in mass conservation.

CHAPTER V

Summary and Conclusions

5.1 Thesis Results Summary

I have presented numerical investigations of galactic outflows covering scales from individual cold clouds in highly idealized setups of a hot wind, to patches of ISM with a full suite of cosmic ray and stellar feedback physics, to scales of full galactic disks, including isolated and cluster environments.

First, we considered the impact of cosmic ray transport at mesoscales, simulating a region with similar conditions to that of the Galactic Center in a tall box. Such ISM patch simulations permit significantly higher resolution than global disk models (e.g., compare *Farber et al.* 2018 to *Ruszkowski et al.* 2017) at a reasonable computational cost, particularly given the expense of MHD simulations including fast cosmic ray transport. I implemented cosmic ray decoupling from cool, neutral gas as a result of ion-neutral friction efficiently damping hydromagnetic waves as a boosted diffusion coefficient in cold gas. To ensure accurate temperature evolution, I implemented the *Townsend* (2009) exact integration scheme for radiative cooling.

The total compute volume of the simulations was 20 GB, all of which remains on external hard drives in my possession. The simulations required roughly 200 kW-hours to run, producing of order 0.1 metric tons CO_2[1].

---

[1] I approximate the electricity consumption to CO_2 generation based on the average CO_2 emitted

With these advancements over previous cosmic ray wind models, I determined that cosmic ray transport crucially modified the outflows. With faster transport from the cool, neutral midplane, cosmic rays more effectively accelerated the tenuous halo gas, establishing a wind. With the reduced cosmic ray pressure in the disk, star formation proceeded with a stronger burst, injecting more cosmic rays – this surprising positive feedback loop was shut off by the ensuing fast wind. Faster transport increased the cosmic ray number density present in the halo, possibly resulting in broader radio halos. Interestingly, even with fast cosmic ray transport, we found the outflow was composed of a fountain flow component and a wind component – future work including tracer particles can help to disentangle the kinematics of simultaneous outflows and inflows.

Second, we utilized highly idealized simulations of an individual cold cloud in a hot wind to determine how cold outflows are driven at the smallest scales. In contrast to previous work that focused on the survival criterion of $10^4\,\mathrm{K}$ clouds of ∼atomic hydrogen in a hot wind, we considered a range of cloud temperatures, focusing on $10^3\,\mathrm{K}$ and $400\,\mathrm{K}$ cold clumps representing molecular clouds. Moreover, we utilized tracer particles to perform the first study of dust survival in a galactic wind context.[2]

The total compute volume of our simulations was roughly ∼1 PB, of which 12 TB was retained (stored on an external hard drive) from the fiducial simulations. I estimate the energy required to produce simulations included in the paper totaled ∼120,000 kW-hours, generating ∼ 50 metric tons of CO_2.

In contrast with previous work of warmer clouds finding a binary result – either complete survival or destruction of the cold phase – we find that below the peak of the cooling time curve ∼8000 K, cold clouds exhibit three evolutionary outcomes: survival and growth of cold gas, destruction of the coldest phase but survival of the $\sim 10^4\,\mathrm{K}$ phase, or complete destruction of cold material via incorporation into the

---

per kW-hour of U.S. electricity generated: https://www.eia.gov/tools/faqs/faq.php?id=74&t=11.

[2] Studies of dust destruction in the high Mach supernova context are more prevalent.

hot wind. We determined analytic criteria that predict these outcomes, as well as a model utilizing instantaneous properties of the turbulent environment to predict the transition from mass loss to growth phases of surviving clouds. Even for clouds that survive, all their originally cold gas at some point mixes with the hot gas and heats up, which we found had important implications for the dust survival fraction.

One of our most enticing results was our finding that molecular clouds are accelerated much faster than the drag timescale expected for the acceleration of a *rigid* body by ram pressure. Since molecular clouds quickly develop an atomic phase 'cocooning' the molecular gas, mixing occurs in a two step process. The hot wind first mixes with the atomic phase which rapidly cools to $\sim 10^5$ K, as the mixed gas at 10^5 K cools rapidly, incorporating the momentum of the wind in the atomic phase. The resulting shear between the atomic and molecular phases mixes the two, bestowing the wind's momentum to the molecular phase (which survives as a distinct phase for sufficiently large clouds). As a result of the individual density contrasts between the hot and atomic & atomic phases ($\sim$100) and the atomic and molecular phases ($\sim$100) being much smaller than the initial density contrast between the hot wind and molecular cloud ($\sim 10^4$), acceleration takes place much faster than if mixing was suppressed, as may be the case if conduction can operate efficiently. However, turbulent mixing layer simulations suggest we are in the regime where mixing should dominate the heat transfer over conduction (*Tan et al.*, 2021). We emphasize that our work was exploratory in determining the temperature-dependence of the survival criterion and understanding the evolution of cold gas under idealized conditions. However, since uncertainties regarding the strength of conduction remain, we expect our results our robust, as studies of cold cloud evolution in a hot wind largely fit under the strong cooling regime of *Tan et al.* (2021)

The fast entrainment of cold clouds via mixing as opposed to direct ram pressure may help to explain observations of molecular outflows both in starburst and quasar systems (*Bolatto et al.*, 2013; *Ferrara and Scannapieco*, 2016) as well as in more quiescent systems (*Di Teodoro et al.*, 2019, 2020; *Su et al.*, 2021). Numerous extensions of this project will help to better understand the launching of galactic outflows at the smallest scales, discussed below.

Third, we studied the role cosmic rays play in modulating galactic properties in cluster environments. We performed one of the first ram pressure stripping models including both a magnetized disk (following the model of *Tonnesen and Stone* 2014) and a magnetized ICM (utilizing the parameters of *Ruszkowski et al.* 2017), and the first to model an L_* galaxy falling into a cluster with cosmic rays (cf. *Bustard et al.* 2020 for the case of a dwarf galaxy modeling the LMC falling into an L_* halo). We implemented an improved stellar feedback routine, incorporating the results of individual supernova remnants (*Martizzi et al.*, 2015) as a subgrid model. The *Martizzi et al.* (2015) subgrid model injects the appropriate amount of momentum and thermal energy based on local conditions to model the unresolved evolution of the Sedov-Taylor phase (cf. *Walch and Naab* 2015; *Iffrig and Hennebelle* 2015; *Kim and Ostriker* 2015). Progressing beyond collisional ionization equilibrium models, we implemented the *Gnedin and Kravtsov* (2011) method for accounting for photoionization heating and radiative cooling.

The total compute volume for the simulations appearing in the paper was ~ 4 TB, which is stored on an external hard drive. The simulations required ~14,000 kW-hours, producing roughly 6 metric tons of CO_2.

Note that the National Weather Service employs an 8 peta-flop cluster[3], similar in power to the initial 18 peta-flop Stampede2 cluster managed by the Texas Advanced Computing Center[4]. We estimate 10 million kW-hours are generated by the NWS per year to produce weather models, emitting ~4200 metric tons of CO_2. Thus, the CO_2 generated from the simulations performed for this thesis are negligible compared

---

[3] https://www.weather.gov/about/supercomputers

[4] https://portal.tacc.utexas.edu/user-guides/stampede2

to that produced by large institutions.

With these numerical improvements, we determined that cosmic rays play a similarly minor role in the ram pressure stripping process to magnetic fields. This is consistent with the simple *Gunn and Gott III* (1972) criterion for ram pressure stripping matching well with observations, despite neglecting nonthermal effects. Nevertheless, cosmic rays significantly modify the phase space of galaxies undergoing ram pressure, permitting low temperature, low density gas to exist that one otherwise expects to be stripped. We considered the moderate ram pressure environment typical of cluster outskirts, yet closer to cluster center with higher ICM density and relative galactic velocity, one may expect this tenuous molecular phase to be stripped. This may possibly explain the molecular gas tails in jellyfish galaxies undergoing extreme ram pressure. The molecular tails are mysterious as dense molecular clouds are not readily stripped (*Tonnesen and Bryan*, 2012).

Moreover, we find cosmic rays significantly suppress the accretion of material towards the galactic center possibly in tension with observations of bulge-dominated spirals in cluster environments (*Dressler*, 1980) and the high-AGN fraction (*Poggianti et al.*, 2017a). Either cosmic-ray coupling to the galactic disk is much weaker than we model (e.g., the transport is faster than we modeled due to ion-neutral damping) or cosmic rays are effectively thermalized by collisional or Coulomb losses close to their sources. We suggest future work utilizing ram pressure stripping observations may help to constrain cosmic-ray transport. Although our current work focuses on cluster outskirts such that we expect ram pressure to dominate galaxy evolution, we aim to explore the impact of galaxy-galaxy interactions in future work (which are expected to dominate the galactic evolution close to cluster cores).

The simulations and data analysis scripts used to generate the results of this thesis will be made available upon reasonable request.

5.2 Future Work

Although great strides have been taken in this thesis towards better understanding the launching of multiphase galactic outflows, many interesting avenues for a more complete understanding remain. Here we highlight a few projects again taking a multiscale approach: (1) the impact of cosmic rays on the acceleration of cold clouds in a hot wind, (2) ISM patch simulations using recent radio observations to constrain cosmic-ray transport, and (3) global galactic disk simulations including tracer particles to study the acceleration of cold gas with a statistically large sample, determining the fate of the cold gas, as well as studying the combination of wind, fountain flow, and accretion from the CGM to better understand the galactic baryon cycle of cosmic ray dominated halos.

Microphysics of Galactic Outflows. At the smallest scales of individual clouds, the impact of cosmic rays on the acceleration of cold clouds remains largely unexplored. This is despite the enticing results of low dimensional models (*Wiener et al.*, 2017, 2019; *Brüggen and Scannapieco*, 2020) suggesting cosmic rays may effectively accelerate cold clouds to high velocities. To our knowledge, *Bustard and Zweibel* (2021) remains the only three-dimensional study of cold cloud acceleration utilizing cosmic rays, which moreover includes the fast transport of cosmic rays due to ion-neutral damping. However, they neglected radiative cooling which was found to be crucial for cloud survival (at least for hydrodynamical studies).

The fast transport of cosmic rays plays a particularly challenging computational problem, as the regularization method to account for cosmic rays streaming down their pressure gradient (*Sharma et al.*, 2010), as well as typical methods to employ diffusion, restrict the timestep as the cell size squared. For example, at 1 pc resolution and for a typical Galactic diffusion coefficient $\kappa = 3 \times 10^{28} \mathrm{cm}^2\mathrm{s}^{-1}$, a stable timestep cannot exceed 1 yr. Such a small timestep is not feasible to advance simulations to ∼Myr. However, the recent development of "two-moment" methods (*Jiang and*

Oh, 2018; *Thomas and Pfrommer*, 2019) reduce the timestep restriction to a linear function of resolution (albeit with a reduced 'speed-of-light' maximum velocity).

Although still computationally expensive, high-resolution simulations of cosmic-ray cloud acceleration are on the horizon. Studies answering the following questions will significantly improve our understanding of the role of cosmic rays in driving galactic outflows: (i) how do cosmic rays modify the survival criteria for molecular clouds of *Farber and Gronke* (2021)? (ii) How significantly does pressure anisotropy, which provides coupling even in bottleneck regions, affect cosmic ray acceleration of cold clouds (*Zweibel*, 2020)? (iii) How do cosmic rays act synergistically with radiation pressure to drive outflows? Recent work has shown that charged dust grains can damp or excite Alfvén waves depending upon their Alfvén Mach number, which modifies cosmic ray transport (*Squire et al.*, 2021).

Even hydrodynamic simulations have significant room for improvement. Possible extensions to *Farber and Gronke* (2021) include: (a) *consideration of colder clouds.* The 10^3 K clouds studied in that work correspond more likely to a diffuse molecular phase. Consideration of star formation in galactic outflows will require cloud temperatures of order $\sim$10 K although the corresponding overdensities will be numerically challenging to simulate. Adaptive time-stepping may be crucial in allowing simulations to be computationally feasible. (b) *higher overdensities.* We considered a fixed overdensity of 10^3 whereas values of 10^{4-5} are necessary to consider mixing with the 10^7 K phase of galactic outflows and the 10^{7-8} K ICM. (c) *heating terms. Farber and Gronke* (2021) utilized cooling curves appropriate for collisional ionization equilibrium. However, the more diffuse medium is likely impacted by the strong UV environment of starbursts, resulting in photoionization heating. Additionally, the molecular phase should be heated and ionized by cosmic rays. Future work including a more rigorous treatement of heating and cooling will help to bridge the gap between basic physics studies and application to observed astronomical systems.

Mesophysics of Galactic Outflows. At the scale of ISM patch simulations, relatively high resolution cosmic ray studies remain possible for simulations of galactic dynamical timescales ∼200 Myr. While *Farber et al.* (2018) pioneered MHD galaxy evolution studies of cosmic ray transport dependent upon local plasma conditions, much progress has since been made. Yet despite recent progress, cosmic ray transport remains underconstrained. *Hopkins et al.* (2021) considered nearly three dozen models for cosmic ray transport, including wave damping and excitation according to the self-confinement and extrinsic turbulence paradigms. Utilizing *Fermi* γ-ray constraints, the theoretically best motivated models were ruled out. However, nearly a dozen models remained in satisfactory agreement with not only γ-ray constraints but also 'grammage' and residence time limits. Clearly, additional constraints on cosmic-ray transport are needed.

The CHANG-ES VLA survey of radio continuum halos around nearby edge-on spiral galaxies has recently determined an anti-correlation between the radio halo scale height and the gas surface density. ISM patch simulations provide the perfect scenario for sweeping the parameter space of gas surface densities. Moreover, FLASH simulations can include Lagrangian tracer particles or a spectral technique to directly track the cosmic ray electrons responsible for generating the radio emission via the synchrotron process (*Yang and Ruszkowski*, 2017). We plan to explore the ability of radio observations to constrain cosmic-ray transport in future work. When constraints provide a ∼unique description of cosmic-ray transport cosmic rays can be included in cosmological simulations. Such simulations will allow a statistical assessment of the importance cosmic rays play in galaxy formation and evolution as a function of redshift and galactic halo mass.

Macrophysics of Galactic Outflows. At the scale of full galactic disks, one can study not only the launching of galactic outflows but also the properties of the CGM at large. Global disk models have revealed that cosmic rays generically dominate the pressure in such halos (*Ji et al.*, 2020). However, detailed kinematics of the combination of outflows, fountain flows, and accretion from the CGM require tracer particles, not typically included in such simulations. Tracer particles will allow the study of the fate of a large number of individual cold clouds impacted by a galactic wind. Do cold clouds survive as predicted by *Farber and Gronke* (2021)? Or does the turbulence stirred by successive generations of supernovae render entrainment less viable than *in-situ* formation of molecular gas? What role do cosmic rays play in modulating the outflow properties – that is, do cosmic rays indirectly aid the acceleration of cold gas via their coupling to the ionized phase?

Clearly, the work is much and the workers are few. So let us puzzle and puzzle until our puzzlers are sore. For surely new generations will think of something we hadn't before.

Fine.

BIBLIOGRAPHY

BIBLIOGRAPHY

Abruzzo, M. W., G. L. Bryan, and D. B. Fielding (2021), A simple model for mixing and cooling in cloud-wind interactions, *arXiv preprint arXiv:2101.10344*.

Agertz, O., A. V. Kravtsov, S. N. Leitner, and N. Y. Gnedin (2013), Toward a complete accounting of energy and momentum from stellar feedback in galaxy formation simulations, *The Astrophysical Journal*, *770*(1), 25.

Anantharamaiah, K. R., and W. M. Goss (1996), Orthogonal rotating gaseous disks near the nucleus of ngc 253, *The Astrophysical Journal Letters*, *466*(1), 13.

Armillotta, L., F. Fraternali, and F. Marinacci (2016), Efficiency of gas cooling and accretion at the disc-corona interface, *MNRAS*, *462*, 4157–4170, doi: 10.1093/mnras/stw1930.

Armillotta, L., F. Fraternali, J. K. Werk, J. X. Prochaska, and F. Marinacci (2017), The survival of gas clouds in the circumgalactic medium of milky way-like galaxies, *Monthly Notices of the Royal Astronomical Society*, *470*, 114–125, doi:10.1093/mnras/stx1239.

Balbus, S. A., and J. F. Hawley (1991), A powerful local shear instability in weakly magnetized disks. i-linear analysis. ii-nonlinear evolution, *The Astrophysical Journal*, *376*, 214–233.

Balbus, S. A., and C. F. McKee (1982), The evaporation of spherical clouds in a hot gas. iii. suprathermal evaporation, *The Astrophysical Journal*, *252*, 529–552.

Banda-Barragán, W., E. Parkin, C. Federrath, R. Crocker, and G. Bicknell (2016), Filament formation in wind–cloud interactions–i. spherical clouds in uniform magnetic fields, *MNRAS*, *455*(2), 1309–1333.

Banda-Barragán, W., C. Federrath, R. Crocker, and G. Bicknell (2018), Filament formation in wind–cloud interactions–ii. clouds with turbulent density, velocity, and magnetic fields, *MNRAS*, *473*(3), 3454–3489.

Banda-Barragán, W. E., F. J. Zertuche, C. Federrath, J. García Del Valle, M. Brüggen, and A. Y. Wagner (2019), On the dynamics and survival of fractal clouds in galactic winds, *MNRAS*, *486*(4), 4526–4544.

Barger, K., N. Lehner, and J. C. Howk (2016), Down-the-barrel and transverse observations of the large magellanic cloud: evidence for a symmetric galactic wind on the near and far sides of the galaxy, *The Astrophysical Journal*, *817*(2), 91.

Barnes, J., and P. Hut (1986), A hierarchical o (n log n) force-calculation algorithm, *nature*, *324*(6096), 446–449.

Batchelor, C. K., and G. Batchelor (2000), *An introduction to fluid dynamics*, Cambridge university press.

Beck, R. (2001), Galactic and extragalactic magnetic fields, *Space Science Reviews*, *99*(1), 243–260.

Beck, R., and G. Golla (1988), Far-infrared and radio continuum emission of nearby galaxies, *Astronomy and Astrophysics*, *191*, L9–L12.

Begelman, M. C., and A. C. Fabian (1990), Turbulent mixing layers in the interstellar and intracluster medium., *MNRAS*, *244*, 26P–29.

Bekki, K. (2013), Galactic star formation enhanced and quenched by ram pressure in groups and clusters, *Monthly Notices of the Royal Astronomical Society*, *438*(1), 444–462.

Bell, E. F., D. H. Mcintosh, N. Katz, and M. D. Weinberg (2003), A first estimate of the baryonic mass function of galaxies, *The Astrophysical Journal*, *585*, 117–120.

Bellhouse, C., et al. (2019), Gasp. xv. a muse view of extreme ram-pressure stripping along the line of sight: physical properties of the jellyfish galaxy jo201, *MNRAS*, *485*(1), 1157–1170.

Berlok, T., and C. Pfrommer (2019), The impact of magnetic fields on cold streams feeding galaxies, *Monthly Notices of the Royal Astronomical Society*, *489*(3), 3368–3384, doi:10.1093/mnras/stz2347.

Bevan, A., M. J. Barlow, and D. Milisavljevic (2017), Dust masses for sn 1980k, sn1993j and cassiopeia a from red–blue emission line asymmetries, *Monthly Notices of the Royal Astronomical Society*, *465*, 4044–4056, doi:10.1093/mnras/stw2985.

Bigiel, F., et al. (2011), A constant molecular gas depletion time in nearby disk galaxies, *The Astrophysical Journal Letters*, *730*(2), L13.

Blandford, R., and D. Eichler (1987), Particle acceleration at astrophysical shocks: A theory of cosmic ray origin, *Physics Reports*, *154*(1), 1–75.

Bolatto, A. D., et al. (2013), Suppression of star formation in the galaxy ngc 253 by a starburst-driven molecular wind, *Nature*, *499*, 450–453, doi:10.1038/nature12351.

Bonnor, W. (1956), Boyle's law and gravitational instability, *MNRAS*, *116*, 351.

Booth, C., O. Agertz, A. V. Kravtsov, and N. Y. Gnedin (2013), Simulations of disk galaxies with cosmic ray driven galactic winds, *The Astrophysical Journal Letters*, *777*(1), L16.

Booth, C. M., J. Schaye, J. D. Delgado, and C. Dalla Vecchia (2012), The filling factor of intergalactic metals at redshift z= 3, *Monthly Notices of the Royal Astronomical Society*, *420*, 1053–1060, doi:10.1111/j.1365-2966.2011.20047.x.

Boselli, A., and G. Gavazzi (2006), Environmental effects on late-type galaxies in nearby clusters, *Publications of the Astronomical Society of the Pacific*, *118*(842), 517.

Boulares, A., and D. P. Cox (1990), Galactic hydrostatic equilibrium with magnetic tension and cosmic-ray diffusion, *The Astrophysical Journal*, *365*, 544–558.

Bregman, J. N., M. E. Anderson, M. J. Miller, E. Hodges-Kluck, X. Dai, J.-T. Li, Y. Li, and Z. Qu (2018), The extended distribution of baryons around galaxies, *The Astrophysical Journal*, *862*(1), 3.

Breitschwerdt, D., J. McKenzie, and H. Voelk (1991), Galactic winds. i-cosmic ray and wave-driven winds from the galaxy, *Astronomy and Astrophysics*, *245*, 79–98.

Breitschwerdt, D., J. McKenzie, and H. Völk (1993), Galactic winds. ii-role of the disk-halo interface in cosmic ray driven galactic winds, *Astronomy and Astrophysics*, *269*, 54–66.

Brook, C., et al. (2011), Hierarchical formation of bulgeless galaxies: why outflows have low angular momentum, *Monthly Notices of the Royal Astronomical Society*, *415*(2), 1051–1060.

Brooks, A. M., M. Kuhlen, A. Zolotov, and D. Hooper (2013), A baryonic solution to the missing satellites problem, *The Astrophysical Journal*, *765*(1), 22.

Brüggen, M., and E. Scannapieco (2016), The launching of cold clouds by galaxy outflows. ii. the role of thermal conduction, *The Astrophysical Journal*, *822*(1), 31.

Brüggen, M., and E. Scannapieco (2020), The launching of cold clouds by galaxy outflows. iv. cosmic-ray-driven acceleration, *The Astrophysical Journal*, *905*(1), 19.

Bryan, G. L., et al. (2014), Enzo: An adaptive mesh refinement code for astrophysics, *The Astrophysical Journal Supplement Series*, *211*(2), 19.

Burkert, A. (1995), The structure of dark matter halos in dwarf galaxies, *The Astrophysical Journal Letters*, *447*(1), L25.

Bustard, C., and E. G. Zweibel (2021), Cosmic-ray transport, energy loss, and influence in the multiphase interstellar medium, *ApJ*, *913*(2), 106.

Bustard, C., E. G. Zweibel, and E. D'Onghia (2016), A versatile family of galactic wind models, *The Astrophysical Journal*, *819*(1), 29.

Bustard, C., E. G. Zweibel, and C. Cotter (2017), Cosmic ray acceleration by a versatile family of galactic wind termination shocks, *The Astrophysical Journal*, *835*(1), 72.

Bustard, C., E. G. Zweibel, E. D'Onghia, J. Gallagher III, and R. Farber (2020), Cosmic-ray-driven outflows from the large magellanic cloud: contributions to the lmc filament, *The Astrophysical Journal*, *893*(1), 29.

Butcher, H., and A. Oemler Jr (1978), The evolution of galaxies in clusters. ii-the galaxy content of nearby clusters, *The Astrophysical Journal*, *226*, 559–565.

Butsky, I. S., and T. R. Quinn (2018), The role of cosmic-ray transport in shaping the simulated circumgalactic medium, *The Astrophysical Journal*, *868*(2), 108.

Butsky, I. S., D. B. Fielding, C. C. Hayward, C. B. Hummels, T. R. Quinn, and J. K. Werk (2020), The impact of cosmic rays on thermal instability in the circumgalactic medium, *ApJ*, *903*, 77.

Bykov, A. M. (2014), Nonthermal particles and photons in starburst regions and superbubbles, *The Astronomy and Astrophysics Review*, *22*(1), 77.

Caprioli, D. (2015), Cosmic-ray acceleration and propagation, *arXiv preprint arXiv:1510.07042*.

Cen, R., and J. P. Ostriker (1992), Galaxy formation and physical bias, *The Astrophysical Journal*, *399*, L113–L116.

Chan, T., D. Kereš, P. Hopkins, E. Quataert, K. Su, C. Hayward, and C. Faucher-Giguère (2019), Cosmic ray feedback in the fire simulations: constraining cosmic ray propagation with gev γ-ray emission, *Monthly Notices of the Royal Astronomical Society*, *488*(3), 3716–3744.

Chevalier, R. A., and A. W. Clegg (1985), Wind from a starburst galaxy nucleus, *Nature*, *317*, 44–45.

Cicone, C., M. Brusa, C. Ramos Almeida, G. Cresci, B. Husemann, and V. Mainieri (2018), The largely unconstrained multiphase nature of outflows in AGN host galaxies, *Nature Astronomy*, *2*(3), 176–178, doi:10.1038/s41550-018-0406-3.

Cicone, C., et al. (2014), Massive molecular outflows and evidence for AGN feedback from CO observations, *Astronomy & Astrophysics*, *562*, A21, doi:10.1051/0004-6361/201322464.

Collaboration, P., et al. (2020), Planck 2018 results. vi. cosmological parameters, *Astronomy & Astrophysics*.

Collaboration, P. A., et al. (2007), Correlation of the highest-energy cosmic rays with nearby extragalactic objects, *Science*, *318*(5852), 938–943.

Cortese, L., et al. (2007), The strong transformation of spiral galaxies infalling into massive clusters at z 0.2, *MNRAS*, *376*(1), 157–172.

Cortese, L., et al. (2010), Herschel-spire observations of the disturbed galaxy ngc 4438, *Astronomy & Astrophysics*, *518*, L63.

Cottle, J., E. Scannapieco, M. Brüggen, W. Banda-Barragán, and C. Federrath (2020), The launching of cold clouds by galaxy outflows. iii. the influence of magnetic fields, *The Astrophysical Journal*, *892*(1), 59.

Cottrell, G. A. (1977), 21-cm observations of the interacting galaxies m81 and m82, *Monthly Notices of the Royal Astronomical Society*, *178*(4), 577–589.

Cowie, L. L., and C. F. McKee (1977), The evaporation of spherical clouds in a hot gas. i. classical and saturated mass loss rates, *The Astrophysical Journal*, *211*, 135–146.

Cox, D. P. (2005), The three-phase interstellar medium revisited, *Annu. Rev. Astron. Astrophys.*, *43*, 337–385.

Cramer, W., J. Kenney, M. Sun, H. Crowl, M. Yagi, P. Jáchym, E. Roediger, and W. Waldron (2019), Spectacular hubble space telescope observations of the coma galaxy d100 and star formation in its ram pressure–stripped tail, *ApJ*, *870*(2), 63.

Croton, D. J., et al. (2006), The many lives of active galactic nuclei: cooling flows, black holes and the luminosities and colours of galaxies, *Monthly Notices of the Royal Astronomical Society*, *365*, 11–28.

Dai, X., J. N. Bregman, C. S. Kochanek, and E. Rasia (2010), On the baryon fractions in clusters and groups of galaxies, *The Astrophysical Journal*, *719*, 119.

Dalgarno, A., and R. A. McCray (1972), Heating and ionization of hi regions, *Annual review of astronomy and astrophysics*, *10*, 375.

de Grijs, R., R. W. O'Connell, G. D. Becker, R. A. Chevalier, and J. S. I. Gallagher (2000), Supernova remnants in the fossil starburst in m82, *AJ*, *119*, 681.

De Looze, I., M. J. Barlow, B. M. Swinyard, J. Rho, H. L. Gomez, M. Matsuura, and R. Wesson (2017), The dust mass in cassiopeia a from a spatially resolved herschel analysis, *Monthly Notices of the Royal Astronomical Society*, *465*, 3309–3342, doi: 10.1093/mnras/stw2837.

Dekel, A., and J. Silk (1986), The origin of dwarf galaxies, cold dark matter, and biased galaxy formation, *The Astrophysical Journal*, *303*, 39–55.

Di Teodoro, E. M., N. M. McClure-Griffiths, F. J. Lockman, S. R. Denbo, R. Endsley, H. A. Ford, and K. Harrington (2018), Blowing in the milky way wind: Neutral hydrogen clouds tracing the galactic nuclear outflow, *ApJ*, *855*, 33, doi:10.3847/1538-4357/aaad6a.

Di Teodoro, E. M., N. M. McClure-Griffiths, F. J. Lockman, and L. Armillotta (2020), Cold gas in the milky way's nuclear wind, *Nature*, *584*, 364–367.

Di Teodoro, E. M., et al. (2019), Molecular gas in the outflow of the small magellanic cloud, *The Astrophysical Journal Letters*, *885*, 32.

Dickey, J., and E. Salpeter (1984), 1.4 ghz continuum sources in the hercules cluster, *The Astrophysical Journal*, *284*, 461–470.

Diesing, R., and D. Caprioli (2018), Effect of cosmic rays on the evolution and momentum deposition of supernova remnants, *Physical review letters*, *121*(9), 091,101.

Draine, B. T. (2011), *Physics of the Interstellar and Intergalactic Medium*, Princeton University Press.

Dressler, A. (1980), Galaxy morphology in rich clusters-implications for the formation and evolution of galaxies, *The Astrophysical Journal*, *236*, 351–365.

Dubey, A., L. B. Reid, and R. Fisher (2008), Introduction to flash 3.0, with application to supersonic turbulence, *Physica Scripta*, *2008*, 14,046.

Dursi, L. J., and C. Pfrommer (2008), Draping of Cluster Magnetic Fields over Bullets and Bubbles—Morphology and Dynamic Effects, *ApJ*, *677*(2), 993–1018, doi:10.1086/529371.

Dutta, A., and P. Sharma (2019), On modelling cc85 wind in an expanding local box, *preprint*.

Dutta, A., P. Sharma, and D. Nelson (2021), Cooling flows around cold clouds in the circumgalactic medium: steady-state models & comparison with tng50, *arXiv preprint arXiv:2107.02722*.

Dwek, E., S. M. Foster, and O. Vancura (1996), Cooling, Sputtering, and Infrared Emission from Dust Grains in Fast Nonradiative Shocks, *ApJ*, *457*, 244, doi:10.1086/176725.

Ebert, R. (1955), Über die verdichtung von h i-gebieten, *Zeitschrift für Astrophysik*, *37*, 217.

Elmegreen, D. M., B. G. Elmegreen, F. R. Chromey, and M. S. Fine (2000), Dust streamers in the virgo galaxy m86 from ram pressure stripping of its companion vcc 882, *AJ*, *120*(2), 733.

Enßlin, T. A. (2003), On the escape of cosmic rays from radio galaxy cocoons, *Astronomy & Astrophysics*, *399*(2), 409–420.

Enßlin, T. A., C. Pfrommer, V. Springel, and M. Jubelgas (2007), Cosmic ray physics in calculations of cosmological structure formation, *Astronomy & Astrophysics*, *473*(1), 41–57.

Everett, J. E., and E. G. Zweibel (2011), The interaction of cosmic rays with diffuse clouds, *The Astrophysical Journal*, *739*(2), 60.

Everett, J. E., E. G. Zweibel, R. A. Benjamin, D. McCammon, L. Rocks, and J. S. Gallagher III (2008), The milky way's kiloparsec-scale wind: a hybrid cosmic-ray and thermally driven outflow, *The Astrophysical Journal*, *674*(1), 258.

Faerman, Y., A. Sternberg, and C. F. McKee (2020), Massive warm/hot galaxy coronae. ii. isentropic model, *The Astrophysical Journal*, *893*(1), 82.

Falle, S., C. Wareing, and J. Pittard (2020), Thermal instability revisited, *MNRAS*, *492*(3), 4484–4499.

Farber, R., M. Ruszkowski, H.-Y. Yang, and E. G. Zweibel (2018), Impact of cosmic-ray transport on galactic winds, *The Astrophysical Journal*, *856*, 112.

Farber, R. J., and M. Gronke (2021), The survival of multiphase dusty clouds in hot winds, *submitted to MNRAS*, *X*, X.

Farmer, A. J., and P. Goldreich (2004), Wave damping by magnetohydrodynamic turbulence and its effect on cosmic-ray propagation in the interstellar medium, *The Astrophysical Journal*, *604*(2), 671.

Faucher-Giguere, C.-A., A. Lidz, M. Zaldarriaga, and L. Hernquist (2009), A new calculation of the ionizing background spectrum and the effects of he ii reionization, *The Astrophysical Journal*, *703*(2), 1416.

Ferland, G., K. Korista, D. Verner, J. Ferguson, J. Kingdon, and E. Verner (1998), Cloudy 90: numerical simulation of plasmas and their spectra, *Publications of the Astronomical Society of the Pacific*, *110*(749), 761.

Ferland, G. J., R. Porter, P. Van Hoof, R. Williams, N. Abel, M. Lykins, G. Shaw, W. J. Henney, and P. Stancil (2013), The 2013 release of cloudy, *Revista mexicana de astronomía y astrofísica*, *49*(1), 137–163.

Ferrara, A., and E. Scannapieco (2016), ON THE FORMATION OF MOLECULAR CLUMPS IN QSO OUTFLOWS, *ApJ*, *833*(1), 46, doi:10.3847/1538-4357/833/1/46.

Field, G. B. (1965), Thermal instability., *ApJ*, *142*, 531.

Fielding, D. B., E. C. Ostriker, G. L. Bryan, and A. S. Jermyn (2020), Multiphase gas and the fractal nature of radiative turbulent mixing layers, *ApJ*, *894*(2), L24, doi:10.3847/2041-8213/ab8d2c.

Fischer, J., et al. (2010), *Herschel* -PACS spectroscopic diagnostics of local ULIRGs: Conditions and kinematics in Markarian 231, *A&A*, *518*, L41, doi:10.1051/0004-6361/201014676.

Fryxell, B., et al. (2000), Flash: An adaptive mesh hydrodynamics code for modeling astrophysical thermonuclear flashes, *The Astrophysical Journal Supplement Series*, *131*, 273–334, doi:10.1086/317361.

Galileo, G. (2016), *Sidereus Nuncius, or the sidereal messenger*, University of Chicgao Press.

Gallagher, R., R. Maiolino, F. Belfiore, N. Drory, R. Riffel, and R. A. Riffel (2019), Widespread star formation inside galactic outflows, *MNRAS*, *485*(3), 3409–3429.

Garrison-Kimmel, S., et al. (2019), Star formation histories of dwarf galaxies in the fire simulations: dependence on mass and local group environment, *Monthly Notices of the Royal Astronomical Society*, *489*(4), 4574–4588.

Genel, S., M. Vogelsberger, D. Nelson, D. Sijacki, V. Springel, and L. Hernquist (2013), Following the flow: Tracer particles in astrophysical fluid simulations, *MNRAS*, *435*, 1426–1442, doi:10.1093/mnras/stt1383.

Gentry, E. S., M. R. Krumholz, A. Dekel, and P. Madau (2017), Enhanced momentum feedback from clustered supernovae, *Monthly Notices of the Royal Astronomical Society*, *465*(2), 2471–2488.

Gentry, E. S., M. R. Krumholz, P. Madau, and A. Lupi (2019), The momentum budget of clustered supernova feedback in a 3d, magnetized medium, *Monthly Notices of the Royal Astronomical Society*, *483*(3), 3647–3658.

Girichidis, P., T. Naab, M. Hanasz, and S. Walch (2018), Cooler and smoother–the impact of cosmic rays on the phase structure of galactic outflows, *Monthly Notices of the Royal Astronomical Society*, *479*(3), 3042–3067.

Girichidis, P., T. Naab, S. Walch, and T. Berlok (2021), The in-situ formation of molecular and warm ionised gas triggered by hot outflows, *arXiv preprint arXiv:2101.08269*.

Girichidis, P., et al. (2016), Launching cosmic-ray-driven outflows from the magnetized interstellar medium, *The Astrophysical Journal Letters*, *816*(2), L19.

Gjergo, E., G. L. Granato, G. Murante, C. Ragone-Figueroa, L. Tornatore, and S. Borgani (2018), Dust evolution in galaxy cluster simulations, *MNRAS*, *479*(2), 2588–2606.

Gnedin, N. Y., and A. V. Kravtsov (2011), Environmental dependence of the kennicutt-schmidt relation in galaxies, *The Astrophysical Journal*, *728*(2), 88.

Grenier, I. A., J. H. Black, and A. W. Strong (2015), The nine lives of cosmic rays in galaxies, *Annual Review of Astronomy and Astrophysics*, *53*, 199–246.

Gronke, M., and S. P. Oh (2018), The growth and entrainment of cold gas in a hot wind, *Monthly Notices of the Royal Astronomical Society: Letters*, *480*, L111–L115.

Gronke, M., and S. P. Oh (2020), How cold gas continuously entrains mass and momentum from a hot wind, *Monthly Notices of the Royal Astronomical Society*, *492*, 1970–1990.

Grønnow, A., T. Tepper-García, and J. Bland-Hawthorn (2018), Magnetic fields in the galactic halo restrict fountain-driven recycling and accretion, *ApJ*, *865*(1), 64, doi:10.3847/1538-4357/aada0e.

Guedes, J., S. Callegari, P. Madau, and L. Mayer (2011), Forming realistic late-type spirals in a λcdm universe: the eris simulation, *The Astrophysical Journal*, *742*(2), 76.

Gunn, J. E., and J. R. Gott III (1972), On the infall of matter into clusters of galaxies and some effects on their evolution, *The Astrophysical Journal*, *176*, 1.

Guo, Q., S. White, C. Li, and M. Boylan-Kolchin (2010), How do galaxies populate dark matter haloes?, *Monthly Notices of the Royal Astronomical Society*, *404*(3), 1111–1120.

Hanasz, M., H. Lesch, T. Naab, A. Gawryszczak, K. Kowalik, and D. Wóltański (2013), Cosmic rays can drive strong outflows from gas-rich high-redshift disk galaxies, *The Astrophysical Journal Letters*, *777*(2), L38.

Hawley, J. F., and S. A. Balbus (1999), Transport in accretion disks, *Physics of Plasmas*, *6*(12), 4444–4449.

Heckman, T. M., M. Dahlem, M. D. Lehnert, G. Fabbiano, D. Gilmore, and W. H. Waller (1995), An X-Ray and Optical Study of the Dwarf Galaxy NGC 1569: Evidence for a Starburst-driven Outflow, *ApJ*, *448*, 98, doi:10.1086/175944.

Heintz, E., and E. G. Zweibel (2018), The parker instability with cosmic-ray streaming, *The Astrophysical Journal*, *860*(2), 97.

Hennebelle, P., and M. Pérault (1999), Dynamical condensation in a thermally bistable flow. application to interstellar cirrus, *A&A*, *351*, 309–322.

Hernquist, L. (1993), N-body realizations of compound galaxies, *The Astrophysical Journal Supplement Series*, *86*, 389–400.

Hess, V. F. (1912), Uber beobachtungen der durchdringenden strahlung bei sieben freiballonfahrten, *Phys. Zeits.*, *13*, 1084–1091.

Hill, A. S., M. R. Joung, M.-M. Mac Low, R. A. Benjamin, L. M. Haffner, C. Klingenberg, and K. Waagan (2012), Vertical structure of a supernova-driven turbulent, magnetized interstellar medium, *The Astrophysical Journal*, *750*(2), 104.

Hillas, A. M. (1984), The origin of ultra-high-energy cosmic rays, *Annual review of astronomy and astrophysics*, *22*(1), 425–444.

Holguin, F., M. Ruszkowski, A. Lazarian, R. Farber, and H. K. Yang (2019), Role of cosmic-ray streaming and turbulent damping in driving galactic winds, *Monthly Notices of the Royal Astronomical Society*, *490*(1), 1271–1282.

Hollenbach, D., and C. F. McKee (1979), Molecule formation and infrared emission in fast interstellar shocks. i. physical processes*, *The Astrophysical Journal Supplement Series*, *41*, 555–592.

Hopkins, P. F., T. Chan, S. Garrison-Kimmel, S. Ji, K.-Y. Su, C. B. Hummels, D. Kereš, E. Quataert, and C.-A. Faucher-Giguère (2020), But what about...: cosmic rays, magnetic fields, conduction, and viscosity in galaxy formation, *Monthly Notices of the Royal Astronomical Society*, *492*(3), 3465–3498.

Hopkins, P. F., J. Squire, T. Chan, E. Quataert, S. Ji, D. Kereš, and C.-A. Faucher-Giguère (2021), Testing physical models for cosmic ray transport coefficients on galactic scales: self-confinement and extrinsic turbulence at gev energies, *Monthly Notices of the Royal Astronomical Society*, *501*(3), 4184–4213.

Huang, J., and L. Greengard (1999), A fast direct solver for elliptic partial differential equations on adaptively refined meshes, *SIAM Journal on Scientific Computing*, *21*(4), 1551–1566.

Huang, X., S. W. Davis, and D. Zhang (2020), Dusty cloud acceleration with multiband radiation, *The Astrophysical Journal*, *893*(1), 50.

Hubble, E., and M. L. Humason (1931), The velocity-distance relation among extragalactic nebulae, *The Astrophysical Journal*, *74*, 43.

Hubble, E. P. (1929a), A relation between distance and radial velocity among extragalactic nebulae, *Proceedings of the National Academy of Sciences of the United States of America*, *15*, 168–173, doi:10.1073/pnas.15.3.168.

Hubble, E. P. (1929b), A spiral nebula as a stellar system, messier 31, *The Astrophysical Journal*, *69*.

Hughes, D. H., et al. (1998), High-redshift star formation in the hubble deep field revealed by a submillimetre-wavelength survey, *Nature*, *394*, 241–247, doi:10.1038/28328.

Iffrig, O., and P. Hennebelle (2015), Mutual influence of supernovae and molecular clouds, *Astronomy & Astrophysics*, *576*, A95.

Ipavich, F. M. (1975), Galactic winds driven by cosmic rays, *The Astrophysical Journal*, *196*, 107–120.

Irwin, J., et al. (2019), Chang-es: Xviii—the chang-es survey and selected results, *Galaxies*, *7*(1), 42.

Jáchym, P., J. Köppen, J. Palouš, and F. Combes (2009), Ram pressure stripping of tilted galaxies, *Astronomy & Astrophysics*, *500*(2), 693–703.

Jáchym, P., M. Sun, J. D. Kenney, L. Cortese, F. Combes, M. Yagi, M. Yoshida, J. Palouš, and E. Roediger (2017), Molecular gas dominated 50 kpc ram pressure stripped tail of the coma galaxy d100, *ApJ*, *839*(2), 114.

Jáchym, P., et al. (2019), Alma unveils widespread molecular gas clumps in the ram pressure stripped tail of the norma jellyfish galaxy, *ApJ*, *883*(2), 145.

Jacob, S., R. Pakmor, C. M. Simpson, V. Springel, and C. Pfrommer (2018), The dependence of cosmic ray-driven galactic winds on halo mass, *Monthly Notices of the Royal Astronomical Society*, *475*(1), 570–584.

Jaffé, Y. L., R. Smith, G. N. Candlish, B. M. Poggianti, Y.-K. Sheen, and M. A. Verheijen (2015), Budhies ii: a phase-space view of h i gas stripping and star formation quenching in cluster galaxies, *Monthly Notices of the Royal Astronomical Society*, *448*(2), 1715–1728.

Jennings, R. M., and Y. Li (2020), Thermal instability and multiphase gas in the simulated interstellar medium with conduction, viscosity and magnetic fields, *preprint*.

Ji, S., S. P. Oh, and M. McCourt (2018), The impact of magnetic fields on thermal instability, *MNRAS*, *476*, 852–867.

Ji, S., T. Chan, C. B. Hummels, P. F. Hopkins, J. Stern, D. Kereš, E. Quataert, C.-A. Faucher-Giguère, and N. Murray (2020), Properties of the circumgalactic medium in cosmic ray-dominated galaxy haloes, *Monthly Notices of the Royal Astronomical Society*, *496*(4), 4221–4238.

Jiang, Y.-F., and S. P. Oh (2018), A new numerical scheme for cosmic-ray transport, *The Astrophysical Journal*, *854*(1), 5.

Jóhannesson, G., et al. (2016), Bayesian analysis of cosmic ray propagation: evidence against homogeneous diffusion, *The Astrophysical Journal*, *824*(1), 16.

Jubelgas, M., V. Springel, T. Enßlin, and C. Pfrommer (2008), Cosmic ray feedback in hydrodynamical simulations of galaxy formation, *Astronomy & Astrophysics*, *481*(1), 33–63.

Kanjilal, V., A. Dutta, and P. Sharma (2021), Growth and structure of multiphase gas in the cloud-crushing problem with cooling, *Monthly Notices of the Royal Astronomical Society*, *501*, 1143–1159.

Katz, N., D. H. Weinberg, L. Hernquist, and J. Miralda-Escude (1996), Damped lyman-alpha and lyman-limit absorbers in the cold dark matter model, *The Astrophysical Journal Letters*, *457*(2), L57.

Kempski, P., and E. Quataert (2020), Thermal instability of halo gas heated by streaming cosmic rays, *MNRAS*, *493*, 1801–1817.

Kennicutt Jr, R. C. (1998), The global schmidt law in star-forming galaxies, *The Astrophysical Journal*, *498*(2), 541.

Kim, C.-G., and E. C. Ostriker (2015), Momentum injection by supernovae in the interstellar medium, *The Astrophysical Journal*, *802*(2), 99.

Kirchschlager, F., F. D. Schmidt, M. J. Barlow, E. L. Fogerty, A. Bevan, and F. D. Priestley (2019), Dust survival rates in clumps passing through the cas a reverse shock-i. results for a range of clump densities, *MNRAS*, *489*, 4465–4496, doi:10.1093/mnras/stz2399.

Klein, R. I., C. F. McKee, and P. Colella (1994), On the hydrodynamic interaction of shock waves with interstellar clouds. 1: Nonradiative shocks in small clouds, *The Astrophysical Journal*, *420*, 213–236.

Klypin, A., A. V. Kravtsov, O. Valenzuela, and F. Prada (1999), Where are the missing galactic satellites?, *The Astrophysical Journal*, *522*(1), 82.

Kravtsov, A. (1999), Phd thesis, Ph.D. thesis, New Mexico State Univ.

Kravtsov, A. V., A. Klypin, and Y. Hoffman (2002), Constrained simulations of the real universe. ii. observational signatures of intergalactic gas in the local supercluster region, *The Astrophysical Journal*, *571*(2), 563.

Kronberger, T., W. Kapferer, C. Ferrari, S. Unterguggenberger, and S. Schindler (2008), On the influence of ram-pressure stripping on the star formation of simulated spiral galaxies, *Astronomy & Astrophysics*, *481*(2), 337–343.

Kroupa, P. (2001), On the variation of the initial mass function, *Monthly Notices of the Royal Astronomical Society*, *322*(2), 231–246.

Krumholz, M. R. (2012), Star Formation in Atomic Gas, *ApJ*, *759*(1), 9, doi:10.1088/0004-637X/759/1/9.

Krumholz, M. R., and J. C. Tan (2007), Slow star formation in dense gas: evidence and implications, *The Astrophysical Journal*, *654*(1), 304.

Kulsrud, R., and C. Cesarsky (1971), The effectiveness of instabilities for the confinement of high energy cosmic rays in the galactic disk, *Astrophysical Letters*, *8*, 189.

Kulsrud, R., and W. P. Pearce (1969), The effect of wave-particle interactions on the propagation of cosmic rays, *The Astrophysical Journal*, *156*, 445.

Kulsrud, R. M. (2005), *Plasma Physics for Astrophysics*, Princeton University Press.

Kupilas, M., C. Wareing, J. Pittard, and S. Falle (2021), Interactions of a shock with a molecular cloud at various stages of its evolution due to thermal instability and gravity, *MNRAS*, *501*(3), 3137–3154.

Lacki, B. C., T. A. Thompson, and E. Quataert (2010), The physics of the far-infrared-radio correlation. i. calorimetry, conspiracy, and implications, *The Astrophysical Journal*, *717*, 1.

Laporte, N., R. S. Ellis, F. Boone, F. E. Bauer, D. Quénard, G. Roberts-Borsani, R. Pelló, I. Pérez-Fournon, and A. Streblyanska (2017), Dust in the reionization era: Alma observations of a z =8.38 gravitationally-lensed galaxy, *arXiv*, *837*, L21, doi:10.3847/2041-8213/aa62aa.

Larson, R. B. (1974), Effects of supernovae on the early evolution of galaxies, *Monthly Notices of the Royal Astronomical Society*, *169*, 229–245.

Lazarian, A. (2016), Damping of alfvén waves by turbulence and its consequences: From cosmic-ray streaming to launching winds, *The Astrophysical Journal*, *833*(2), 131.

Lee, B., A. Chung, S. Tonnesen, J. D. Kenney, O. I. Wong, B. Vollmer, G. R. Petitpas, H. H. Crowl, and J. van Gorkom (2017), The effect of ram pressure on the molecular gas of galaxies: three case studies in the virgo cluster, *MNRAS*, *466*(2), 1382–1398.

Lee, D. (2013), A solution accurate, efficient and stable unsplit staggered mesh scheme for three dimensional magnetohydrodynamics, *Journal of Computational Physics*, *243*, 269–292, doi:10.1016/j.jcp.2013.02.049.

Lee, D., and A. E. Deane (2009), An unsplit staggered mesh scheme for multidimensional magnetohydrodynamics, *Journal of Computational Physics*, *228*, doi:10.1016/j.jcp.2008.08.026.

Lee, J., T. Kimm, H. Katz, J. Rosdahl, J. Devriendt, and A. Slyz (2020), Dual effects of ram pressure on star formation in multiphase disk galaxies with strong stellar feedback, *The Astrophysical Journal*, *905*(1), 31.

Lehnert, M. D., and T. M. Heckman (1996), Ionized gas in the halos of edge-on starburst galaxies: evidence for supernova-driven superwinds, *The Astrophysical Journal*, *462*, 651.

Leroy, A. K., et al. (2015), The multi-phase cold fountain in m82 revealed by a wide, sensitive map of the molecular interstellar medium, *The Astrophysical Journal*, *814*, 83.

Leroy, A. K., et al. (2017), Cloud-scale ism structure and star formation in m51, *The Astrophysical Journal*, *846*(1), 71.

Li, M., and G. L. Bryan (2020), Simple yet powerful: Hot galactic outflows driven by supernovae, *The Astrophysical Journal Letters*, *890*(2), L30.

Li, Y., G. L. Bryan, M. Ruszkowski, G. M. Voit, B. W. O'Shea, and M. Donahue (2015), Cooling, agn feedback, and star formation in simulated cool-core galaxy clusters, *The Astrophysical Journal*, *811*(2), 73.

Li, Z., P. F. Hopkins, J. Squire, and C. Hummels (2020), On the survival of cool clouds in the circumgalactic medium, *Monthly Notices of the Royal Astronomical Society*, *492*, 1841–1854, doi:10.1093/mnras/stz3567.

Lochhaas, C., T. A. Thompson, and E. E. Schneider (2021), The characteristic momentum of radiatively cooling energy-driven galactic winds, *Monthly Notices of the Royal Astronomical Society*, *504*(3), 3412–3423.

Lockman, F. J., E. M. Di Teodoro, and N. McClure-Griffiths (2020), Observation of acceleration of h i clouds within the fermi bubbles, *ApJ*, *888*(1), 51.

López-Barquero, V., R. Farber, S. Xu, P. Desiati, and A. Lazarian (2016), Cosmic-ray small-scale anisotropies and local turbulent magnetic fields, *The Astrophysical Journal*, *830*(1), 19.

Lynds, C. (1961), Radio observations of the peculiar galaxy m82., *The Astrophysical Journal*, *134*, 659–661.

Lynds, C. R., and A. R. Sandage (1963), Evidence for an explosion in the center of the galaxy m82., *The Astrophysical Journal*, *137*, 1005.

Lyutikov, M. (2006), Magnetic draping of merging cores and radio bubbles in clusters of galaxies, *Monthly Notices of the Royal Astronomical Society*, *373*(1), 73–78.

Mac Low, M.-M., and A. Ferrara (1999), Starburst-driven mass loss from dwarf galaxies: efficiency and metal ejection, *The Astrophysical Journal*, *513*, 142.

Mac Low, M.-M., C. F. McKee, R. I. Klein, J. M. Stone, and M. L. Norman (1994), Shock interactions with magnetized interstellar clouds. 1: Steady shocks hitting nonradiative clouds, *The Astrophysical Journal*, *433*, 757–777.

Maiolino, R., et al. (2017), Star formation inside a galactic outflow, *Nature*, *544*(7649), 202–206.

Mandelker, N., D. Nagai, H. Aung, A. Dekel, Y. Birnboim, and F. C. van den Bosch (2020), Instability of supersonic cold streams feeding galaxies – IV. Survival of radiatively cooling streams, *Monthly Notices of the Royal Astronomical Society*, *494*(2), 2641–2663, doi:10.1093/mnras/staa812.

Marinacci, F., J. Binney, F. Fraternali, C. Nipoti, L. Ciotti, and P. Londrillo (2010), The mode of gas accretion on to star-forming galaxies, *Monthly Notices of the Royal Astronomical Society*, *404*, 1464–1474.

Martin, C. L. (2005), Mapping Large-Scale Gaseous Outflows in Ultraluminous Galaxies with Keck II ESI Spectra: Variations in Outflow Velocity with Galactic Mass, *The Astrophysical Journal*, *621*(1), 227–245, doi:10.1086/427277.

Martizzi, D., C.-A. Faucher-Giguère, and E. Quataert (2015), Supernova feedback in an inhomogeneous interstellar medium, *Monthly Notices of the Royal Astronomical Society*, *450*(1), 504–522.

Martizzi, D., D. Fielding, C.-A. Faucher-Giguère, and E. Quataert (2016), Supernova feedback in a local vertically stratified medium: interstellar turbulence and galactic winds, *MNRAS*, *459*(3), 2311–2326.

McClure-Griffiths, N. M., J. A. Green, A. S. Hill, F. J. Lockman, J. M. Dickey, B. M. Gaensler, and A. J. Green (2013), Atomic hydrogen in a galactic center outflow, *ApJ*, *770*, L4, doi:10.1088/2041-8205/770/1/L4.

McClure-Griffiths, N. M., H. Dénes, J. Dickey, et al. (2018), Cold gas outflows from the small magellanic cloud traced with askap, *Nature*, *2*, 901–906.

McCourt, M., P. Sharma, E. Quataert, and I. J. Parrish (2012), Thermal instability in gravitationally stratified plasmas: implications for multiphase structure in clusters and galaxy haloes, *Monthly Notices of the Royal Astronomical Society*, *419*, 3319–3337.

McCourt, M., R. M. O'Leary, A.-M. Madigan, and E. Quataert (2015), Magnetized gas clouds can survive acceleration by a hot wind, *Monthly Notices of the Royal Astronomical Society*, *449*, 2–7.

McCourt, M., S. P. Oh, R. O'Leary, and A.-M. Madigan (2018), A characteristic scale for cold gas, *Monthly Notices of the Royal Astronomical Society*, *473*, 5407–5431.

McKee, C. F., and L. L. Cowie (1977), The evaporation of spherical clouds in a hot gas. ii-effects of radiation, *The Astrophysical Journal*, *215*, 213–225.

McKee, C. F., and E. C. Ostriker (2007), Theory of star formation, *Annu. Rev. Astron. Astrophys.*, *45*, 565–687.

Melioli, C., E. de Gouveia Dal Pino, and F. Geraissate (2013), Evolution of m82-like starburst winds revisited: 3d radiative cooling hydrodynamical simulations, *Monthly Notices of the Royal Astronomical Society*, *430*(4), 3235–3248.

Miyamoto, M., and R. Nagai (1975), Three-dimensional models for the distribution of mass in galaxies, *Publications of the Astronomical Society of Japan*, *27*, 533–543.

Moretti, A., et al. (2018), Gasp–x. apex observations of molecular gas in the discs and in the tails of ram-pressure stripped galaxies, *MNRAS*, *480*(2), 2508–2520.

Moretti, A., et al. (2020a), Gasp. xxii. the molecular gas content of the jw100 jellyfish galaxy at z 0.05: Does ram pressure promote molecular gas formation?, *The Astrophysical Journal*, *889*(1), 9.

Moretti, A., et al. (2020b), The high molecular gas content, and the efficient conversion of neutral into molecular gas, in jellyfish galaxies, *The Astrophysical Journal Letters*, *897*(2), L30.

Moss, D., and D. Sokoloff (2017), Galactic winds and the origin of large-scale magnetic fields, *Astronomy & Astrophysics*, *598*, A72.

Moster, B. P., R. S. Somerville, C. Maulbetsch, F. C. V. D. Bosch, A. V. Macció, T. Naab, and L. Oser (2010), Galactic winds and the origin of large-scale magnetic fields, *ApJ*, *710*, 903.

Müller, A., et al. (2021), Highly ordered magnetic fields in the tail of the jellyfish galaxy jo206, *Nature Astronomy*, *5*(2), 159–168.

Murphy, E. J., J. D. P. Kenney, G. Helou, A. Chung, and J. H. Howell (2009), Environmental effects in clusters: Modified far-infrared-radio relations within virgo cluster galaxies, *The Astrophysical Journal*, *694*, 1435.

Murray, N., B. Ménard, and T. A. Thompson (2011), Radiation pressure from massive star clusters as a launching mechanism for super-galactic winds, *The Astrophysical Journal*, *735*(1), 66.

Ménard, B., R. Scranton, M. Fukugita, and G. Richards (2010), Measuring the galaxy–mass and galaxy–dust correlations through magnification and reddening, *Monthly Notices of the Royal Astronomical Society*, *405*, 1025–1039.

Nagashima, K., K. Fujimoto, and R. Jacklyn (1998), Galactic and heliotail-in anisotropies of cosmic rays as the origin of sidereal daily variation in the energy region¡ 104 gev, *Journal of Geophysical Research: Space Physics*, *103*(A8), 17,429–17,440.

Nava, L., and S. Gabici (2013), Anisotropic cosmic ray diffusion and gamma-ray production close to supernova remnants, with an application to w28, *Monthly Notices of the Royal Astronomical Society*, *429*(2), 1643–1651.

Navarro, J. F., C. S. Frenk, and S. D. White (1997), A universal density profile from hierarchical clustering, *The Astrophysical Journal*, *490*(2), 493.

Oosterloo, T., and J. van Gorkom (2005), A large h i cloud near the centre of the virgo cluster, *Astronomy & Astrophysics*, *437*(1), L19–L22.

Pacini, D. (1912), *La radiazione penetrante alla superficie ed in seno alle acque*, Stab. tip. Toscano.

Paglione, T. A., and R. D. Abrahams (2012), Properties of nearby starburst galaxies based on their diffuse gamma-ray emission, *The Astrophysical Journal*, *755*(2), 106.

Pakmor, R., C. Pfrommer, C. M. Simpson, R. Kannan, and V. Springel (2016a), Semi-implicit anisotropic cosmic ray transport on an unstructured moving mesh, *Monthly Notices of the Royal Astronomical Society*, *462*(3), 2603–2616.

Pakmor, R., C. Pfrommer, C. M. Simpson, and V. Springel (2016b), Galactic winds driven by isotropic and anisotropic cosmic-ray diffusion in disk galaxies, *The Astrophysical Journal Letters*, *824*(2), L30.

Paladino, R., M. Murgia, T. T. Helfer, T. Wong, R. Ekers, L. Blitz, L. Gregorini, and L. Moscadelli (2006), Thermal and non-thermal components of the interstellar medium at sub-kiloparsec scales in galaxies, *Astronomy and Astrophysics*, *456*, 847–859.

Peek, J. E. G., B. Ménard, and L. Corrales (2015), DUST IN THE CIRCUMGALACTIC MEDIUM OF LOW-REDSHIFT GALAXIES, *ApJ*, *813*(1), 7, doi:10.1088/0004-637X/813/1/7.

Peeples, M. S., J. K. Werk, J. Tumlinson, B. D. Oppenheimer, J. X. Prochaska, N. Katz, and D. H. Weinberg (2014), A budget and accounting of metals at z 0: results from the cos-halos survey, *The Astrophysical Journal*, *786*(1), 54.

Peters, T., et al. (2015), Impact of supernova and cosmic-ray driving on the surface brightness of the galactic halo in soft x-rays, *The Astrophysical Journal Letters*, *813*(2), L27.

Pfrommer, C., and J. Dursi (2010), Detecting the orientation of magnetic fields in galaxy clusters, *Nature Physics*, *6*(7), 520–526.

Pfrommer, C., R. Pakmor, K. Schaal, C. Simpson, and V. Springel (2017a), Simulating cosmic ray physics on a moving mesh, *Monthly Notices of the Royal Astronomical Society*, *465*(4), 4500–4529.

Pfrommer, C., R. Pakmor, C. M. Simpson, and V. Springel (2017b), Simulating gamma-ray emission in star-forming galaxies, *The Astrophysical Journal Letters*, *847*(2), L13.

Pietrzyński, G., et al. (2013), An eclipsing-binary distance to the large magellanic cloud accurate to two per cent, *Nature*, *495*(7439), 76–79.

Poggianti, B. M., et al. (2017a), Ram-pressure feeding of supermassive black holes, *Nature*, *548*(7667), 304–309.

Poggianti, B. M., et al. (2017b), Gasp. i. gas stripping phenomena in galaxies with muse, *The Astrophysical Journal*, *844*(1), 48.

Priestley, F., H. Chawner, M. Matsuura, I. De Looze, M. Barlow, and H. Gomez (2021), Revisiting the dust destruction efficiency of supernovae, *Monthly Notices of the Royal Astronomical Society*, *500*(2), 2543–2553.

Priestley, F. D., M. J. Barlow, and I. De Looze (2019), The mass, location, and heating of the dust in the cassiopeia a supernova remnant, *Monthly Notices of the Royal Astronomical Society*, *485*, 440–451, doi:10.1093/mnras/stz414.

Ptuskin, V. (2006), Cosmic ray transport in the galaxy, in *J. Phys. Conf. Ser*, vol. 47, pp. 113–119.

Ptuskin, V., H. Völk, V. Zirakashvili, and D. Breitschwerdt (1997), Transport of relativistic nucleons in a galactic wind driven by cosmic rays., *Astronomy and Astrophysics*, *321*, 434–443.

Qu, Z., and J. N. Bregman (2018a), The mass and absorption columns of galactic gaseous halos, *The Astrophysical Journal*, *856*(1), 5.

Qu, Z., and J. N. Bregman (2018b), The mass and absorption column densities of galactic gaseous halos. ii. the high ionization state ions, *The Astrophysical Journal*, *862*(1), 23.

Qu, Z., and J. N. Bregman (2019), The warm gaseous disk and the anisotropic circumgalactic medium of the milky way, *The Astrophysical Journal*, *880*(2), 89.

Radovich, M., B. Poggianti, Y. L. Jaffé, A. Moretti, D. Bettoni, M. Gullieuszik, B. Vulcani, and J. Fritz (2019), Gasp–xix. agn and their outflows at the centre of jellyfish galaxies, *Monthly Notices of the Royal Astronomical Society*, *486*(1), 486–503.

Ramos-Martínez, M., G. C. Gómez, and Á. Pérez-Villegas (2018), Mhd simulations of ram pressure stripping of a disc galaxy, *Monthly Notices of the Royal Astronomical Society*, *476*(3), 3781–3792.

Raymond, J. C., D. P. Cox, and B. W. Smith (1976), Radiative cooling of a low-density plasma, *The Astrophysical Journal*, *204*, 290–292.

Rekola, R., M. G. Richer, M. L. McCall, M. J. Valtonen, J. K. Kotilainen, and C. Flynn (2005), Distance to NGC 253 based on the planetary nebula luminosity function, *Monthly Notices of the Royal Astronomical Society*, *361*(1), 330–336, doi: 10.1111/j.1365-2966.2005.09166.x.

Reynolds, R., L. Haffner, and S. Tufte (1999), Evidence for an additional heat source in the warm ionized medium of galaxies, *The Astrophysical Journal Letters*, *525*(1), L21.

Ricker, P. (2008), A direct multigrid poisson solver for oct-tree adaptive meshes, *The Astrophysical Journal Supplement Series*, *176*(1), 293.

Robertson, B. E., A. V. Kravtsov, N. Y. Gnedin, T. Abel, and D. H. Rudd (2010), Computational eulerian hydrodynamics and galilean invariance, *MNRAS*, *401*(4), 2463–2476.

Roediger, E. (2009), Ram pressure stripping of disk galaxies in galaxy clusters, *Astronomische Nachrichten: Astronomical Notes*, *330*(9-10), 888–897.

Roediger, E., and M. Brüggen (2006), Ram pressure stripping of disc galaxies: the role of the inclination angle, *Monthly Notices of the Royal Astronomical Society*, *369*(2), 567–580.

Roediger, E., M. Brüggen, M. Owers, H. Ebeling, and M. Sun (2014), Star formation in shocked cluster spirals and their tails, *Monthly Notices of the Royal Astronomical Society: Letters*, *443*(1), L114–L118.

Rosen, A., and J. N. Bregman (1995), Global models of the interstellar medium in disk galaxies, *The Astrophysical Journal*, *440*, 634.

Rudd, D. H., A. R. Zentner, and A. V. Kravtsov (2008), Effects of baryons and dissipation on the matter power spectrum, *The Astrophysical Journal*, *672*(1), 19.

Ruggiero, R., and G. B. Lima Neto (2017), The fate of the gaseous discs of galaxies that fall into clusters, *Monthly Notices of the Royal Astronomical Society*, *468*(4), 4107–4115.

Rupke, D. (2018), A Review of Recent Observations of Galactic Winds Driven by Star Formation, *Galaxies*, *6*(4), 138, doi:10.3390/galaxies6040138.

Rupke, D. S., S. Veilleux, and D. B. Sanders (2005), Outflows in infrared-luminous starbursts at z¡ 0.5. ii. analysis and discussion, *The Astrophysical Journal Supplement Series*, *160*, 115.

Ruszkowski, M., T. Enßlin, M. Brüggen, S. Heinz, and C. Pfrommer (2007), Impact of tangled magnetic fields on fossil radio bubbles, *Monthly Notices of the Royal Astronomical Society*, *378*(2), 662–672.

Ruszkowski, M., T. Enßlin, M. Brüggen, M. Begelman, and E. Churazov (2008), Cosmic ray confinement in fossil cluster bubbles, *Monthly Notices of the Royal Astronomical Society*, *383*(4), 1359–1365.

Ruszkowski, M., M. Brüggen, D. Lee, and M.-S. Shin (2014), Impact of magnetic fields on ram pressure stripping in disk galaxies, *The Astrophysical Journal*, *784*, 75, doi:10.1088/0004-637X/784/1/75.

Ruszkowski, M., H.-Y. K. Yang, and E. Zweibel (2017), Global simulations of galactic winds including cosmic-ray streaming, *The Astrophysical Journal*, *834*(2), 208.

Sakai, S., and B. F. Madore (1999), Detection of the red giant branch stars in m82 using the hubble space telescope, *ApJ*, *526*(2), 599.

Salem, M., and G. L. Bryan (2014), Cosmic ray driven outflows in global galaxy disc models, *Monthly Notices of the Royal Astronomical Society*, *437*(4), 3312–3330.

Saury, E., M.-A. Miville-Deschênes, P. Hennebelle, E. Audit, and W. Schmidt (2014), The structure of the thermally bistable and turbulent atomic gas in the local interstellar medium, *Astronomy & Astrophysics*, *567*, A16.

Scannapieco, E. (2017), The Production of Cold Gas Within Galaxy Outflows, *ApJ*, *837*(1), 28, doi:10.3847/1538-4357/aa5d0d.

Scannapieco, E., and M. Brüggen (2015), The launching of cold clouds by galaxy outflows. i. hydrodynamic interactions with radiative cooling, *The Astrophysical Journal*, *805*, 158.

Schlickeiser, R. (1989), Cosmic-ray transport and acceleration. i-derivation of the kinetic equation and application to cosmic rays in static cold media. ii-cosmic rays in moving cold media with application to diffusive shock wave acceleration, *The Astrophysical Journal*, *336*, 243–293.

Schmidt, M. (1959), The rate of star formation., *The astrophysical journal*, *129*, 243.

Schmidt, P., et al. (2019), Chang-es-xvi. an in-depth view of the cosmic-ray transport in the edge-on spiral galaxies ngc 891 and ngc 4565, *Astronomy & Astrophysics*, *632*, A12.

Schneider, E. E., B. E. Robertson, and T. A. Thompson (2018), Production of Cool Gas in Thermally Driven Outflows, *ApJ*, *862*(1), 56, doi:10.3847/1538-4357/aacce1.

Schneider, E. E., E. C. Ostriker, B. E. Robertson, and T. A. Thompson (2020), The physical nature of starburst-driven galactic outflows, *ApJ*, *895*, 43, doi:10.3847/1538-4357/ab8ae8.

Schulz, S., and C. Struck (2001), Multi stage three-dimensional sweeping and annealing of disc galaxies in clusters, *Monthly Notices of the Royal Astronomical Society*, *328*(1), 185–202.

Scodeggio, M., and G. Gavazzi (1993), 21 centimeter study of spiral galaxies in clusters. iii-neutral gas content, star formation, and radio continuum properties, *The Astrophysical Journal*, *409*, 110–125.

Scoville, N., A. Sargent, D. Sanders, and B. Soifer (1991), Dust and gas in the core of arp 220 (ic 4553), *The Astrophysical Journal*, *366*, L5–L9.

Semenov, V. A., A. V. Kravtsov, and N. Y. Gnedin (2016), Nonuniversal star formation efficiency in turbulent ism, *The Astrophysical Journal*, *826*(2), 200.

Semenov, V. A., A. V. Kravtsov, and N. Y. Gnedin (2017), The physical origin of long gas depletion times in galaxies, *The Astrophysical Journal*, *845*(2), 133.

Semenov, V. A., A. V. Kravtsov, and N. Y. Gnedin (2018), How galaxies form stars: the connection between local and global star formation in galaxy simulations, *The Astrophysical Journal*, *861*(1), 4.

Semenov, V. A., A. V. Kravtsov, and D. Caprioli (2021), Cosmic-ray diffusion suppression in star-forming regions inhibits clump formation in gas-rich galaxies, *The Astrophysical Journal*, *910*(2), 126.

Shapley, A. E., C. C. Steidel, M. Pettini, and K. L. Adelberger (2003), Rest-frame ultraviolet spectra of z 3 lyman break galaxies, *The Astrophysical Journal*, *588*, 65.

Sharma, P., P. Colella, and D. F. Martin (2010), Numerical implementation of streaming down the gradient: application to fluid modeling of cosmic rays and saturated conduction, *SIAM Journal on Scientific Computing*, *32*(6), 3564–3583.

Sharma, P., M. McCourt, E. Quataert, and I. J. Parrish (2012), Thermal instability and the feedback regulation of hot haloes in clusters, groups and galaxies, *MNRAS*, *420*, 3174–3194.

Silvia, D. W., B. D. Smith, and J. M. Shull (2010), Numerical simulations of supernova dust destruction. i. cloud-crushing and post-processed grain sputtering, *ApJ*, *715*, 1575.

Silvia, D. W., B. D. Smith, and J. M. Shull (2012), Numerical simulations of supernova dust destruction. ii. metal-enriched ejecta knots, *ApJ*, *748*, 12.

Simpson, C. M., R. Pakmor, F. Marinacci, C. Pfrommer, V. Springel, S. C. Glover, P. C. Clark, and R. J. Smith (2016), The role of cosmic-ray pressure in accelerating galactic outflows, *The Astrophysical Journal Letters*, *827*(2), L29.

Slavin, J. D., E. Dwek, M.-M. Mac Low, and A. S. Hill (2020), The dynamics, destruction, and survival of supernova-formed dust grains, *ApJ*, *902*(2), 135.

Soifer, B., G. Helou, C. Lonsdale, G. Neugebauer, P. Hacking, J. Houck, F. Low, W. Rice, and M. Rowan-Robinson (1984), The remarkable infrared galaxy arp 220= ic 4553, *The Astrophysical Journal*, *283*, L1–L4.

Somerville, R. S., and R. Davé (2015), Physical models of galaxy formation in a cosmological framework, *Annual Review of Astronomy and Astrophysics*, *53*, 51–113.

Sparre, M., C. Pfrommer, and M. Vogelsberger (2019), The physics of multiphase gas flows: fragmentation of a radiatively cooling gas cloud in a hot wind, *Monthly Notices of the Royal Astronomical Society*, *482*, doi:10.1093/mnras/sty3063.

Sparre, M., C. Pfrommer, and K. Ehlert (2020), Interaction of a cold cloud with a hot wind: the regimes of cloud growth and destruction and the impact of magnetic fields, *Monthly Notices of the Royal Astronomical Society*, *499*, 4261–4281, doi:10.1093/mnras/staa3177.

Spergel, D. N., et al. (2003), First-year wilkinson microwave anisotropy probe (wmap)* observations: determination of cosmological parameters, *The Astrophysical Journal Supplement Series*, *148*(1), 175.

Spilker, J. S., et al. (2020), Ubiquitous molecular outflows in z¿ 4 massive, dusty galaxies. ii. momentum-driven winds powered by star formation in the early universe, *The Astrophysical Journal*, *905*(2), 86.

Spitzer, L. J. (1956), On a possible interstellar galactic corona, *ApJ*, *124*, 20, doi: 10.1086/146200.

Squire, J., P. F. Hopkins, E. Quataert, and P. Kempski (2021), The impact of astrophysical dust grains on the confinement of cosmic rays, *Monthly Notices of the Royal Astronomical Society*, *502*(2), 2630–2644.

Steidel, C. C., D. K. Erb, A. E. Shapley, M. Pettini, N. Reddy, M. Bogosavljević, G. C. Rudie, and O. Rakic (2010), The structure and kinematics of the circumgalactic medium from far-ultraviolet spectra of z= 2-3 galaxies, *The Astrophysical Journal*, *717*, 289.

Steinhauser, D., S. Schindler, and V. Springel (2016), Simulations of ram-pressure stripping in galaxy-cluster interactions, *Astronomy & Astrophysics*, *591*, A51.

Stone, J. M., and M. L. Norman (1992), The three-dimensional interaction of a supernova remnant with an interstellar cloud, *The Astrophysical Journal*, *173*, 17–19.

Strickland, D. K., and T. M. Heckman (2007), Iron line and diffuse hard x-ray emission from the starburst galaxy m82, *The Astrophysical Journal*, *658*, 258.

Strickland, D. K., and T. M. Heckman (2009), Supernova feedback efficiency and mass loading in the starburst and galactic superwind exemplar m82, *ApJ*, *697*(2), 2030.

Strong, A. W., and I. V. Moskalenko (1998), Propagation of cosmic-ray nucleons in the galaxy, *The Astrophysical Journal*, *509*(1), 212.

Strong, A. W., I. V. Moskalenko, and V. S. Ptuskin (2007), Cosmic-ray propagation and interactions in the galaxy, *Annu. Rev. Nucl. Part. Sci.*, *57*, 285–327.

Su, M., T. R. Slatyer, and D. P. Finkbeiner (2010), Giant gamma-ray bubbles from fermi-lat: active galactic nucleus activity or bipolar galactic wind?, *ApJ*, *724*(2), 1044.

Su, Y., et al. (2021), Molecular gas distribution perpendicular to the galactic plane, *The Astrophysical Journal*, *910*(2), 131.

Sun, M., C. Jones, W. Forman, P. Nulsen, M. Donahue, and G. Voit (2006), A 70 kiloparsec x-ray tail in the cluster a3627, *The Astrophysical Journal Letters*, *637*(2), L81.

Sun, M., M. Donahue, E. Roediger, P. Nulsen, G. Voit, C. Sarazin, W. Forman, and C. Jones (2009), Spectacular x-ray tails, intracluster star formation, and ulxs in a3627, *The Astrophysical Journal*, *708*(2), 946.

Sur, S., E. Scannapieco, and E. C. Ostriker (2016), Galaxy outflows without supernovae, *The Astrophysical Journal*, *818*(1), 28.

Sutherland, R. S., and M. A. Dopita (1993), Cooling functions for low-density astrophysical plasmas, *The Astrophysical Journal Supplement Series*, *88*, 253–327.

Tajima, T., and J. M. Dawson (1979), Laser electron accelerator, *Physical Review Letters*, *43*(4), 267.

Tan, B., and S. P. Oh (2021), A model for line absorption and emission from turbulent mixing layers, *preprint*, arXiv:2105.11496.

Tan, B., S. P. Oh, and M. Gronke (2021), Radiative mixing layers: insights from turbulent combustion, *MNRAS*, *502*(3), 3179–3199.

Tasker, E. J., and G. L. Bryan (2006), Simulating star formation and feedback in galactic disk models, *The Astrophysical Journal*, *641*(2), 878.

Thomas, T., and C. Pfrommer (2019), Cosmic-ray hydrodynamics: Alfvén-wave regulated transport of cosmic rays, *Monthly Notices of the Royal Astronomical Society*, *485*(3), 2977–3008.

Thompson, T. A., E. Quataert, D. Zhang, and D. H. Weinberg (2016), An origin for multiphase gas in galactic winds and haloes, *Monthly Notices of the Royal Astronomical Society*, *455*, 1830–1844.

Thoudam, S., J. Rachen, A. van Vliet, A. Achterberg, S. Buitink, H. Falcke, and J. Hörandel (2016), Cosmic-ray energy spectrum and composition up to the ankle: the case for a second galactic component, *Astronomy & Astrophysics*, *595*, A33.

Tonnesen, S. (2019), The journey counts: The importance of including orbits when simulating ram pressure stripping, *ApJ*, *874*, 161, doi:10.3847/1538-4357/ab0960.

Tonnesen, S., and G. L. Bryan (2009), Gas stripping in simulated galaxies with a multiphase interstellar medium, *The Astrophysical Journal*, *694*(2), 789.

Tonnesen, S., and G. L. Bryan (2010), The tail of the stripped gas that cooled: Hi, hα, and x-ray observational signatures of ram pressure stripping, *The Astrophysical Journal*, *709*(2), 1203.

Tonnesen, S., and G. L. Bryan (2012), Star formation in ram pressure stripped galactic tails, *Monthly Notices of the Royal Astronomical Society*, *422*(2), 1609–1624.

Tonnesen, S., and G. L. Bryan (2021), Its clouds illusions i recall: Mixing drives the acceleration of clouds from ram pressure stripped galaxies, *ApJ*, *911*, 68.

Tonnesen, S., and J. Stone (2014), The ties that bind? galactic magnetic fields and ram pressure stripping, *The Astrophysical Journal*, *795*, 148, doi:10.1088/0004-637X/795/2/148.

Townsend, R. (2009), An exact integration scheme for radiative cooling in hydrodynamical simulations, *The Astrophysical Journal Supplement Series*, *181*(2), 391.

Trachternach, C., W. De Blok, F. Walter, E. Brinks, and R. Kennicutt Jr (2008), Dynamical centers and noncircular motions in things galaxies: implications for dark matter halos, *The Astronomical Journal*, *136*(6), 2720.

Trapp, C., et al. (2021), Gas infall and radial transport in cosmological simulations of milky way-mass disks, *arXiv preprint arXiv:2105.11472*.

Tremonti, C. A., T. M. Heckman, G. Kauffmann, J. Brinchmann, S. Charlot, S. D. White, M. Seibert, et al. (2004), The origin of the mass-metallicity relation: insights from 53,000 star-forming galaxies in the sloan digital sky survey, *ApJ*, *613*, 898.

Trotta, R., G. Jóhannesson, I. V. Moskalenko, and et al. (2011), Constraints on cosmic-ray propagation models from a global bayesian analysis, *ApJ*, *729*, 106.

Tsai, J. C., and W. G. Mathews (1995), Interstellar grains in elliptical galaxies: grain evolution, *preprint*.

Tumlinson, J., et al. (2011), The large, oxygen-rich halos of star-forming galaxies are a major reservoir of galactic metals, *Science*, *334*(6058), 948–952.

Übler, H., T. Naab, L. Oser, and et al. (2014), Why stellar feedback promotes disc formation in simulated galaxies, *MNRAS*, *443*, 2092.

Uhlig, M., C. Pfrommer, M. Sharma, B. B. Nath, T. Enßlin, and V. Springel (2012), Galactic winds driven by cosmic ray streaming, *Monthly Notices of the Royal Astronomical Society*, *423*(3), 2374–2396.

Veilleux, S., G. Cecil, and J. Bland-Hawthorn (2005), Galactic winds, *Annu. Rev. Astron. Astrophys.*, *43*, 769–826.

Veilleux, S., R. Maiolino, A. D. Bolatto, and S. Aalto (2020), Cool outflows in galaxies and their implications, *The Astronomy and Astrophysics Review*, *28*, 1–173.

Vijayan, A., K. C. Sarkar, B. B. Nath, P. Sharma, and Y. Shchekinov (2018), Extraplanar x-ray emission from disc-wide outflows in spiral galaxies, *Monthly Notices of the Royal Astronomical Society*, *475*(4), 5513–5528.

Vogelsberger, M., S. Genel, D. Sijacki, P. Torrey, V. Springel, and L. Hernquist (2013), A model for cosmological simulations of galaxy formation physics, *Monthly Notices of the Royal Astronomical Society*, *436*(4), 3031–3067.

Voit, G. M., G. L. Bryan, B. W. O'Shea, and M. Donahue (2015), Precipitation-regulated star formation in galaxies, *Astrophysical Journal Letters*, *808*, L30, doi: 10.1088/2041-8205/808/1/L30.

Vollmer, B., M. Soida, A. Chung, L. Chemin, J. Braine, A. Boselli, and R. Beck (2009), Ram pressure stripping of the multiphase ism in the virgo cluster spiral galaxy ngc 4438, *Astronomy and Astrophysics*, *496*, 669–675.

Vollmer, B., M. Soida, A. Chung, R. Beck, M. Urbanik, K. T. Chyży, K. Otmianowska-Mazur, and J. H. V. Gorkom (2010), The influence of the cluster environment on the large-scale radio continuum emission of 8 virgo cluster spirals, *Astronomy and Astrophysics*, *512*, A36.

Vollmer, B., M. Soida, R. Beck, A. Chung, M. Urbanik, K. T. Chyży, K. Otmianowska-Mazur, and J. D. P. Kenney (2013), Large-scale radio continuum properties of 19 virgo cluster galaxies-the influence of tidal interactions, ram pressure stripping, and accreting gas envelopes, *Astronomy and Astrophysics*, *553*, A116.

Vulcani, B., B. M. Poggianti, M. Gullieuszik, A. Moretti, S. Tonnesen, Y. L. Jaffé, J. Fritz, G. Fasano, and D. Bettoni (2018), Enhanced star formation in both disks and ram-pressure-stripped tails of gasp jellyfish galaxies, *The Astrophysical Journal Letters*, *866*(2), L25.

Walch, S., and T. Naab (2015), The energy and momentum input of supernova explosions in structured and ionized molecular clouds, *Monthly Notices of the Royal Astronomical Society*, *451*(3), 2757–2771.

Walter, F., et al. (2017), Dense molecular gas tracers in the outflow of the starburst galaxy ngc 253, *The Astrophysical Journal*, *835*, 265.

Wang, B. (1994), Cooling gas outflows from galaxies, *arXiv preprint astro-ph/9412033*.

Watson, M. G., V. Stanger, and R. E. Griffiths (1984), X-ray emission from m82, *The Astrophysical Journal*, *286*, 144–158.

Weiß, A., F. Walter, N. Neininger, and U. Klein (1999), Evidence for an expanding molecular superbubble in m 82, *Astronomy and Astrophysics*, *345*, 23–26.

Werk, J. K., J. X. Prochaska, C. Thom, J. Tumlinson, T. M. Tripp, J. M. O'Meara, and M. S. Peeples (2013), The cos-halos survey: an empirical description of metal-line absorption in the low-redshift circumgalactic medium, *ApJS*, *204*, 17.

Wiener, J., E. G. Zweibel, and S. P. Oh (2013), Cosmic ray heating of the warm ionized medium, *The Astrophysical Journal*, *767*(1), 87.

Wiener, J., C. Pfrommer, and S. P. Oh (2017), Cosmic ray driven galactic winds: streaming or diffusion?, *MNRAS*, *467*, 906–921, doi:10.1093/mnras/stx127.

Wiener, J., E. G. Zweibel, and S. P. Oh (2018), High β effects on cosmic ray streaming in galaxy clusters, *Monthly Notices of the Royal Astronomical Society*, *473*(3), 3095–3103.

Wiener, J., E. G. Zweibel, and M. Ruszkowski (2019), Cosmic ray acceleration of cool clouds in the circumgalactic medium, *MNRAS*, *489*, 205–223, doi: 10.1093/mnras/stz2007.

Wulf, T. (1910), About the radiation of high penetration capacity contained in the atmosphere, *Physikalische Zeitschrift*, *5*, 152–157.

Wünsch, R., S. Walch, A. Whitworth, and F. Dinnbier (2017), Tree-based solvers for adaptive mesh refinement code flash–ii: radiation transport module treeray, *arXiv preprint arXiv:1708.06142*.

Xu, J., and J. M. Stone (1995), The hydrodynamics of shock-cloud interactions in three dimensions, *The Astrophysical Journal*, *454*, 172.

Yan, H., and A. Lazarian (2004), Cosmic-ray scattering and streaming in compressible magnetohydrodynamic turbulence, *The Astrophysical Journal*, *614*(2), 757.

Yang, H.-Y., and M. Ruszkowski (2017), The spatially uniform spectrum of the fermi bubbles: The leptonic active galactic nucleus jet scenario, *The Astrophysical Journal*, *850*(1), 2.

Yang, H.-Y., M. Ruszkowski, P. Ricker, E. Zweibel, and D. Lee (2012), The fermi bubbles: supersonic active galactic nucleus jets with anisotropic cosmic-ray diffusion, *The Astrophysical Journal*, *761*(2), 185.

Yang, H.-Y. K., M. Ruszkowski, and E. Zweibel (2013), The fermi bubbles: gamma-ray, microwave and polarization signatures of leptonic agn jets, *Monthly Notices of the Royal Astronomical Society*, *436*(3), 2734–2746.

Yoast-Hull, T. M., J. E. Everett, J. S. I. Gallagher, and E. G. Zweibel (2013), Winds, clumps, and interacting cosmic rays in m82, *ApJ*, *768*, 53.

Yoast-Hull, T. M., J. S. I. Gallagher, E. G. Zweibel, and J. E. Everett (2014), Active galactic nuclei, neutrinos, and interacting cosmic rays in ngc 253 and ngc 1068, *ApJ*, *780*, 137.

Yun, M. S., P. T. Ho, and K. Y. Lo (1994), A high-resolution image of atomic hydrogen in the m81 group of galaxies, *Nature*, *372*, 530–532.

Yun, M. S., N. A. Reddy, and J. J. Condon (2001), Radio properties of infrared-selected galaxies in the iras 2 jy sample, *The Astrophysical Journal*, *554*, 803.

Zahid, H. J., R. M. Yates, L. J. Kewley, and R. P. Kudritzki (2013), The observed relation between stellar mass, dust extinction, and star formation rate in local galaxies, *Astrophysical Journal*, *763*, doi:10.1088/0004-637X/763/2/92.

Zhang, B., et al. (2013), The narrow x-ray tail and double hα tails of eso 137-002 in a3627, *The Astrophysical Journal*, *777*(2), 122.

Zhang, D., T. A. Thompson, E. Quataert, and N. Murray (2017), Entrainment in trouble: cool cloud acceleration and destruction in hot supernova-driven galactic winds, *MNRAS*, *468*(4), 4801–4814.

Zirakashvili, V. N., D. Breitschwerdt, V. S. Ptuskin, and H. J. Voelk (1996), Magnetohydrodynamic wind driven by cosmic rays in a rotating galaxy, *A&A*, *311*, 113.

Zweibel, E. G. (2013), The microphysics and macrophysics of cosmic rays, *Physics of Plasmas*, *20*, 055,501.

Zweibel, E. G. (2017), The basis for cosmic ray feedback: Written on the wind, *Physics of Plasmas*, *24*(5), 055,402.

Zweibel, E. G. (2020), The role of pressure anisotropy in cosmic-ray hydrodynamics, *The Astrophysical Journal*, *890*(1), 67.

Zweibel, E. G., and C. Heiles (1997), Magnetic fields in galaxies and beyond, *Nature*, *385*, 131.